UNIVERSITY OF SOUTHAMPTON

Faculty of Physical and Applied Sciences

Optoelectronics Research Centre (ORC)

Pump Conditioning and Optimisation for Erbium Doped Fibre Applications

by

Ee Leong Lim

Thesis for the degree of Doctor of Philosophy

Sep 2012

UNIVERSITY OF SOUTHAMPTON

ABSTRACT

FACULTY OF ENGINEERING AND APPLIED SCIENCE

OPTOELECTRONICS RESEARCH CENTRE

Doctor of Philosophy

PUMP CONDITIONING AND OPTIMISATION FOR ERBIUM DOPED FIBRE APPLICATIONS

by Ee Leong Lim

This thesis presents my investigation into in-band pumped erbium doped fibre amplifiers (EDFAs) and their performance under high power continuous wave (cw) operation and high energy low repetition rate pulsed operation. In addition, Q-switched erbium doped fibre lasers were investigated and used as the seed laser for a high energy low repetition rate EDFA system. Furthermore, the power scaling of all-fibre frequency doubled fibre lasers based on periodically poled silica fibre (PPSF) was also investigated.

In Q-switched fibre lasers, the multiple-peak phenomenon (MPP) is an undesirable effect in which the Q-switched pulse develops sub-structure or even breaks into multiple sub pulses. I demonstrated that the MPP can be eliminated by increasing the acousto-optic modulator rise time. An experimentally validated numerical model was also used to explain the origin of MPP. Next, I showed that the interplay between MPP and modulation instability (MI) changes the detail of the spectral evolution of the Q-switched pulses.

The in-band EDFAs were investigated using 1535 nm pump fibre lasers. For cw operation, a highly efficient (~ 80%), high power (18.45 W) in-band, core pumped erbium/ytterbium co-doped fibre laser was demonstrated. Using a fitted simulation model, I showed that the significantly sub-quantum limit conversion efficiency of in-band pumped EDFAs observed experimentally can be explained by concentration quenching. I then numerically studied and experimentally validated the optimum pumping configuration for power scaling of in-band, cladding pumped EDFAs. My simulation results indicate that a ~ 77% power conversion efficiency with high output power should be possible through cladding pumping of current commercially available pure erbium doped active fibres providing the loss experienced by the cladding guided 1535 nm pump due to the coating absorption can be reduced to an acceptable level by better coating material choice. The power conversion efficiency has the potential to exceed 90% if concentration quenching of erbium ions can be reduced via improvements in fibre design and fabrication.

For low repetition rate pulsed operation, I demonstrated and compared high-energy, in-band pumped EDFAs operating at 1562.5 nm under both a core pumping scheme (CRS) and a cladding pumping scheme (CLS). The CRS/CLS sources generated smooth, single-peak pulses with maximum pulse energies of ~1.53/1.50 mJ, and corresponding pulse widths of ~176/182 ns respectively, with an M^2 of ~1.6 in both cases. However, the conversion efficiency for the CLS was >1.5 times higher than the equivalent CRS variant operating at the same pulse energy due to the lower pump intensity in the CLS that mitigates the detrimental effects of concentration quenching. With a longer fibre length in a CLS implementation a pulse energy of ~2.6 mJ was demonstrated with a corresponding M^2 of ~4.2. Using numerical simulations I explained that the saturation of pulse energy observed in my experiments was due to saturation of the pump absorption.

For the frequency doubling work, the fundamental pump source of the PPSF was a master oscillator power amplifier seeded with a tuneable external cavity laser. During the high power operation, the heat deposition along the PPSF shifted the optimal quasi-phase matched wavelength to a longer wavelength. This shift must be compensated to achieve optimal performance of the PPSF under test and was achieved in my experiment by tuning the central wavelength of the pump source. At the end of the high power experiment, the PPSF samples degraded to ~40% of their pristine PPSF normalised efficiencies. The glass property of the PPSF had also been changed by the high power exposure. A high power all-fibre frequency doubled laser was demonstrated with 1.13 W of second harmonic average power with ~27% internal conversion efficiency.

Table of contents

Chapter 1 Introduction 1

- 1.1 The motivation 1
- 1.2 Structure of the thesis 5

Chapter 2 Background 7

- 2.1 Optical properties of optical fibres 7
  - 2.1.1 Wave equations for optical fibres 7
  - 2.1.2 Weakly guided step index fibres 8
  - 2.1.3 Fibre modes in multimode fibres 10
  - 2.1.4 Guided modes in actual fibres 12
- 2.2 Optical nonlinearity 14
  - 2.2.1 Nonlinear induced polarisation 14
  - 2.2.2 Third order nonlinear processes 15
  - 2.2.3 Nonlinearities in optical fibre 18
- 2.3 Erbium doped fibre amplifiers 26
  - 2.3.1 Emission and absorption of light 26
  - 2.3.2 Pump wavelengths for erbium ions 28
  - 2.3.3 Pump coupling scheme for active fibres 29
  - 2.3.4 Overlap factor 32
  - 2.3.5 Quasi-three level fibre amplifier model 33
  - 2.3.6 Amplified spontaneous emission 33
  - 2.3.7 Master oscillator power amplifier 35

Chapter 3 Q-switched fibre lasers 39

- 3.1 Point model of Q-switched laser 39
- 3.2 The multiple-peak phenomena in core-pumped Q-switched fibre laser 41
  - 3.2.1 Experiment 41
  - 3.2.2 Simulation 44
- 3.3 The MPP and nonlinear effects in Q-switched cladding-pumped fibre lasers 51
  - 3.3.1 MPP in Q-switched cladding-pumped fibre lasers 51

3.3.2 Nonlinear effects in Q-switched cladding-pumped fibre lasers 52
3.3.3 The interplay of MPP and nonlinearity 53
3.4 Conclusion 55
Chapter 4 Continuous wave in-band pumped fibre amplifiers 57
4.1 Background 57
4.1.1 Net cross section and transparency inversion 57
4.1.2 More on erbium ion transitions 59
4.1.3 Simulation model for the upconversion of erbium ions 64
4.1.4 Discussion on ion concentration quenching 65
4.1.5 Ytterbium codoping in in-band pumped EDFA 67
4.2 State of the arts 69
4.3 Characteristics of the pump source 70
4.4 Core-pumped MOPA 72
4.4.1 Experiment setup 72
4.4.2 Fitting results 74
4.5 Power scaling of in-band pumped EDF 75
4.5.1 Simulation 75
4.5.2 Experimental validation: cladding pump case 78
4.6 Conclusion 79
Chapter 5 High energy in-band pumped fibre amplifiers 80
5.1 Background 81
5.1.1 Pulse amplification and energy extraction 81
5.1.2 Simulation model for pulse fibre amplifier 83
5.2 State of the arts 85
5.3 Experimental setup 86
5.4 Experiment 88
5.4.1 Seed laser characteristics 88
5.4.2 Pre-amplifier characteristics 89
5.4.3 In-band pumped final amplifier characteristics 89
5.4.4 CLS experiment with a longer length of fibre 94
5.5 Simulation 95

5.5.1 The simulation model 95

5.5.2 Explanation for pulse energy saturation due to pump saturation 97

5.6 Conclusion 100

Chapter 6 All-fibre frequency-doubled fibre lasers .... **Error! Bookmark not defined.**

6.1 Background .... **Error! Bookmark not defined.**

6.1.1 DC-induced second order nonlinearity in optical fibre .... **Error! Bookmark not defined.**

6.1.2 Thermal poling .... **Error! Bookmark not defined.**

6.1.3 Second harmonic generation in periodically poled silica fibre**Error! Bookmark not defined.**

6.1.4 Realising the quasi-phase matched condition in poled fibres**Error! Bookmark not defined.**

6.1.5 Typical parameters of PPSF .... **Error! Bookmark not defined.**

6.1.6 Glass defects and PPSF .... **Error! Bookmark not defined.**

6.2 State of the arts .... **Error! Bookmark not defined.**

6.3 First demonstration of watts-level all-fibre frequency-doubled lasers**Error! Bookmark not defined.**

6.3.1 PPSF specification .... **Error! Bookmark not defined.**

6.3.2 Setup of first harmonic source .... **Error! Bookmark not defined.**

6.3.3 Characteristics of the first harmonic source .... **Error! Bookmark not defined.**

6.3.4 Characteristics of the all-fibre frequency-double laser .... **Error! Bookmark not defined.**

6.4 Degradation of the PPSF efficiency .... **Error! Bookmark not defined.**

6.4.1 The first harmonic source .... **Error! Bookmark not defined.**

6.4.2 High power operation .... **Error! Bookmark not defined.**

6.4.3 Change in transmission spectrum .... **Error! Bookmark not defined.**

6.4.4 Possible degradation mechanisms .... **Error! Bookmark not defined.**

6.5 Conclusion .... **Error! Bookmark not defined.**

Chapter 7 Conclusion and future work 101

7.1 Conclusion 101

7.2 Future work 103

Chapter 8 Appendix 105

8.1 Derivation of the rate equations for the upconversion of erbium ions 105

8.2 List of Publications 108

Chapter 9 References 109

List of figures

Figure 1-1 An illustration of DCF with octagonal shaped inner cladding. 1

Figure 1-2 The energy level diagram of (a) the 980 nm pumped EDF (b) the 915/975 nm pumped EYDF to generate 1.55 μm. 2

Figure 1-3 The energy level diagram of in-band pumped EDF to generate 1.55 μm. 2

Figure 2-1 The normalised intensity distribution of the first 6 LP-modes of a step index fibre with V=8.1. The white circular lines outline the fibre core with diameter of 40 μm. 11

Figure 2-2 Comparison of the LP_{01} modes of step index fibres with same core diameter but different V-numbers. The intensity is normalised to the intensity peak of the respective mode 12

Figure 2-3 (a) The refractive index difference of Liekki Er-60-40/140 along the radial position provided by the fibre manufacturer (Liekki) and reconfirmed in-house by Mr Robert Standish (b) The radial intensity distribution (normalised to the same power) of the first 5 LP-modes calculated using transfer matrix method. 13

Figure 2-4 Electromagnetic wave incident on nonlinear medium induces a nonlinear polarisation. The interaction of the electromagnetic wave and the induced nonlinear polarisation can be described by Eq. (2-17). An example of $\chi^{(2)}$-medium is the periodically poled silica fibre (PPSF) and an example of $\chi^{(3)}$-medium is the optical fibre. 14

Figure 2-5 The nonlinear polarisation in $\chi^{(3)}$-medium gives rise to SPM, XPM and FWM. 15

Figure 2-6 (a) An example of θ_+-type FWM where frequency ω_4 is generated with the sum of ω_1, ω_2 and ω_3. (b) An example of θ_--type FWM where frequency ω_3 and ω_4 are generated with the sum of ω_1 and ω_2. 17

Figure 2-7 An illustration of the energy conservation (a) and phase mismatch (b) diagrams of a θ_--type FWM. 17

Figure 2-8 Temporal variation of the electric field of an optical pulse that spreads in a linear medium with anomalous dispersion; the shorter-wavelength component B has a larger group velocity and therefore travels faster than the longer-wavelength component R [13] 19

Figure 2-9 Temporal variation of the electric field of an optical pulse in a nonlinear nondispersive medium. The self-phase modulation ($n_2>0$) introduces a negative frequency shift at the leading half of the pulse (denotes R) and a positive frequency shift at the trailing half (denoted B). Even though the frequency across the pulse varies, its shape is not altered [13] 21

Figure 2-10 Modulation instability is a θ_--type FWM where the 2 pump photon are degenerate, create two sidebands at Ω_s away from the pump wavelength. 22

Figure 2-11 Gain spectra of MI at three power levels for SMF 28e (i.e., β_2=-23 ps^2km^{-1}, D=18 $pskm^{-1}nm^{-1}$, γ=1.2 $W^{-1}km^{-1}$). 23

Figure 2-12 An illustration of stimulated Brillouin scattering 24

Figure 2-13 The population density N_2 and N_1 are determined by the rate of absorption, stimulated emission , spontaneous emission of photon as well as pumping and depumping rate of ion. 27

Figure 2-14 The absorption- and emission- cross sections of a typical Er^{3+}*-doped Al-Ge-Silicate fibre. The cross section data is from [22].* *29*

Figure 2-15 The absorption- (solid) and emission- (dotted) cross sections of a typical Er^{3+}/Yb^{3+} *co-doped phosphosilicate fibre. The cross section data is from [23].* *29*

Figure 2-16 GTWave multimode fibre coupler schematic. s & p denote signal and pump rods, respectively [25]. *30*

Figure 2-17 The brightness conversion in cladding pumped fibre [6]. *31*

Figure 2-18 With the overlap factor, the circularly symmetric ion distribution profile is simplified into an equivalent flat-top ion distribution profile. The blue lines are the LP_{01} *mode intensity profile and red lines are the ion distribution profile.* *32*

Figure 2-19 The simulated behaviour of 980 nm pumped EDFA along the fibre position with and without ASE consideration. (a) The pump power (b) The backward and forward ASE power (c) The populatin inversion (d) The signal power. *35*

Figure 2-20 Schematic of a master oscillator power amplifier designed for a targeted application requirement. Seed: seed laser, pre-amp: preamplifier and final-amp: final stage amplifiers. The rectangular symbol with an arrow represents an optical isolator that prevents the backward amplified spontaneous emission (ASE) from the next stage to influence the current stage. The optical processing unit (OPU) is a component used to tailor the characteristic of the signal light, for example, the spectral property can be tailored using fibrised filter and temporal characteristic can be tailored with electro-optic modulator *35*

Figure 2-21 The aftermath of the fire that happened at a bent section of a cladding guided pump fibre. Due to the bending, the multimode pump power leaked out from the fibre and became a heat source, which eventually lead to the fire that initiate from the high temperature resistant kapton tape *37*

Figure 3-1 Typical Q-switched pulse shapes obtained from numerical integration of the rate equation of the point model at various initial population inversion (N_i)*. The photon-number density n(t) is normalised to the threshold population difference* N_t *and the time is normalised to the photon cavity lifetime* τ_p *[13].* *40*

Figure 3-2 Experimental setup for the Q-switched all-fibre ring laser with an estimated cavity length of~6.4 m. The port 1, port 2 and port 3 of the circulator are labelled *41*

Figure 3-3 The measured AOM switching response (solid line) with AWG rise time (τ_{AWG}) *of 24 ns and the corresponding fitting function (dashed line) using Eq. (3-3) with rise time* (τ_r) *of 70 ns.* *42*

Figure 3-4 The temporal characteristic of pulsed produce with 3 different AOM rise times measured with Thorlabs D400FC InGaAs detector at 5 kHz repetition rate with AOM opening time of 1 μs*. The average powers measured are 13.50 mW, 16.75 mW and 16.75 mW for rise time of 35 ns, 70 ns and 150 ns respectively. The pulse widths are ~100 ns for all cases.* *43*

Figure 3-5 A typical spectrum of the Q-switched all-fibre ring laser measured with HP 86140A optical spectrum analyser with 0.07 nm resolution. The FWHM of the spectrum is determined as 0.22 nm. *44*

Figure 3-6 Model of the Q-switched fibre ring laser shown in Figure 3-2. CLW: the clock-wise direction. *45*

Figure 3-7 Representation of upwind differencing schemes. The upper scheme is stable when the advection constant v is negative, as shown; the lower scheme is stable when the advection constant v is positive, also as shown. The Courant condition must also be satisfied [37]... 47

Figure 3-8 Comparison of (a) simulated (b) measured and postulated pulses with different AOM rise time, τ_r. 49

Figure 3-9 Output pulses for various AOM rise times in dBm scale. The time axis is normalised to the cavity round trip time of the laser cavity. (b) Solid lines: the close-out of output pulses. Dashed line: the normalised transmission function of AOM, i.e., 0 dB corresponds to the maximum transmission of the AOM.. 49

Figure 3-10 The schematic of the experimental setup for the Q-switched fibre ring laser. The estimated cavity length is ~37.5 m. The "V-t" plot illustrates the trapezoidal electrical gating pulse sent to the AOM.. 51

Figure 3-11 The Q-switched fibre ring laser is packaged in a metal box.. 51

Figure 3-12 The pulses produced with 4 different values of τ_r at fixed pump power. The pulse spectrum (resolution=2 nm) is shown inset.. 52

Figure 3-13 The normalised output spectra (resolution= 2 nm) at 3 average output powers. The spectra correspond to the average power (estimated peak power/ pulse width) of 72 mW (71 W/182 ns), 92 mW (115 W/ 134 ns), 121 mW (208 W/ 92 ns. Inset shows the pulse corresponding to 121-mW average power. 53

Figure 3-14 (a) Setup for spectrally resolved optical time gating method. The optical fibre/ electronic connections are shown in solid/dashed lines. The normalised pulse-spectrum evolution with a τ_r of (b) 500 ns and (c) 70 ns respectively (temporal resolution=10 ns, wavelength resolution=2 nm). The contour lines are separated by 1.50 dB step. In (b) and (c), the upper and lower insets show the close-up of the spectral and temporal evolution of the pulse. 55

Figure 4-1 The transparency inversion across wavelength based on the cross section in Figure 2-14. The two red dashed lines show that when the erbium fibre amplifier is pumped at 1480 nm and 1535 nm, the maximum inversion that can be reached is ~0.78 and ~0.50 respectively. Similarly, the blue dashed lines show that the signal at 1565 nm and 1605 nm can extract gain from the EDFA until an inversion level of ~0.35 and ~0.20 respectively. 58

Figure 4-2 Net cross section for various inversion levels between $^4I_{15/2}$ and $^4I_{13/2}$ manifolds of the erbium ion based on the cross section in Figure 2-14.. 59

Figure 4-3 Energy level structure of erbium ion. The wavelength scale corresponds to the wavelength of the transition from a given energy level to the ground state [22]. 60

Figure 4-4 (a) An illustration of the excited state absorption of 1.5-1.6-μm radiation by erbium ions in the $^4I_{13/2}$ level. (b) An illustration of the excited state absorption of ~0.98 μm radiation by an erbium ion in the $^4I_{11/2}$ level. Some of the ions at the $^4F_{7/2}$/ $^2H_{11/2}$/ $^4S_{3/2}$ level will emit green radiation at ~0.52-0.54 μm. 61

Figure 4-5 An illustration of the energy level diagram in the upconversion process of erbium ion in $^4I_{13/2}$. 62

Figure 4-6 A two dimensional model of silica glass network with erbium doping. The two different types of upconversion, i.e., the homogenous upconversion (HUC) and the pair induced quenching (PIQ) are schematically shown [42]. 63

Figure 4-7 The green florescence emission when pure-erbium doped large mode area (Liekki Er 60-40/140DC) is strongly pumped by 1535 nm at 16-W input pump with core-pumping scheme. 66

Figure 4-8 Measured backward fluorescence power at 980 nm for seven different long fibres when pumped by 25 mW at 1480 nm [19]. Note that the graphs are on a logarithmic scale. 66

Figure 4-9 The fitted paired ion ratio against ion concentration. The MN 97 corresponds to [42]. The nanoparticle doping and standard corresponds to the fibre in [52] fabricated with nanoparticle-enabled and standard MCVD respectively. JN95 corresponds to the fibre in [19]. Lieeki corresponds to the Er-LMA used in Section 4.4. SPI corresponds to the EYDF used in Section 4.4. 67

Figure 4-10 The energy gap between $^4I_{11/2}$ *and* $^4I_{13/2}$ *of erbium manifolds (6500* cm^{-1}*) prevents the energy transfer from the* $^4I_{13/2}$ *level* Er^{3+} *ion to the* $^2F_{7/2}$ *level* Yb^{3+} *ion.* 68

Figure 4-11 Setup configuration of the in-band pump source. HR-FBG: high-reflectivity FBG, OC-FBG: output coupling FBG. 71

Figure 4-12 Spectral plots of the 1535 nm pump laser at various output powers. 71

Figure 4-13 The experimental setup for the 1535 nm pump fibre laser. The green fluorescence is due to the the upconversion of erbium ions while the violet fluorescence is due to the of 915 nm radiation induced fluorescence in camera. 72

Figure 4-14 Experimental setup of the FP-CRS configuration. Cladding mode stripper was used only for Fibre 2. 73

Figure 4-15 Experimental (circles) and simulation (lines) results for (a) Fibre 1 and (b) Fibre 2. The inset in (a) is the output spectrum of Fibre 1 at the maximum output signal power. The inset in (b) is the simulated signal power distribution along Fibre 2 for the case of 563 mW input signal power and 7.05 W input pump power. 74

Figure 4-16 Simulated signal power distribution along the gain fibre for 5 different k-values with 0.5 W 1565 nm input signal power and 20 W input pump power in FP-CRS configuration................................75

Figure 4-17 Signal distribution at two different k-values (0.2% (solid lines) and 4.1% (dashed lines) under (a) forward-pumping scheme (FP) and (b) backward-pumping scheme (BP). Blue lines are 1565 nm-CRS, green-lines are 1565 nm-CLS and red lines are 1605 nm-CLS. The input signal power is 1 W and the input pump is 100 W. 77

Figure 4-18 The simulated (solid lines) and the experimental (circles) output signal power with respect to the absorbed pump power for the cladding pumped MOPA with input signals of 0.61 W at 1565 nm and 1605 nm 79

Figure 5-1 Optical signal passing through a short segment of an amplifier. 81

Figure 5-2 The calculated saturation energy dependence on the core diameter at 1565 nm wavelength according to the EDF-cross section shown in Figure 2-14. 82

Figure 5-3 (a) The intensity profiles of the Gaussian input pulse (blue) and output pulses at 20 dB (red) and 30 dB (green) gain respectively. The horizontal temporal axis is the coordinate in the moving pulse *frame. (b) The ratio of FWHM of the output pulse to the input pulse, defined as broadening factor, at different gain levels.* *83*

Figure 5-4 Comparison between the radially dependent model (dashed curves) and the overlap model (solid curves) for the amplification of 100 ns pulses in a (a) 30 μm core fibre pumped with 20 W and with 10 W input peak power and (b) 6 μm core fibre pumped with 10 W and with 1 W input peak power [27]. *85*

Figure 5-5 The progress of pulse energy extracted from the erbium-doped or erbium-ytterbium co-doped fibres [7, 72, 73, 77, 82-87].The results are divided into 2 categories, i.e., M2<1.65, which represents the relatively good output beam quality and M2>1.65. .... *85*

Figure 5-6 Schematic view of all-fibrised master oscillator power amplifier systems with an in-band pumped erbium-doped final amplifier stage. The upper setup represents the core pumping scheme (CRS). Since both the CRS and the cladding pumping scheme (CLS) have the same seed laser and preamplifier, only the final amplifier stage of the CLS is shown in the lower setup. *87*

Figure 5-7 (a) The seed pulse shape (with the peak power determined by fitting the area under the measured pulse shape to the measured pulse energy). (b) The normalised output spectrum of the Q-switched seed laser. *88*

Figure 5-8 (a) The normalised output spectrum before WDM (green line), after WDM (blue line) and the transmission response of the WDM (red line). (b) The pre-amplifier pulse shape. *89*

Figure 5-9 The pulse energy at different input pump powers at 0.3 kHz in the CRS (blue) and CLS (red) casess. (b) The residual pump power at different pulse energies. Note that the residual pump in the CRS has been scaled up by a factor of 10 so that the residual pump for both pumping schemes can be displayed on the same graph. *90*

Figure 5-10 The pulse energy at different levels of absorbed pump at 0.3 kHz in the CRS (blue) and CLS (red) cases. (b) The conversion efficiency versus pulse energy. *91*

Figure 5-11 (a) The pulse energy versus repetition rate for the CLS at a pump power of ~16.1 W. The inset shows the inter-pulse temporal response measured at the fibre output. (b) The output energy (left axis) and residual pump power (right axis) versus repetition rate for 4 different input pump powers for the CRS (cyan: 5.92 W, red: 8.33 W, green: 11.86 W and blue: 14.92 W). *92*

Figure 5-12 Evolution of pulse energy along the fibre under different repetition rates and pump powers [80]. *93*

Figure 5-13 (a) The normalised CRS output spectra at 3 different repetition rates at maximum input pump power. (b) The CRS pulse shapes at 4 different input pump powers at a repetition rate of 0.3 kHz. *93*

Figure 5-14 (a) The pulse energy against input pump power at a repetition rate of 0.3 kHz with a 19.5 m length of fibre. (b) The residual pump power at different pulse energies. The inset shows the conversion efficiency against pulse energy. *94*

Figure 5-15 (a) The normalised inversion at an input pump power of 3W (dashed line), 4W (dotted line) and 16 W (solid line) for the CRS (blue) and CLS (red) respectively in the presence of PIQ (i.e., k=4.1%). (b) The spatial evolution of the pulse energy at input pump power of 3 W (dashed line), 4 W (dotted line) and 16 W (solid line) for the CRS (blue) and CLS (red) respectively in the presence of PIQ (i.e., k=4.1%). *97*

Figure 5-16 (a) The pulse energy at different input pump power levels in the presence (k=4.1%) and absence (k=0.0%) of paired ions. (b) The residual pump power at different output pulse energies. Note that the residual pump power for the CRS with PIQ has been scaled up by a factor of 10 so that the residual pump power can be displayed on the same plot for all cases. 99

Figure 6-1 The schematic of the effective second order nonlinearity induced by the dc-field in a silica optical fibre.. ***Error! Bookmark not defined.***

Figure 6-2 (a) Microscope picture of a typical twin hole fibre. (b) The schematic of a twin-hole fibre with two electrodes inserted through side polished holes for thermal poling [90]. ***Error! Bookmark not defined.***

Figure 6-3 Coordinate system used to represent the interaction of the FH and SH in PPSF [90]. .... ***Error! Bookmark not defined.***

Figure 6-4 Intensity of SH wave along the propagation direction for non-phase matching (green), phase matching (blue) and quasi-phase matching (red) cases. The regions enclosed by purple dotted lines illustrate the regions where effective second order nonlinearity are present while the regions in between illustrate the regions where effective second order nonlinearity are absent. The height of the purple dotted lines is for illustration purpose only and does not correspond to the vertical scale. The SH is assumed to be zero at the start of the SH medium. The simulation program was written by Dr Corbari from physical optics group. .... ***Error! Bookmark not defined.***

Figure 6-5 The schematic of a uniformly poled fibre that is fabricated into a PPSF with a period of modulation Λ through selective UV exposure. .... ***Error! Bookmark not defined.***

Figure 6-6 (a) Variation of the effective refractive index with wavelength in FORC-2 fibre (b) Dependence of the QPM period on the fundamental wavelength for the FORC-2 fibre from mode-propagation simulator (solid line) and experimental measurements (filled triangles) [90]................ ***Error! Bookmark not defined.***

Figure 6-7 An illustration of the external and internal normalised conversion efficiencies of PPSF. ***Error! Bookmark not defined.***

Figure 6-8 Second harmonic tuning curve of device ASCR 148 obtained with low power CW tuneable laser source. The measurement was performed by Dr. Corbari from physical optics group. .... ***Error! Bookmark not defined.***

Figure 6-9 Experimental setup of the all-fibre frequency-doubled fibre laser. ***Error! Bookmark not defined.***

Figure 6-10 The spectra of the TLS after the EOM phase modulator when the phase modulation is in OFF (blue line) and ON (green line) states.. ***Error! Bookmark not defined.***

Figure 6-11 The output spectra from the MOPA source at 4 different average output power levels with OSA resolution of (a) 2nm and (b) 0.02 nm.. ***Error! Bookmark not defined.***

Figure 6-12 The output pulse shape with ~462 ps FWHM pulse width........ ***Error! Bookmark not defined.***

Figure 6-13 An illustration of the pulse generated with EOM and the residual interpulse cw component due to finite EOM extinction ratio. .... ***Error! Bookmark not defined.***

Figure 6-14 The output spectra at 5.24 W average power in 3 different modes of operations. .... ***Error! Bookmark not defined.***

Figure 6-15 Average second harmonic power measured as a function of the average fundamental power in (a) linear scale and (b) logarithmic scale. The optimal QPM wavelength is optimised during the experiment. .... ***Error! Bookmark not defined.***

*Figure 6-16 The SH power generated at 3 different EOM modes of operations.****Error! Bookmark not defined.***

Figure 6-17 (a) Average second harmonic power and (b) optimal QPM wavelength measured as a function of fundamental power for the ASCR 148. .... ***Error! Bookmark not defined.***

Figure 6-18 The output spectra of the FH during the wavelength tuning and (b) the corresponding SH spectra. .... ***Error! Bookmark not defined.***

Figure 6-19 Conversion efficiency of the second harmonic as a function of internal FH power .... ***Error! Bookmark not defined.***

Figure 6-20 The average second harmonic power as a function of fundamental power measured directly at 3 different wavelength settings. The blue curve shows the SH power at the optimal QPM wavelength. The red and green curves show the SH power at the minimum and maximum tuning wavelengths shown in Figure 6-17 (b). .... ***Error! Bookmark not defined.***

*Figure 6-21 The tuning characteristics of the ASCR 148 before and after high power experiment. Measurement was performed by Dr. Corbari from physical optics group....****Error! Bookmark not defined.***

Figure 6-22 (a) The FH pulse shape with the peak power determined by fitting the area under the measured pulse shape to the measured pulse energy with ~462 ps FWHM. The InGasAs photodiode used (Agilent 83440 D) has a rise and fall time of <16 ps. (b) The red curve is the SH pulse shape (FWHM=416 ps) calculated with the FH pulse shape shown in sub-figure (a) using Eq.(6-22). The blue curve is the fitted SH pulse shape (FWHM~400ps) with the peak power determined by fitting the area under the measured pulse shape to the measured pulse energy. The measured pulse shape is considered as the electrical response of the silicon photodiode (shown in the inset) with width of up to ~920 ps. The silicon photodiode used (Thorlabs DET02AFC) has a rise and fall time of 50 ps and 250 ps respectively. .... ***Error! Bookmark not defined.***

*Figure 6-23 The setup of the FH source with operating wavelength around 1550 nm.****Error! Bookmark not defined.***

Figure 6-24 The normalised spectra at the various ports of the fibrised polarisation beam splitter (F-PBS) showing the effect of ASE filtering based on polarisation. .... ***Error! Bookmark not defined.***

Figure 6-25 The output spectra from the MOPA source at 4 different average output power levels with OSA resolution of 2 nm. .... ***Error! Bookmark not defined.***

Figure 6-26 The voltage response of the photodetector (Agilent 83440) increases linearly with the average FH power.. ***Error! Bookmark not defined.***

Figure 6-27 Tuning characteristic of the FORC6-L4 before and after high power test. Measurement was performed by Dr. Corbari from physical optics group. .... ***Error! Bookmark not defined.***

Figure 6-28 The evolution of the ratio of the PPSF normalised efficiency to its pristine value at different input FH power $P_{input}(\omega)$ during the high power operation. .... **Error! Bookmark not defined.**

Figure 6-29 Transmission spectra of pristine sample (blue), uniformly poled sample (red) and PPSF sample (green). The black dashed line indicates the spectral position of 800 nm. Note that the spectral shape of the white light source used for the measurement has been removed. Measurement was performed by Dr. Corbari from physical optics group. .... **Error! Bookmark not defined.**

Figure 6-30 Transmission spectra of PPSF before (red) and after (blue) the high power operation. The black dashed line indicates the spectral position of 800 nm. Measurement was performed by Dr. Corbari from physical optics group. .... **Error! Bookmark not defined.**

Figure 6-31 The schematic for the hypotheses to explain the reduction of the normalised conversion efficiency and the transmission loss of PPSF after the high power experiment. **Error! Bookmark not defined.**

Figure 8-1 An illustration of the relationship between the IC concentration and the ion population density in a simple case where 4 ICs are in state I and 3 ICs are in state II. The notation $N_{E,S}$ represents the ion concentration at energy level E in the state S. *107*

List of tables

Table 1 The normalised propagation constants of the guided modes in a step index fibre with V=8.1..... 10

Table 2 Comparison of the properties of the LP_{01} mode in step index fibre with 40 μm core size but different V-numbers.. 12

Table 3 Main parameters for the simulation of the Q-switched fibre ring lasers shown in Figure 3-2..... 48

Table 4 Recent progress in high average power erbium doped fibre lasers and amplifiers 70

Table 5 Summary of key results for various schemes for 1 W input signal and 100 W input pump........... 78

*Table 6 Summary of the progress in SH power and conversion efficiency of the PPSF**Error! Bookmark not defined.***

DECLARATION OF AUTHORSHIP

I, Ee Leong Lim

declare that the thesis entitled

Pump conditioning and optimisation for erbium doped fibres and their applications

and the work presented in the thesis are both my own, and have been generated by me as the result of my own original research. I confirm that:

- this work was done wholly or mainly while in candidature for a research degree at this University;
- where any part of this thesis has previously been submitted for a degree or any other qualification at this University or any other institution, this has been clearly stated;
- where I have consulted the published work of others, this is always clearly attributed;
- where I have quoted from the work of others, the source is always given. With the exception of such quotations, this thesis is entirely my own work;
- I have acknowledged all main sources of help;
- where the thesis is based on work done by myself jointly with others, I have made clear exactly what was done by others and what I have contributed myself;
- parts of this work have been published (see List of Publications).

Ee Leong Lim

Sep 2012

Acknowledgements

I am extremely grateful to my supervisor, Prof. David Richardson, for offering me the ORC PhD scholarship. I am also thankful to him for always keeping on top of my research progress and providing unwavering support and guidance. I would like to thank my co-supervisor, Dr Shaif-ul Alam, for developing me with valuable skill sets in fibre laser and saving me from being carried away by minor details and losing sight of the overall research goal. I am grateful to both of them for spending so much time out of their busy schedule to guide and teach me the process of research.

I am fortunate to work with many members of pulsed fibre lasers group who have shared with me their experiences in splicing, free-space alignment and equipment, in particular Dr Dejiao Lin, Dr Kang Kang Chen, Mr Simon Teh Peh Siong and Mr Zhihong Li. I also like to thank Dr Jonathan Price, who always critically reviews my results and allows me to think more sharply.

I am grateful to my collaborators in the research in periodically poled silica fibre (PPSF), i.e., Prof. Peter Kazansky, Dr Morton Ibsen and Dr Costatino Corbari. In particular, I have learned much from the insightful discussions with Dr Costatino Corbari.

My research is also made possible by the generosity of Prof. Johan Nilsson, Prof. Periklis Petropoulos, Prof. Andy Clarkson, Dr. Jacob Mackenzie, Prof. Jayanta Sahu and many of their students who lend their equipment to me. I have also benefited from interaction with Dr. Christophe Codemard who has taught me many things about fibre amplifiers. I would also like to thank Mr. Simon Butler and Mr. Fadzilah (Adie) Lotffe for the great mechanical support for my experiments.

I will forever grateful to my wife, May Siu Mee Lin. She has supported me unconditionally and has made numerous sacrifices throughout my PhD study. Finally, I would like to dedicate my thesis to my wife and our parents, i.e., Lim Tian Han and Chu Jee Lian, Siu Chou Chong and Irene Ho Beng Sim.

List of abbreviations

AOM	Acousto-Optic Modulator
ASE	Arbitrary Waveform Generator
AWG	Continuous Wave
BP	Backward-pumping
CLS	Cladding pumping Scheme
CRS	Core Pumping Scheme
CW or cw	Continuous Wave
DC	Direct Current
DCA	Digital Communication Analyser
DCF	Double Clad Fibre
DND	Direct Nanoparticle Deposition
EDFA	Erbium Doped Fibre Amplifier
EOM	Electro-Optics Modulator
Er	Erbium
ESA	Excited State Absorption
EYDF	Erbium-Ytterbium (co-)Doped Fibre
EYDFA	Erbium-Ytterbium (co-)Doped Fibre Amplifier
EYDFL	Erbium-Ytterbium (co-)Doped Fibre laser
FA	Fibre Amplifier
FBG	Fibre Bragg Grating
FH	Fundamental Harmonic
Final-amp	Final Stage Amplifier
FORC	Fibre Optics Research Center
FP	Forward-pumping
FWHM	Full Width at Half Maximum
FWM	Four Wave Mixing
GVD	Group Velocity Dispersion
GVM	Group Velocity Mismatched
HUC	Homogenous Upconversion
IP-EDFA	In-band Pumped Erbium Doped Fibre Amplifier
LBO	Lithium Triborate
LIDAR	Light Detection And Ranging
LMA	Large Mode Area
LP	Linearly Polarized (mode)
MCVD	Modified Chemical Vapour Deposition
MFD	Mode Field Diameter
MI	Modulation Stability

MMF	Multimode Fibre
MO	Master Oscillator
MOPA	Master Oscillator Power Amplifier
MPP	Multiple-Peak Phenomena
NA	Numerical Aperture
Nd	Neodymium
NLSE	Nonlinear Schrödinger Equation
OC	Output Coupler
OPU	Optical Processing Unit
ORC	Optoelectronics Research Centre
OSA	Optical Spectrum Analyser
OSNR	Optical Signal To Noise Ratio
PBS	Polarizing Beam Splitter
PC	Polarisation Controller
PCE	Power Conversion Efficiency
PIQ	Pair Induced Quenching
PMC	Perfect Phase Matching Condition
PPLN	Periodically Poled Lithium Niobate
PPSF	Periodically Poled Silica Fibre
Pre-amp	Preamplifier
QPM	Quasi-Phase Matching
RE	Rare Earth
RF	Radio Frequency
RF gen	Radio Frequency Generator
RIP	Refractive Index Profile
SBS	Stimulated Brillouin Scattering
SBSR	Sideband Suppression Ratio
SH	Second Harmonic
SHG	Second Harmonic Generation
SMF	Single Mode Fibre
SMSR	Side-Mode Suppression Ratio
SON	Second Order Nonlinearity
SPI	Southampton Photonics Inc.
SPM	Self-Phase Modulation
SRS	Stimulated Raman Scattering
TBP	Tuneable Bandpass Filter
TDFL	Thulium Doped Fibre Laser
TFB	Tapered Fibre Bundle

TLS	Tuneable Laser Source
Tm	Thulium
UV	Ultra-Violet
VCO	Voltage Controlled Oscillator
WDM	Wavelength Division Multiplexer
XPM	Cross Phase Modulation
Yb	Ytterbium

Chapter 1 Introduction

1.1 The motivation

Among the rare earth doped fibre lasers, the Yb^{3+}-doped fibre laser (YDFL) that emits radiation at ~1.0 μm is the most advanced primarily due to the high absorption cross section at 9xx-nm pump wavelengths and the low quantum defect between the pump and the emitted radiation. One of the key technologies that enables the power scaling of fibre laser is the concept of double clad fibre (DCF) as shown in Figure 1-1. A DCF consists of a rare earth doped core, an inner cladding and an outer cladding layer. In the DCF, the area of the pump guiding inner cladding is larger than the rare earth doped core. Furthermore, the numerical aperture (NA) of the inner cladding is often higher than the signal guiding rare earth doped core. Both the larger area and the higher NA of the inner cladding greatly facilitate the coupling of pump power from multimode laser diode into the rare earth doped core where the signal power is generated. This type of pumping configuration is known as cladding pump scheme (CLS). In contrast, when the pump and signal light are both guided in the rare earth doped core, it is known as the core pumping scheme (CRS). Due to the difference in the pump light guiding mechanism, the pump intensity in the CLS is lower than the CRS for a given pump power. Typically, the cladding pump absorption is typically estimated to be lower than core pump absorption by a factor given by the area ratio of core and inner cladding [1]. With the CLS, the average output power from near-diffraction limited YDFL reaches milestone of ~10 kW average output power in year 2009 [2].

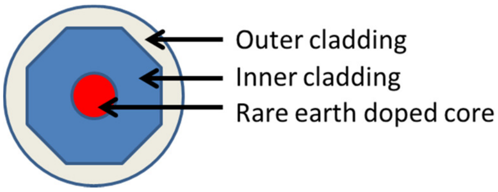

Figure 1-1 An illustration of DCF with octagonal shaped inner cladding.

While this rapid growth of YDFLs has led to many applications, these are mainly limited due to safety reasons to situations where atmospheric propagation of laser beams is not needed, or at least can be performed in a highly controlled environment. The invisible emission wavelength of YDFL at ~1 μm can transmit through the human eye without much attenuation and burn the most sensitive part of the eye, the retina. Conversely, light from erbium doped fibre lasers (EDFLs) that emit at ~1.55 μm is strongly absorbed in the cornea as well as lens and therefore will not reach the retina. According to the testing standard EN207, the maximum permissible exposure (MPE) to EDFLs is at least two orders of magnitude higher than YDFLs. Therefore, EDFLs are often called “eye-safe” lasers and they offer immediate advantages in applications where atmospheric propagation of a laser beam in an uncontrolled environment is a must.

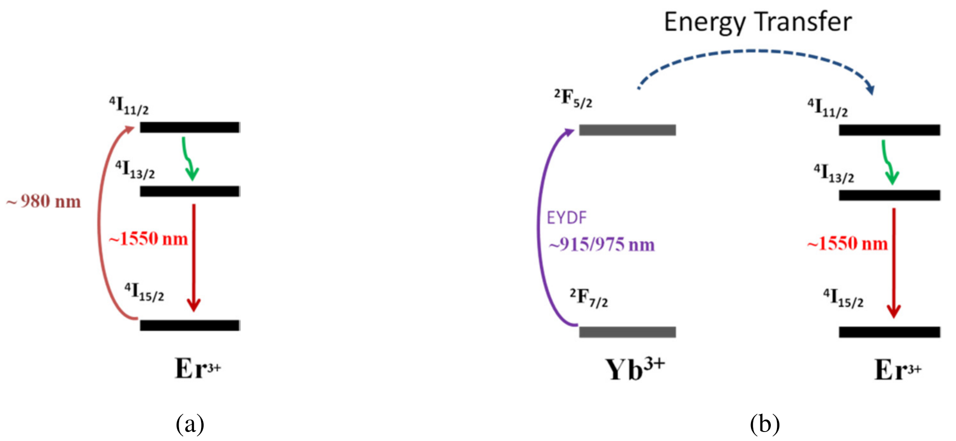

Figure 1-2 The energy level diagram of (a) the 980 nm pumped EDF (b) the 915/975 nm pumped EYDF to generate 1.55 µm.

For the generation of at ~1.55 µm radiation, an erbium doped fibre (EDF) is traditionally pumped at ~980 nm as illustrated in Figure 1-2 (a). However, due to the low absorption cross section, the pump absorption of the EDF in the CLS is so low that it is difficult to achieve sufficient pump absorption to reach high average power. To date, a maximum average power of only 70 W has been generated in CLS using the multimode pump laser diode module that capable of providing 500 W input pump power [3, 4].

The erbium doped fibre (EDF) has also been co-doped with ytterbium ions, which offers a much higher absorption cross section in the range of 900 nm to 980 nm. The pump power is initially absorbed by the Yb^{3+}-ions (purple line in Figure 1-2(b)) and is then non-radiatively transferred to the Er^{3+}-ions (blue dashed line in Figure 1-2(b)). Through this approach, an average power of ~297 W has been demonstrated from an erbium-ytterbium co-doped fibre laser (EYDF) [5]. However, further power scaling suffers from two problems. Firstly, the conversion efficiency of the EYDF approach is demonstrated to be at most ~40%. At 100 W output power level, then there will be ~ 150 W of heat generated that needs to be dissipated along the fibre to prevent the coating temperature from rising to ~80 ^{o}C under long term operation (beyond which damage is likely to occur) [6]. Next, secondary co-lasing of ytterbium ions occurs at higher power that can lead to catastrophic damages or at best reduced efficiency of ~19% as demonstrated by Y. Jeong et al [5]. These two drawbacks have impeded the further power scaling of the EYDF approaches.

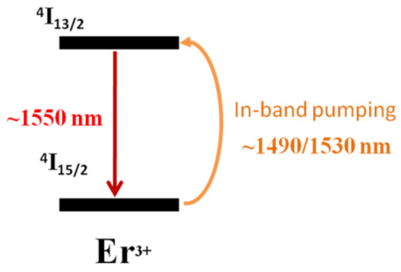

Figure 1-3 The energy level diagram of in-band pumped EDF to generate 1.55 µm.

Therefore, in this thesis, I investigated the in-band pumping (also known as tandem pumping or resonant pumping) to both eliminate the ytterbium co-lasing and to achieve high conversion efficiency. In this approach, the rare earth ions are directly pumped from the ground state ($^4I_{15/2}$- manifold) into the lasing level ($^4I_{13/2}$- manifold) as shown in Figure 1-3. In this way, with the pump and signal wavelength of 1535 nm and 1565 nm, the quantum defect is less than 2%.

Even though, direct laser diode pumped CLS would probably offer the highest electrical to optical conversion efficiency, a single mode fibre laser pumped CRS offers many other advantages. Firstly, the increase of pump absorption due to CRS allows the erbium doping concentration in the core of the erbium doped fibre (EDF) to be lowered. A lower erbium doping concentration reduces the concentration quenching problem in EDF (see Chapter 4). Secondly, as explained previously, the Er^{3+}-ions are often sensitised with Yb^{3+}-ions. The energy transfer between Yb^{3+}- and Er^{3+}-ions is efficient only if the fibre is co-doped with phosphorous, which in turn, results in an increase of NA and hence the number of guided modes. Therefore, it is a great challenge to have single-mode output and high pump absorption simultaneously in EYDF. In the CRS, the higher pump absorption enabled by the high brightness pump fibre laser may render the co-doping of ytterbium in EDF unnecessary which can lead to a lower NA and improved output beam quality. At the same time, the core diameter of the DCF can also be increased to increase the maximum extractable pulse energy (see Section 5.1.1) and to reduce the nonlinear coefficient (see Section 2.2.3.2) without degrading the beam quality. Thirdly, the higher pump absorption will reduce the amplifier length and, therefore, the effective nonlinear length.

Many applications, such as LIDAR and free space communication, require atmospheric propagation of “eye-safe” high energy pulses. Therefore, I also investigated the generation of high energy pulses using in-band pumped EDFLs.

For the high energy in-band pumped pulsed MOPA, I aim is to reduce the number of stages and therefore the system complexity through the use of a seed source with relatively high output energy. A Q-switched fibre laser that can generate relatively high pulse energy is well suited for this purpose. However, many high energy Q-switched fibre lasers in the literature suffer from the multiple peak phenomenon (MPP), where the Q-witched pulse is broken up into multiple sub peaks. Such a pulse is undesirable because it further develops along the master oscillator power amplifier (MOPA) chain and results in a pulse shape that is unsuitable for many applications [7]. Furthermore, the structured output pulse also complicates the interpretation of the experimental results obtained from MOPAs. Therefore, the MPP must be eliminated. Hence, I have also investigated the MPP in Q-switched fibre lasers and sought ways to eliminate it.

As previously discussed, the emission wavelength of a laser is so crucial that it is often one of the most important factors to consider when choosing a laser for a specific application. The limited possible emission wavelength range of rare earth doped fibre lasers is a major obstacle for many wavelength sensitive applications. Hence, nonlinear optical processes are often used to overcome this hurdle by converting the high average power emission from a fibre laser to wavelengths that are more suitable for a particular application. Nonlinear materials, such as Lithium Triborate (LiB_3O_5 or LBO) or periodically poled lithium niobate (PPLN), have been used to demonstrate high power nonlinear wavelength conversion with fibre lasers [8, 9]. However, the bulk nature of these nonlinear materials leads to the need for free space alignment and reduces system robustness. Therefore, I have also developed erbium doped fibre MOPAs to investigate second harmonic generation (SHG) based on periodically poled silica fibre (PPSF), which is essentially an optical fibre that exhibits second order nonlinearity.

In summary, the large demands for eye-safe wavelengths motivated me to investigate the impact of in-band pumping on “eye-safe” erbium doped fibre lasers for high power continuous wave operation and high energy low repetition rate operations with a particular interest in comparing the CLS and CRS. Meanwhile, as part of the development process of high energy low repetition rate EDFLs, I have also investigated the MPP in Q-switched fibre laser. Finally, I investigated SHG based on PPSF to broaden the accessible emission wavelength range and therefore the applications of the erbium doped fibre lasers.

1.2 Structure of the thesis

This thesis is structured as follow:

Chapter 2 describes the background knowledge that is commonly applicable across most of the chapters. Section 2.1 discusses the properties of optical fibres and the guided modes. Section 2.2 discusses optical nonlinearities. Section 2.3 introduces the erbium doped fibre amplifier with the emphasis on the application in high power fibre laser.

Chapter 3 describes the design and development of an all-fibre Q-switched laser that is subsequently used as the seed source for the MOPA presented in Chapter 5. Section 3.1 briefly introduced the behaviour of Q-switched lasers. Section 3.2 discusses the multiple-peak phenomenon in Q-switched fibre lasers whilst Section 3.3 discusses how the multiple-peak phenomenon affects the spectral evolution in a Q-switched fibre laser.

Chapter 4 describes the in-band pumped erbium doped fibre amplifier in continuous wave operation. Section 4.1 discusses the background for this chapter, which covers the net cross section concept and ion-ion interactions in erbium doped fibre. Section 4.2 presents the state of the arts in high average power erbium doped fibre laser. Section 4.3 presents the characteristics of the 1535 nm pump fibre laser used in this chapter and Chapter 5. Section 4.4 and 4.5 presents experimental and simulation results on this topic.

Chapter 5 describes the in-band pumped erbium doped fibre amplifier for the generation of high energy pulses. Section 5.1 discussed the background for this chapter whilst Section 5.2 presents the state of the arts in high energy erbium doped fibre lasers. Section 5.3 presents the experimental setup used in this chapter. Section 5.4 and 5.5 present the experimental and simulation results.

Error! Reference source not found. describes the work on nonlinear wavelength conversion using PPSF. Section **Error! Reference source not found.** describes the operational principle of PPSF. Section **Error! Reference source not found.** presents the state of the arts in the high power and high efficiency second harmonic generation with PPSF. Section **Error! Reference source not found.** presents the first demonstration of Watt-level average power from a PPSF while Section **Error! Reference source not found.** investigates the degradation of PPSF observed under high power operation.

Chapter 6 summarises the results obtained during my research and outlines possible future directions.

Chapter 2 Background

This chapter discusses the background required to understand the subsequent chapters.

An optical fibre is a cylindrical waveguide that is formed by the co-centric core and cladding sections. The refractive index of the core is higher than the cladding such that light can be guided by the process of total internal reflection [10]. Section 2.1 introduces how light is guided in an optical fibre and the corresponding guidance properties. The presence of an optical field in an optical fibre induces a polarisation due to the response of the material. This polarisation can become nonlinear when the optical field is sufficiently strong. Section 2.2 discusses the origin of this induced polarisation whilst Section 2.2.3 discusses how it modifies the guidance property of the optical field inside the optical fibre. In order to achieve light amplification, rare earth ions, such as Er^{3+} and Yb^{3+}, are often doped into the core of the optical fibres. These rare earth ions are excited by the pump field to provide the energy required for the amplification of the signal field. Section 2.3 describes the amplification of the light by rare earth ions and the working principles of high power erbium doped fibre lasers and amplifiers.

2.1 Optical properties of optical fibres

It is important to understand the optical properties of an optical fibre to understand the optical processes that occur in it. The detailed description and derivation of the fibre modes can be found in various text books [10, 11]. Therefore, only the characteristics of the optical fibres that are most relevant to this thesis will be highlighted. Section 2.1.1 discusses some of the important equations that describe the optical properties of optical fibres. The governing equations for the guided modes in a weakly guided step index fibre are presented in Section 2.1.2. The fibre modes in a weakly guided step index multimode optical fibre are discussed in Section 2.1.3. Finally, the refractive index profile of an actual fibre and its guided modes are discussed in Section 2.1.4.

2.1.1 Wave equations for optical fibres

Like all other electromagnetic problems, the optical field in an optical fibre is governed by Maxwell's equations and the associated boundary conditions. In a nonmagnetic medium, the Maxwell's equations can be represented by the following equation [10, 11]:

$$\nabla^2 E - \frac{1}{c^2}\frac{\partial^2}{\partial t^2}E = \frac{1}{\epsilon_0 c^2}\frac{\partial^2 P}{\partial t^2}, \qquad (2\text{-}1)$$

where E is the electric field, t is the time, c is the speed of light and P is the induced polarisation. The induced polarisation characterises the response of the material to the optical field and will be further discussed in Section 2.2.

When the nonlinear component of P is small compared to the linear component, Eq. (2-1) can be simplified to the well-known Helmholtz equation:

$$\nabla^2 E + n^2(r,\omega)\frac{\omega^2}{c^2}E = 0, \tag{2-2}$$

where $n(r,\omega)$ is the radial refractive index distribution, r is the radial position and ω is the frequency of the optical field.

Assuming the envelope of the optical field is varying slowly and the optical fibre is circularly symmetric, the electric field can be written as a function of independent variable:

$$E(r,\omega) = A(\omega)F(r)exp(i\beta_0 z), \tag{2-3}$$

where $F(r)$ is the transverse field distribution of the fibre mode, $exp(\pm im\phi)$ is the angular dependence term, $A(\omega)$ is the amplitude of the field that varies along the z-axis of the fibre and the term $exp(i\beta_0 z)$ contains the phase modulation with β_0, the propagation constant.

With Eq.(2-3), the Eq. (2-2) can be solved by the method of the separation of variables that leads to the following two equations [10, 12]:

$$\frac{\mathrm{d}^2 F}{\mathrm{dr}^2} + \frac{1}{r}\frac{\mathrm{dF}}{\mathrm{dr}} + \left(k_0^2 n^2(r) - \beta^2 - \frac{l^2}{r^2}\right)F = 0, \tag{2-4}$$

$$2i\beta_0\frac{dA}{dz} + (\beta^2 - \beta_0^2)A = 0, \tag{2-5}$$

where k_0 is the wave number given by $\frac{2\pi}{\lambda_0}$, λ_0 is the free space wavelength, l is the azimuthal mode number, β is the eigenvalue of Eq. (2-4) and, therefore, the propagation constant of the fibre mode (the difference between β and β_0 will be explained below). The fibre modes describe the transverse electromagnetic field distribution in an optical fibre and the propagation of light therein.

Equation (2-4) is independent of the propagation direction of the optical field. For a particular fibre structure, the fibre modes can be determined from the boundary conditions, i.e., in the absence of free electric charges and currents, the tangential components of the electric and magnetic fields and the normal components of the electric and magnetic flux densities must be continuous [13].

Equation (2-5) describes the variation of the amplitude of the optical field, A, along the propagation direction, i.e., the changes in the optical pulse properties, as it propagates along the fibre. The β_0 in Eq. (2-5) is the value of β in the absence of dispersion and Kerr-nonlinearity. Both dispersion and Kerr-nonlinearity modify the propagation constant of the fibre mode (β) and lead to changes in optical spectrum and pulse shape. In the literature, the "modified" version of Eq. (2-5), which considers the third order nonlinearity and dispersion, can be derived into the nonlinear Schrödinger equation (NLSE) [12].

2.1.2 Weakly guided step index fibres

In a weakly guided step index fibre, the core and the cladding refractive indices are approximately equal to each other, i.e., $n_1 \approx n_2$, where n_1 and n_2 are the core and cladding refractive indices of a step index fibre. Under this condition, the guided fibre modes are nearly transverse, i.e., the electric field along the propagation direction is close to zero. In a step index fibre, the refractive index profile is characterised by:

$$\begin{aligned} n(r) &= n_1 \qquad 0 < r < a \qquad \text{core,} \\ &= n_2 \qquad r > a \qquad \text{cladding.} \end{aligned} \tag{2-6}$$

With this refractive index profile, the corresponding transverse dependence of the guided fibre modes can be obtained by solving Eq. (2-4) and expressed as [10]:

$$\psi(r,\phi) = \begin{cases} \frac{A}{J_l(U)} J_l\left(\frac{Ur}{a}\right)\begin{bmatrix}\cos l\phi \\ \sin l\phi\end{bmatrix}; & r < a \\ \frac{A}{K_l(U)} K_l\left(\frac{Wr}{a}\right)\begin{bmatrix}\cos l\phi \\ \sin l\phi\end{bmatrix}; & r > a \end{cases} \tag{2-7}$$

where ψ is the transverse component of the electric field (E_x or E_y), A is the normalisation constant as determined by the optical power guided in the mode, $J_l(U)$ is the Bessel function of first kind for integer order of l, $K_l(U)$ is the modified Bessel functions of second kind with integer order of l. The variable U and W are defined as:

$$U = a(k_0^2 n_1^2 - \beta^2)^{\frac{1}{2}}, \tag{2-8}$$

$$W = a(\beta^2 - k_0^2 n_2^2)^{\frac{1}{2}}, \tag{2-9}$$

and the normalised waveguide parameter V can be defined as:

$$V = (U^2 + W^2)^{\frac{1}{2}} = k_0 a(n_1^2 - n_2^2)^{\frac{1}{2}}, \tag{2-10}$$

where a is the core radius. For a given a V-number, many properties of a step index fibre can be explained. Furthermore, the numerical aperture (NA) of a fibre is defined as:

$$NA = (n_1^2 - n_2^2)^{\frac{1}{2}} \ . \tag{2-11}$$

In the above equations, the propagation constant for the mode, β, is the only unknown parameter. It can be determined by considering the continuity of $\frac{\partial \phi}{\partial r}$ at $r = a$, which results in the following characteristic equation:

$$\frac{UJ_l'(U)}{J_l(U)} = \frac{WK_l'(W)}{K_l(W)}. \tag{2-12}$$

By solving Eq. (2-12), the β parameter for each fibre modes can be obtained. Mathematically, β is the eigenvalue of each of the fibre modes and the fibre mode is the corresponding eigenvector. For a given value of l, there will be a finite number of solutions, and the fibre mode corresponds to the m^{th} solution is referred to as the LP$_{lm}$ mode. It is useful to remember that when $V < 2.405$, there is only one eigenvalue that can be found from Eq. (2-12), which means that the fibre guides only one mode and is designated as the LP$_{01}$ mode.

Finally, it is convenient to define the normalised propagation constant as:

$$b = \frac{\frac{\beta^2}{k_0^2} - n_2^2}{n_1^2 - n_2^2}. \tag{2-13}$$

For the guided modes, it can be shown that $0 < b < 1$. The higher the b-value, the stronger is the mode guidance in the fibre.

2.1.3 Fibre modes in multimode fibres

In this section, we discuss some of the modal properties of a multimode step index fibre that operates at $1.55\ \mu m$ with $NA = 0.1$ and $2a = 40\ \mu m$ corresponding to a V-value of ~8.11. These parameters are chosen because it corresponds to the V-number of the large mode area Er-doped fibre used in Chapter 4 and Chapter 5.

Using Eq. (2-12), it is possible to obtain 10 different values of β for this fibre. The corresponding b-values are listed in Table 1. The normalised intensity distributions of the first six LP-modes are shown in Figure 2-1. Even though there are many guided modes, the exact modes present in a fibre depend on the modal excitation condition. The LP_{01} is typically the most desirable mode for fibre laser because the output beam is similar to the Gaussian beam profile, which is useful for many applications. The LP_{11} is typically generated if there is a lateral offset when two fibres are fusion-spliced together. In the absences of lateral offset, the pure LP_{01} from the single-mode input fibre can still be coupled into the LP_{02} due to the centro-symmetric nature of LP_{01} and LP_{02} modes [11].

Table 1 The normalised propagation constants of the guided modes in a step index fibre with *V*=8.1

Mode	LP_{01}	LP_{11}	LP_{21}	LP_{02}	LP_{31}	LP_{12}	LP_{41}	LP_{22}	LP_{03}	LP_{51}
b	0.9305	0.8241	0.6856	0.6389	0.5175	0.4235	0.3321	0.1860	0.1492	0.1024

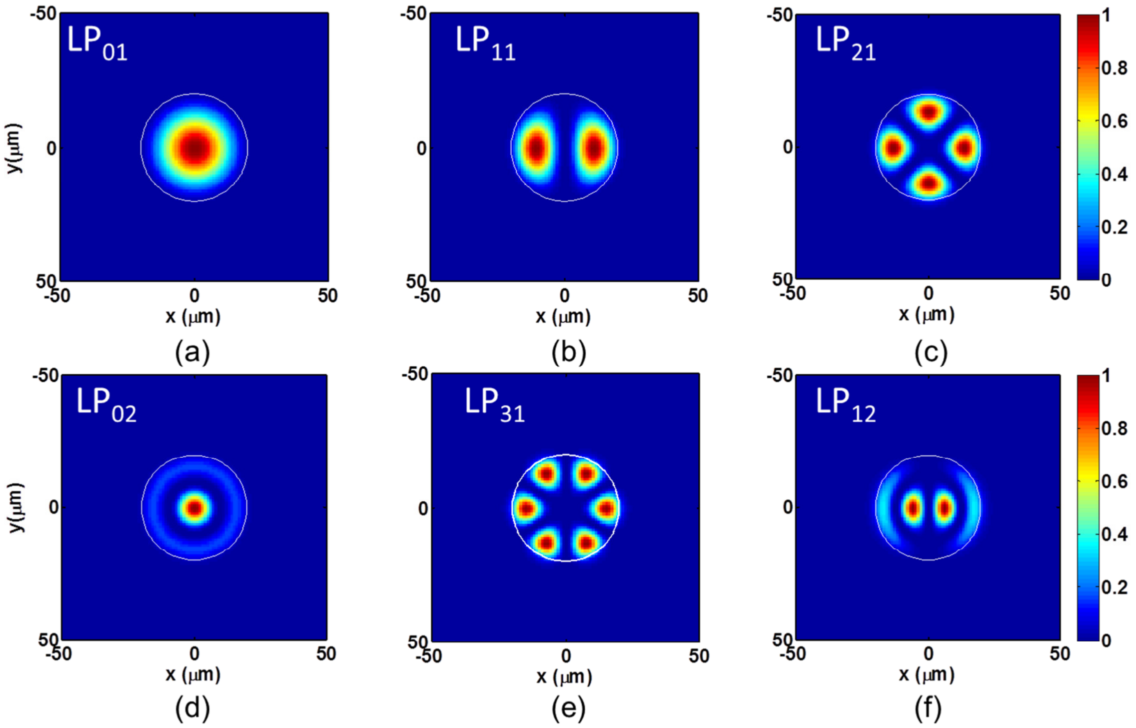

Figure 2-1 The normalised intensity distribution of the first 6 LP-modes of a step index fibre with V=8.1. The white circular lines outline the fibre core with diameter of 40 μm.

For the case of LP$_{01}$, the mode radius, w_0, is the radius where the intensity has dropped to $\frac{1}{e^2}$ of the intensity on the beam axis and $2w_0$ is known as the mode field diameter (MFD). The effective mode area (A_{eff}) for LP$_{01}$ is defined as [10]:

$$A_{eff} = \pi w_0^2 \, . \tag{2-14}$$

The MFD of the LP$_{01}$ mode shown in Figure 2-1(a) is estimated to be 32 μm corresponding to A_{eff} of 804 μm^2.

Now, we examine the effect of V values on the characteristics of the LP$_{01}$ mode in a step index fibre with the same core radius. The intensity mode profiles of the LP$_{01}$ mode for different V values ($V \approx$ 2.35, 3.98 and 8.11 at 1.55 μm) are shown in Figure 2-2 and their corresponding properties are outlined in Table 2. In the case of $V \approx 2.35$, the single mode condition (V<2.403) is satisfied, therefore, the fibre supports only the LP$_{01}$ mode and exhibits a b-value of 0.0975 and an MFD of 80 μm. The low b-value implies that the LP$_{01}$ mode in this case is weakly guided. When $V \approx 3.98$, the b-value becomes 0.4143 and the MFD reduces to 44 μm. Table 2 shows that as the V-number increase from 2.35 (red plot in Figure 2-2) to 8.11 (blue plot in Figure 2-2), the ratio of power remain in the core increases from ~69% to ~99%. On the other hand, the normalised intensity decreases from 1.00 (at the centre of the core) to 0.51 (at the core/clad interface) when $V = 2.35$. Similarly the normalised intensity decreases from 1.00 at the core centre to 0.02 at the core/clad interface when $V = 8.11$. Therefore, as the V-number increases, the LP$_{01}$ modal intensity within the fibre core increases. This increase of LP$_{01}$ modal intensity as the V number increases will be further discussed in Section 5.5. It is to be noted here that the low NA values listed in the Table 2 is chosen only for understanding the changes in intensity profile of the LP_{01} mode of a 40 µm core step index fibre operating at 1.55 µm with V-values of 2.35, 3.98 and 8.11. In practive, the NA of a step index fibre is always choosen to be >0.06 to avoild excessive bend loss [14].

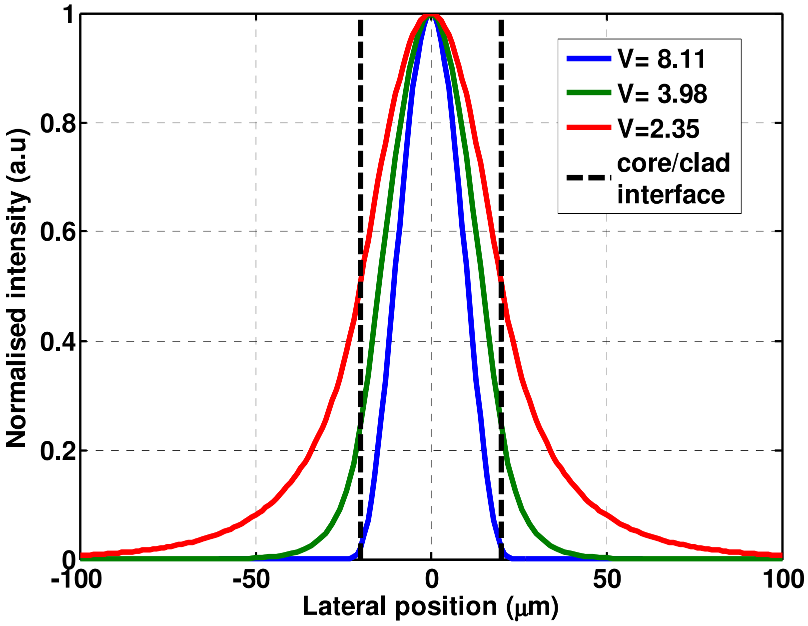

Figure 2-2 Comparison of the LP_{01} modes of step index fibres with same core diameter but different *V*-numbers. The intensity is normalised to the intensity peak of the respective mode.

Table 2 Comparison of the properties of the LP_{01} mode in step index fibre with 40 µm core size but different *V*-numbers.

Normalised frequency, V	2.35	3.98	8.11
Numerical aperture, NA	0.0145	0.0246	0.1000
Normalised propagation constant, b	0.0975	0.4143	0.9305
Mode field diameter, MFD	80 µm	44 µm	32 µm
Percentage of power in core	69%	92%	99%
Normalised intensity at core/clad interface	0.51	0.25	0.02

2.1.4 Guided modes in actual fibres

In the previous sections, the properties of a step index fibre have been discussed. However, the refractive index of actual fibre differs from step index profile. In this section, we show the guided modes of the large mode area fibre (Liekki Er-60-40/140) used in Chapter 4 and Chapter 5. The fibre is specified to have a core and cladding diameter of 40 µm and 140 µm respectively with core NA of ~0.1.

Figure 2-3(a) shows the refractive index difference of the fibre along the radial position. The fibre exhibits a two-step index profile. The core region is located between radial positions 0-20 µm. The first and second cladding layers are formed between radial positions 22-50 µm and 55-70 µm. Within the core region (<20 µm), the refractive index gradually decreases toward the centre before a sharp rise at the centre of the core. The index different between the core and the first cladding region corresponds well with the specified NA of the fibre.

With the refractive index profile, the guided modes can be simulated numerically, for example using the transfer matrix method [15] and the implementation of this method can be found in the commercial software Optiwave optisystem version 10. The normalised intensity profiles of all guided modes are shown in the Figure 2-3(b). The mode profile of the LP_{01} closely follows the refractive index profile and exhibits a MFD of ~ 37 µm.

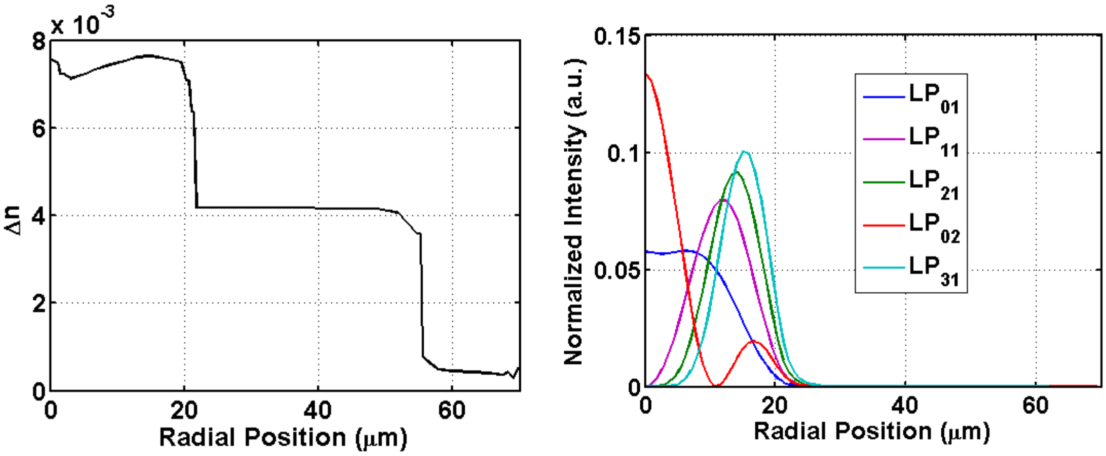

(a) (b)

Figure 2-3 (a) The refractive index difference of Liekki Er-60-40/140 along the radial position provided by the fibre manufacturer (Liekki) and reconfirmed in-house by Mr Robert Standish (b) The radial intensity distribution (normalised to the same power) of the first 5 LP-modes calculated using transfer matrix method.

2.2 Optical nonlinearity

2.2.1 Nonlinear induced polarisation

A useful model to describe the optical nonlinearity is to consider the induced polarisation P by the incident field E as below [12]:

$$P = \varepsilon_0\left(\chi^{(1)}E + \chi^{(2)}E^2 + \chi^{(3)}E^3 + \cdots\right), \tag{2-15}$$

where $\chi^{(1)}$ denotes the linear susceptibility, and the quantities $\chi^{(2)}$, $\chi^{(3)}$, ... are known as the nonlinear susceptibilities of the medium.

At low optical intensity, only the linear susceptibility is significant, i.e., the medium response is linear. Hence, the frequency of oscillation of the polarisation field is the same as the frequency of the incident field. At high optical intensity, the nonlinear susceptibilities start to become significant. Due to the nonlinear dependency on the incident field, the oscillation frequency of the induced polarisation can contain spectral components other than the incident frequency.

From Eq. (2-1), the interaction of an electromagnetic field with the linear and nonlinear induced polarisations can be described by the following equation [12, 16]:

$$\nabla^2 E - \frac{1}{c^2}\frac{\partial^2}{\partial t^2}E = \frac{1}{\epsilon_0 c^2}\frac{\partial^2}{\partial t^2}\left(P^L + P^{NL}\right), \tag{2-16}$$

where the induced polarisation has been separated into the linear (P^L) and nonlinear (P^{NL}) parts. In a lossless, isotropic, dispersive medium, the equation for each frequency component of the field can be expressed as [16]:

$$\nabla^2 E_n - \frac{\varepsilon_r(\omega_n)}{c^2}\frac{\partial^2}{\partial t^2}E_n = \frac{1}{\epsilon_0 c^2}\frac{\partial^2}{\partial t^2}P_n^{NL}, \tag{2-17}$$

where $\varepsilon_r(\omega_n)$ is the dimensionless frequency dependence relative permittivity which is different for each material and n is the index for the various frequency components. This equation has the form of the driven wave equation, where the left hand side is the applied electromagnetic field the right hand side arises due to the induced polarisation in the medium.

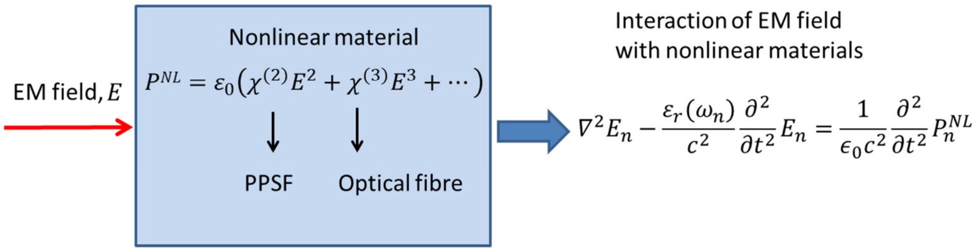

Figure 2-4 Electromagnetic wave incident on nonlinear medium induces a nonlinear polarisation. The interaction of the electromagnetic wave and the induced nonlinear polarisation can be described by Eq. (2-17). An example of $\chi^{(2)}$-medium is the periodically poled silica fibre (PPSF) and an example of $\chi^{(3)}$-medium is the optical fibre.

Figure 2-4 illustrates that an electromagnetic field incident on nonlinear medium can induce a nonlinear polarisation response. If the nonlinear induced polarisation (i.e., P_n^{NL}) for a given nonlinear process is known, it is then possible to describe the interaction of the nonlinear materials and the electromagnetic field by using Eq. (2-17).

In this chapter, I will focus our discussion on P_n^{NL} induced by the third order susceptibility $\chi^{(3)}$ since this is typically the lowest order nonlinearity that can be induced in silica optical fibre due to its inversion symmetry. However, in **Error! Reference source not found.**, I will show that the silica fibre can be engineered into a periodically poled silica fibre (PPSF) that exhibits $\chi^{(2)}$ nonlinearity.

2.2.2 Third order nonlinear processes

In this section, I will present the nonlinearly induced polarisation (i.e., P_n^{NL}) in an optical fibre ($\chi^{(3)}$-medium) and explain how it gives rise to the self-phase modulation (SPM), cross phase modulation (XPM) and four wave mixing (FWM).

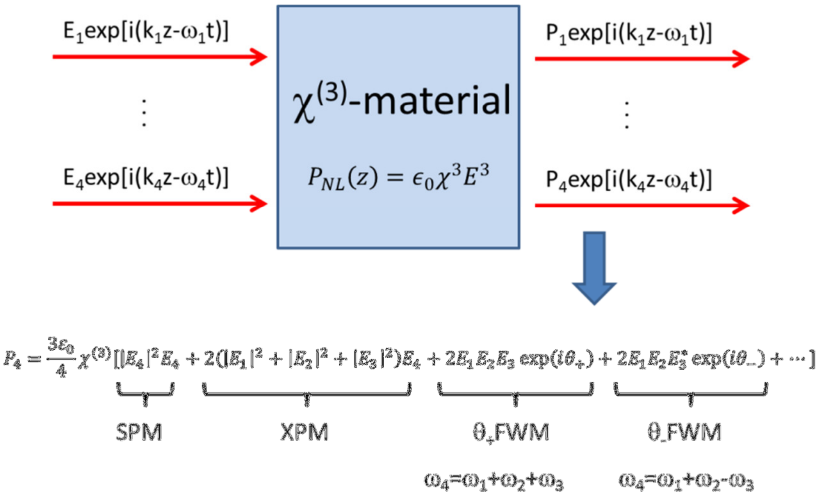

Figure 2-5 The nonlinear polarisation in $\chi^{(3)}$-medium gives rise to SPM, XPM and FWM.

When four linearly polarised optical waves oscillating at frequencies ω_1, ω_2, ω_3, and ω_4 incident on the nonlinear medium as illustrated by the left hand side of Figure 2-5, the total electric field can be written as:

$$E = \frac{1}{2}\hat{x}\sum_{j=1}^{4} E_j\, exp\big[i\big(k_jz - \omega_it\big)\big] + c.c. \tag{2-18}$$

where $\hat{x}$ is the polarisation unit vector. The P_n^{NL} arises from the response of the $\chi^{(3)}$-medium can then be expressed as [12]:

$$P_{NL}(z) = \epsilon_0\chi^{(3)}E^3\,. \tag{2-19}$$

If we substitute (2-18) into (2-19) and express $P_{NL}(z)$ in the same form of (2-18), we get:

$$P_{NL} = \frac{1}{2}\hat{x}\sum_{j=1}^{4} P_j \, exp\left[i\left(k_j z - \omega_i t\right)\right] + c.c, \tag{2-20}$$

where P_j is the induced nonlinear polarisation at the frequency ω_i. There will be four components within P_{NL} that oscillates at the frequency corresponding to each of the incident frequencies. Each of the P_j consists of a large number of terms involving the products of three waves. For example, the component of P_4 that oscillates at ω_4 can be expressed as:

$$P_4 = \frac{3\varepsilon_0}{4}\chi^{(3)}[|E_4|^2 E_4 + 2(|E_1|^2 + |E_2|^2 + |E_3|^2)E_4 + 2E_1E_2E_3 \exp(i\theta_+) + 2E_1E_2E_3^* \exp(i\theta_-) + \cdots], \tag{2-21}$$

where θ_+ and θ_- are defined as:

$$\theta_+ = (k_1 + k_2 + k_3 - k_4)z - (\omega_1 + \omega_2 + \omega_3 - \omega_4)t, \tag{2-22}$$

$$\theta_- = (k_1 + k_2 - k_3 - k_4)z - (\omega_1 + \omega_2 - \omega_3 - \omega_4)t. \tag{2-23}$$

Each of the terms in Eq. (2-21) corresponds to one type of nonlinear effect that can modify the field at ω_4 and are illustrated at the bottom of Figure 2-5. The first term is responsible for self-phase modulation (SPM). The overall effect of the SPM is that the field experiences a refractive index changes that is proportional to the optical intensity itself ($|E_4|^2$). This effect will be further discussed in Section 2.2.3 in the context of optical fibre.

The second terms are responsible for cross-phase modulation (XPM), where the refractive index seen by the optical field depends on the other fields. For example, in Eq. (2-21) , the refractive index of optical at ω_4 will depend on optical fields at ω_1, ω_2 and ω_3.

The two remaining terms correspond to two different types of four wave mixing (FWM) that can generate ω_4 from the combination of 3 other fields. The term containing θ_+ corresponds to the case in which three photons at ω_1, ω_2, ω_3 transfer their energy to a single photon at frequency $\omega_4 = \omega_1 + \omega_2 + \omega_3$, as illustrated in Figure 2-6(a). While the term containing θ_- corresponds to the case in which two photons at ω_1 and ω_2 are annihilated with simultaneous creation of two photons at frequencies ω_3 and ω_4, such that $\omega_1 + \omega_2 = \omega_3 + \omega_4$, as illustrated in Figure 2-6(b). These frequency relationships between the interacting fields essentially mean that the overall photon energy is conserved, as illustrated in Figure 2-7(a) in the case of θ_--FWM.

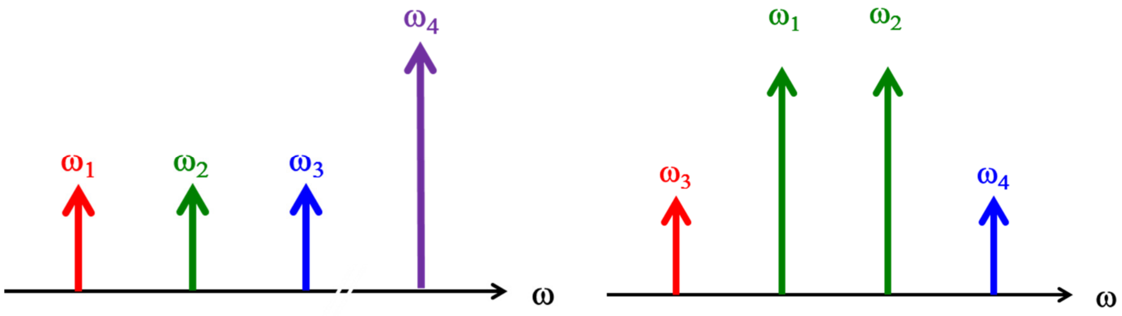

(a) (b)

Figure 2-6 (a) An example of θ_+-type FWM where frequency ω_4 is generated with the sum of ω_1, ω_2 and ω_3. (b) An example of θ_--type FWM where frequency ω_3 and ω_4 are generated with the sum of ω_1 and ω_2.

The efficiency of the two types of FWMs depend on the phase mismatch between E_4 and P_4, Δk, governed by first terms in Eqs. (2-22) and (2-23). For instance, the phase-matching requirement for the θ_+-type FWM is

$$\Delta k = k_1 + k_2 + k_3 - k_4, \tag{2-24}$$

and for the θ_--type FWM is

$$\Delta k = k_1 + k_2 - k_3 - k_4. \tag{2-25}$$

The Δk of the θ_--type FWM is illustrated in Figure 2-7(b).

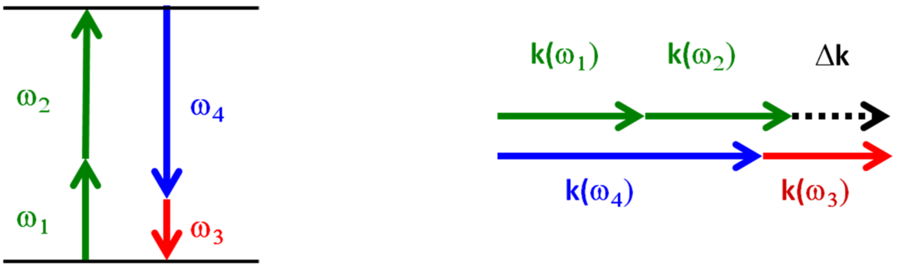

(a) (b)

Figure 2-7 An illustration of the energy conservation (a) and phase mismatch (b) diagrams of a θ_--type FWM.

When the phase-matching condition is fulfilled ($\Delta \mathrm{k} = 0$), the generated optical fields maintains a fixed phase relation with respect to the $P_{NL}(z)$ and is able to extract energy most efficiently from the incident waves [16]. For example, in the θ_--FWM, the $P_{NL}(z)$ corresponds to the term with θ_- in Eq. (2-21) while the generated optical fields oscillate at ω_3 and ω_4. As a result, the nonlinear polarisation and generated optical fields are synchronised in phase and gives rise to the maximum transfer of energy from the incident fields to the generated optical fields. However, when $\Delta \mathrm{k} \neq 0$, the nonlinear polarisation and the generated optical fields do not travel at the same phase velocity. In fact, their phase difference becomes π after a coherence length L_c given by:

$$L_c = \left|\frac{\pi}{\Delta \mathrm{k}}\right|. \tag{2-26}$$

In Section 2.2.3.3, I will discuss modulation instability (MI), which is a kind of θ_--type FWM, where the 2 pump photons in the FWM are degenerate, i.e., they are the same while the phase matching condition is fulfilled through the SPM and anomalous dispersion of the nonlinear medium. Furthermore, in Section 3.3, I demonstrate that the peak power of the Q-switched fibre laser is strong enough to induce the θ_--type FWM within the laser cavity during the build up of the Q-switched pulses.

2.2.3 Nonlinearities in optical fibre

In this section, the spectral- and the intensity-dependent response of the optical fibre to an optical pulse are described. In the scalar approach, the optical field of the pulse is assumed to maintain its polarisation along the fibre length so that the electric field vector, $\boldsymbol{E}(\boldsymbol{r},t)$, can be expressed as [12]:

$$\boldsymbol{E}(\boldsymbol{r},t) = \frac{1}{2}\hat{x}(F(x,y)\,\mathrm{A(z,t)}\exp[i(\beta_0 z - \omega_0 t)] + c.c), \tag{2-27}$$

where $\hat{x}$ is the polarisation unit vector, $F(x,y)$ is the transverse mode distribution, β_0 is the propagation constant at the carrier frequency ω_0. The $F(x,y)$ and β_0 can be determined from the Helmholtz equation with the boundary condition for a given fibre structure as described in Section 2.1.2. $\mathrm{A(z,t)}$ is the slowly varying pulse envelope and is chosen such that $|\mathrm{A(z,t)}|^2$ represents the optical power P(z,t).

The evolution of $\mathrm{A(z,t)}$ is determined by the response of the fibre to the pulse. In Section 2.2.3.1, the spectral-dependent response is first described. This leads to a phenomenon known as group velocity dispersion (GVD). Next, the intensity-dependent response is described, which leads to self-phase modulation (SPM). Section 2.2.3.3 describes the condition under which the interplay between the GVD and SPM lead to a phenomenon known as modulation instability (MI).

Afterwards, the stimulated Brillouin scattering and the stimulated Raman scattering are briefly described in Section 2.2.3.4 and 2.2.3.5 respectively. These processes belong to the inelastic nonlinear processes, whereby part of the energy of the incident photon is transferred to the nonlinear medium.

2.2.3.1 Chromatic dispersion

The spectral envelope of an optical pulse can be described by the Fourier transform of $\mathrm{A(z,t)}$, i.e., $\tilde{A}(\mathrm{z}, \omega - \omega_0)$. A fibre generally responds differently to different frequency components. As a result, the different frequency-components exhibit different propagation behaviours characterised by the spectral-dependent propagation constant $\beta(\omega)$. However, the exact functional form of $\beta(\omega)$ is rarely known. Therefore, it is approximated by using the Taylor's series about the carrier frequency ω_0 as [12]:

$$\beta(\omega) = \beta_0 + (\omega-\omega_0)\beta_1 + \frac{1}{2!}(\omega-\omega_0)^2\beta_2 + \frac{1}{3!}(\omega-\omega_0)^3\beta_3 + \cdots, \tag{2-28}$$

where

$$\beta_m = \left(\frac{d^m\beta}{d\omega^m}\right), \tag{2-29}$$

$$\beta_1 = \frac{1}{v_g}, \tag{2-30}$$

$$\beta_2 = \frac{d^2\beta}{d\omega^2} = \frac{d}{d\omega}\left(\frac{1}{v_g}\right). \tag{2-31}$$

The parameter β_1 corresponds to the inverse of the group velocity, which is the speed at which the envelope moves in the fibre and β_2 is known as the GVD parameter. When β_2 is nonzero, the different frequency components travel at different group velocities. This phenomenon is commonly known as group velocity dispersion in the literature.

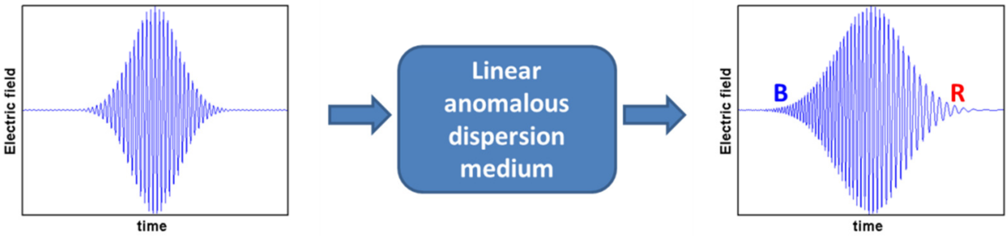

Figure 2-8 Temporal variation of the electric field of an optical pulse that spreads in a linear medium with anomalous dispersion; the shorter-wavelength component B has a larger group velocity and therefore travels faster than the longer-wavelength component R [13].

Figure 2-8 illustrates the optical pulse propagate in an anomalous dispersive medium ($\beta_2 < 0$) where the group velocity increases with frequency. This means that the blue-shifted (higher frequency/shorter wavelength) spectrum of the pulse will travel faster than those that are red-shifted. In contrast, the opposite happens in the normal dispersion regime where β_2 is positive. In the fibre optic literature, the dispersion parameter D is commonly used in place of β_2. The two parameters are related to each other through:

$$D = \frac{d\beta_1}{d\lambda} = -\frac{2\pi c}{\lambda^2}\beta_2. \tag{2-32}$$

where λ is the wavelength of the light. Typically, in an index-guided fibre, the dispersion property is mainly determined by the material of the fibre, which is silica. For SMF-28e fibre, the dispersion parameter is specified as $D \leq 18\frac{ps}{nm.km}$ at 1550 nm. The positive sign of D means that the fibre exhibits anomalous dispersion at around 1550 nm and the numerical value means that the light pulse of 1 nm FWHM-bandwidth will broaden by 18 ps after propagating along a 1 km length of the fibre.

Overall, in the frequency domain, the dispersion causes the different spectral components of the pulse to travel at different velocities but will not change the frequency content of the pulse in the absence of SPM. In the time domain, this will result in a change of pulse shape, which depends both on the properties of the pulse and the dispersion property of the fibre.

2.2.3.2 Self-phase modulation

In Section 2.2.2, I have discussed that the χ^3-nonlinearity of the medium can induced self-phase modulation (SPM). In this section, the intensity induced phase shift, and consequently the frequency shift, across the pulse due to SPM will be discussed.

In the slow varying envelope approximation and the assumption that the nonlinear induced polarisation is small compared to the linear induced polarisation, the change of refractive index due to SPM is given by [12]:

$$\tilde{n} = n + n_2|E|^2, \tag{2-33}$$

where

$$n_2 = \frac{3}{8}Re(\chi^{(3)}). \tag{2-34}$$

The n_2 has a value of ~$2.6 \times 10^{-20} m^2/W$ for silica.This kind of nonlinearity is also known as Kerr-nonlinearity in the literature.

When the electric field of a pulse, E, is represented by Eq. (2-27), the intensity of the optical pulse can be expressed as $I(z,t) = \frac{|A(z,t)|^2}{A_{eff}}$, where A_{eff} is the effective area of the mode and is a waveguide-structure dependent parameter defined as:

$$\mathrm{A_{eff}} = \frac{\left(\iint_{-\infty}^{\infty} |F(x,y)|^2 dxdy\right)^2}{\iint_{-\infty}^{\infty} |F(x,y)|^4 dxdy|}. \tag{2-35}$$

The change in the refractive index induced by the pulse intensity modifies the propagation properties of the pulse itself by introducing an intensity-dependent phase shift to different parts of the pulse envelope. In a lossless fibre, the intensity-dependent phase-shift, $\phi_{NL}(z,t)$, is expressed as [12]:

$$\phi_{NL}(z,t) = kn_2 I(z,t)z = \frac{kn_2 P(z,t)}{A_{eff}}z, \tag{2-36}$$

where $P(z,t)$ is the power profile of the pulse given by $|A(z,t)|^2$. Hence, $\phi_{NL}(z,t)$ is affected by the intensity dependent response through n_2 and is affected by the waveguide structure through A_{eff}. In the fibre optic literature, Eq. (2-36) is expressed as:

$$\phi_{NL}(z,t) = \gamma P(z,t)z, \tag{2-37}$$

where $\gamma = \frac{k_0 n_2}{A_{eff}} = \frac{2\pi n_2}{\lambda\, A_{eff}}$ is known as the nonlinear parameter. For SMF-28e fibre, the mode field diameter (MFD) at 1550 nm is $\sim 10.4\ \mu m$ corresponds to $\gamma \approx 1.2\ W^{-1}km^{-1}$.

Since the intensity varies across the pulse, the induced phase shift also varies across the pulse, which, in turn, results in a change in the spectral content of the pulse. The instantaneous angular frequency of the pulse, $\omega(t)$, is equal to the rate of change of the phase, i.e.:

$$\omega(t) = -\frac{d\phi}{dt}, \tag{2-38}$$

where the minus sign is due to the choice of the factor $\exp(-i\omega_0 t)$ in Eq. (2-27). Therefore the instantaneous frequency can be derived as

$$\omega(t) = -\frac{d}{dt}[(\beta_0 z - \omega_0 t) + \phi_{NL}],$$

$$\omega(t) = \omega_0 - \gamma z\,\frac{dP(z,t)}{dt}. \tag{2-39}$$

Eq. (2-39) shows that the SPM induced spectral change is related to the rate of change of the instantaneous power of the pulse. This spectral change illustrated in Figure 2-9 in a medium where $n_2>0$. At the leading edge of the pulse, the $\frac{dP(z,t)}{dt}$ is positive. Therefore, SPM will reduce the $\omega(t)$ to a lower than the initial value, i.e., a frequency down-shift, according to Eq. (2-39). Similarly, SPM will induce a frequency up-shift at the trailing edge of the pulse.

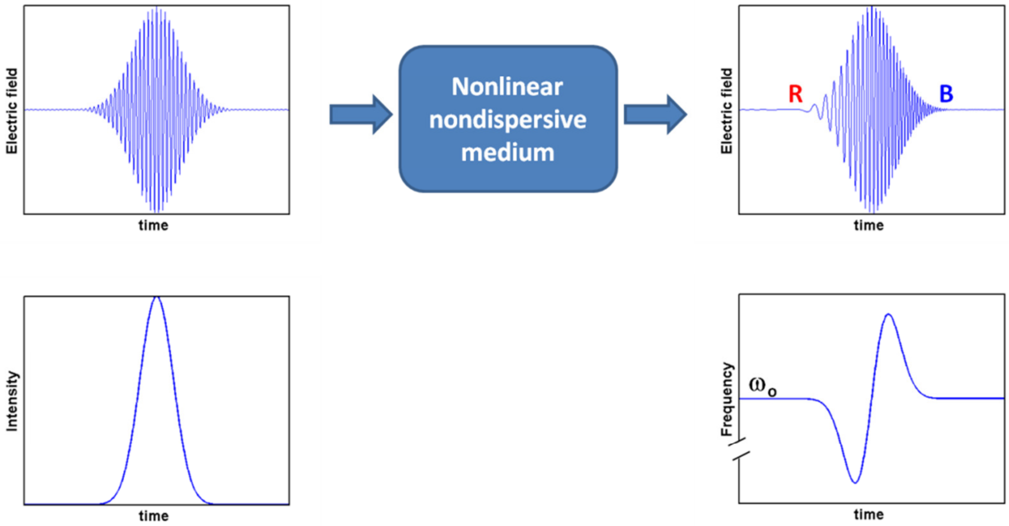

Figure 2-9 Temporal variation of the electric field of an optical pulse in a nonlinear nondispersive medium. The self-phase modulation ($n_2>0$) introduces a negative frequency shift at the leading half of the pulse (denotes R) and a positive frequency shift at the trailing half (denoted B). Even though the frequency across the pulse varies, its shape is not altered [13].

Overall, in frequency domain, new spectral-components are created due to SPM. In the time domain, this will not change the pulse envelope in the absence of GVD.

2.2.3.3 Modulation instability

In this section, I show that the combined effect of self-phase modulation and anomalous dispersion in an optical fibre can lead to a phenomenon known as modulation instability (MI). This is a θ_--type FWM, whereby 2 pump photons are degenerated, i.e., they are essentially the same as illustrated in Figure 2-10.

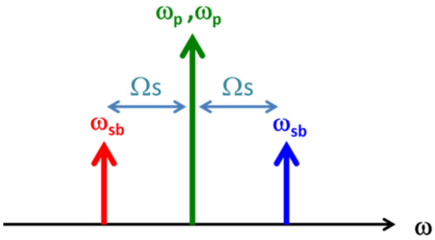

Figure 2-10 Modulation instability is a θ_--type FWM where the 2 pump photon are degenerate, create two sidebands at Ω_s away from the pump wavelength.

In a single mode optical fibre, the wave-vector mismatch Δk is mainly determined by the material dispersion and nonlinear phase shift in the form [12]:

$$\Delta k = \Delta k_M + \Delta k_{NL}, \tag{2-40}$$

where Δk_M and Δk_{NL} represent the mismatch occurring as a result of material dispersion and nonlinear effects respectively.

Assuming that the pump is much more intense than the new frequency components generated and remains undepleted, the nonlinear phase shift due to SPM of the two degenerate pump photons can be written using Eq. (2-37) as [12]:

$$\Delta k_{NL} = 2\gamma P_0, \tag{2-41}$$

where P_0 is the input pump power.

The frequencies in the Eq. (2-23) of the θ_--type FWM can be written in terms of frequency shift Ω_s such that ($\omega_1 = \omega_2$ due to the degenerated pump photons):

$$\Omega_s = \omega_1 - \omega_3 = \omega_4 - \omega_1. \tag{2-42}$$

Then, using the Taylor series expansion similar to Eq. (2-28) up to the quadratic term, the Δk_M can be expressed in terms of the Ω_s as:

$$\Delta k_M \approx \beta_2 \Omega_s^2. \tag{2-43}$$

Substituting Eqs. (2-41) and (2-43) into Eq. (2-40), it can be seen that phase matching, i.e., $\Delta k = 0$, occurs only in the anomalous dispersion regime, i.e., $\beta_2 < 0$, at the frequency shift given by:

$$\Omega_s = \left(\frac{2\gamma P_0}{|\beta_2|}\right)^{1/2}. \tag{2-44}$$

Thus, a pump wave propagating in the anomalous dispersion regime would develop sidebands located at $\omega_1 \pm \Omega_s$ as a result of FWM that is phase matched by SPM as illustrated in Figure 2-10. Furthermore, it can be shown that the power gain spectrum due to the MI is given by [12]:

$$g(\Omega) = |\beta_2 \Omega| (2\Omega_s^2 - \Omega^2)^{\frac{1}{2}}. \qquad (2\text{-}45)$$

Using Eq. (2-45), the gain spectra for the SMF-28e fibre for three input powers are calculated at wavelength of 1550-nm and shown in Figure 2-11. The gain spectrum is symmetric with respect to Ω=0. As the input power is increased, the gain-peak shifts further away from the centre.

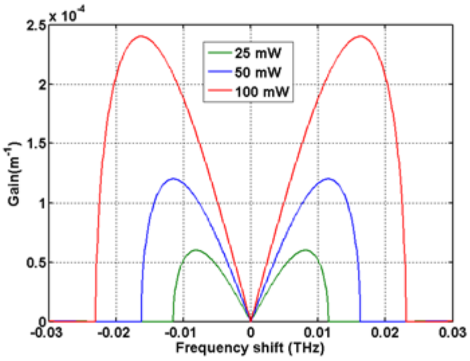

Figure 2-11 Gain spectra of MI at three power levels for SMF 28e (i.e., β_2=-23 ps^{2}km^{-1}, D=18 pskm^{-1}nm^{-1}, γ=1.2 W^{-1}km^{-1}).

Erbium doped fibre lasers operating at 1550 nm fall in the anomalous dispersive medium. In these fibre lasers, I have experimentally observed that MI is the first nonlinear effect that limits the maximum output peak power by transferring the energy to the two MI-induced sidebands as will be described in Section 3.3 and 5.4.2.

2.2.3.4 Stimulated Brillouin scattering

When an incident photon with frequency ω_L interacts with a thermal induced acoustic phonon, a small part of the incident photon can be backscattered with a frequency ω_S that is downshifted by ~10-20 GHz in silica fibre at ~1.55 μm pump wavelength [17]. The frequency downshifted backscattered light is known as Stokes light and this phenomenon is known as spontaneous Brillouin scattering. The beating of Stokes light and the incident light induces a forward travelling index modulation, i.e., a Bragg grating structure, via electrostriction effect. The frequency of this travelling grating Ω is given by the frequency difference between the incident pump light and Stokes light, i.e., $\Omega = \omega_L - \omega_S$, as illustrated in Figure 2-12. The presence of this grating can further increase the backscattered Stokes light. With even higher incident pump power, the grating can be further developed such that most of the incident light is transferred to the backscattered Stokes light and is known as stimulated Brillouin Scattering (SBS) [16, 18].

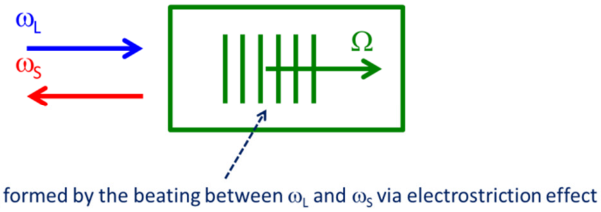

Figure 2-12 An illustration of stimulated Brillouin scattering.

SBS is a detrimental effect that potentially limits the peak power that can be extracted by the narrow-linewidth fibre laser described in **Error! Reference source not found.**. The SBS threshold (P_{SBS}) is defined as the critical input power where the backscattered light at the fibre input end becomes equal to the power at the fibre output end and is given by [12]:

$$P_{SBS} = \frac{21A_{eff}}{L_{eff}g_B}, \tag{2-46}$$

where g_B is Brillouin gain which has the peak value, $g_{B,peak}$, of ~$5 \times 10^{-11} m/W$ for silica fibre [12] and L_{eff} is the effective length. For the case of a passive fibre, the L_{eff} is defined as:

$$\mathrm{L_{eff}} = \frac{1 - e^{-\alpha_p L}}{\alpha_p}, \tag{2-47}$$

where α_p is the background loss of the pump in m^{-1} and L is the length of the fibre. On the other hand, for the case of gain (active) fibre, the effective length is defined as:

$$\mathrm{L_{eff}} = \frac{e^{gL} - 1}{g}, \tag{2-48}$$

where g is the saturated gain coefficient of the signal wavelength in m^{-1}. To account for the finite spectral width of the pump light, the Brillouin gain can be expressed as [18]:

$$g_B = \frac{g_{B,peak}}{(1 + \frac{w_{las}}{w_{BS}})}, \tag{2-49}$$

where w_{las} is the laser bandwidth and w_{BS} is the Brillouin gain bandwidth which is 50-100 MHz in silica fibre [17]. This equation shows that g_B can be reduced by an increase of w_{las}, which in turn increases the SBS threshold.

The linewidth of the seed laser (External cavity tuneable laser-Agilent 81640A) of the MOPA described in **Error! Reference source not found.** is specified as 100 kHz. If the output of this seed laser is directly amplified using a 3.5 m long gain fibre with 20 dB gain, the SBS threshold is calculated as 0.39 W based on Eq. (2-46) with the parameters w_{BS} of 75 MHz, $g_{B,peak}$, of ~$5 \times 10^{-11} m/W$ and MFD of 10.4 µm (i.e., same as that of the SMF-28 fibre). This shows that the SBS threshold is rather low and will limit the power available for further nonlinear frequency conversion. Therefore, in **Error! Reference source not found.**, the narrow linewidth seed laser was phase-dithered to increase its linewidth in order to mitigate the detrimental effects of SBS. Furthermore, the effect of SBS is also further suppressed by choosing a signal pulse width of ~0.5 ns that is much less than the acoustic phonon life time of ~10 ns [12].

2.2.3.5 Stimulated Raman scattering

The stimulated Raman scattering (SRS) is a stimulated emission process due to the interaction of incident photon and the optical phonon originates from the molecular vibration of the optical medium. In this process, when the frequency difference between the pump and the Stokes light matches the molecular vibrational frequency, the transfer of power from pump to Stokes light occurs with a transfer rate that depends on both pump and Stokes powers [12].

The SRS threshold (P_{SRS}) is defined as the critical input power where the Stokes light at the fibre output end becomes equal to the pump power at the fibre output end, and is given by [12]:

$$P_{SRS} = \frac{16A_{eff}}{L_{eff}g_R}, \tag{2-50}$$

where g_R is the Raman gain coefficient with a value of $\sim 1 \times 10^{-13} m/W$ at the pump wavelength of 1 µm. Meanwhile, for other pump wavelengths g_R can be obtained by using the inverse dependence of g_R on Raman pump wavelength. Similar to the case of SBS, the effective length for SRS can be expressed by Eqs. (2-47) and (2-48) for the passive and gain fibres respectively.

For an erbium doped fibre amplifier based on 5 m long LMA fibre (Liekki Er-60-40/140) described in Section 2.1.4 with 20 dB gain, the SRS threshold can be estimated as ~1.2 kW at 1.55 µm based on Eq. (2-50) with A_{eff} of 804 µm^2 and g_R of $0.66 \times 10^{-13} m/W$. However, the emission wavelength of the erbium doped silica fibre laser at 1.55 µm is located at the anomalous dispersion regime, where nonlinear wavelength conversion due to modulation instability (MI) is also possible. In this work, I have found that the threshold for modulation instability (MI) in erbium doped silica fibre is lower than the SRS and will be discussed in Section 3.3.

2.3 Erbium doped fibre amplifiers

This section introduces the erbium doped fibre amplifiers (EDFA) for high power generation. The subsections are organised in a "bottom-up" sequence, i.e., material properties (Section 2.3.1 and Section 2.3.2), component properties (Section 2.3.3), subsystem properties (Section 2.3.4, 2.3.5 and 2.3.6) and system properties (Section 2.3.7).

The emission and absorption of light by the rare earth ion are first described in Section 2.3.1. The different pump wavelength options to excite erbium ion to the higher energy level are described in Section 2.3.2. Section 2.3.3 describes the all-fibrised pump coupling technologies for coupling pump power from pump laser into the active fibre. It also explains the "brightness enhancement" process occurs in cladding pumping scheme. Section 2.3.4 describes the concept of overlap factor to parameterise the spatial dependent of the overlap between the doping profile and the optical mode. Section 2.3.5 presents a simple model that describes quasi-three level fibre amplifiers. Section 2.3.6 describes the amplified spontaneous emission. Finally, in Section 2.3.7, the concept of master oscillator power amplifier is described.

2.3.1 Emission and absorption of light

A photon may interact with the electron of a rare earth ion if its energy matches the difference between the two energy levels E_2 and E_1. On one hand, the photon may transfer its energy to the ion, which is raised to a higher energy level. On the other hand, the ion can also undergo a transition to a lower energy level and resulting in the emission of photon of energy equal to the difference between the energy levels, $E_1 - E_2$ [13].

The rate of spontaneous emission of an ion, W_{sp}, into any of the available optical mode from energy level E_2 to E_1 is given by

$$W_{sp} = \frac{1}{t_{sp}}, \qquad (2\text{-}51)$$

where t_{sp} known as the spontaneous emission life time between the two energy levels. Meanwhile, the rate of stimulated emission (if the ion is in the E_2-level) and absorption (if the ion is in the E_1-level), W_i, is given by

$$W_i = \phi\sigma(\nu), \qquad (2\text{-}52)$$

where $\phi = \frac{I}{h\nu}$ is the photon-flux density (photon/ unit area.sec) , I is the intensity of light, ν is the photon frequency and h is the Planck constant. The transition cross section, $\sigma(\nu)$, is the coefficient of proportionality between the rate of an induced transition and the photon flux density.

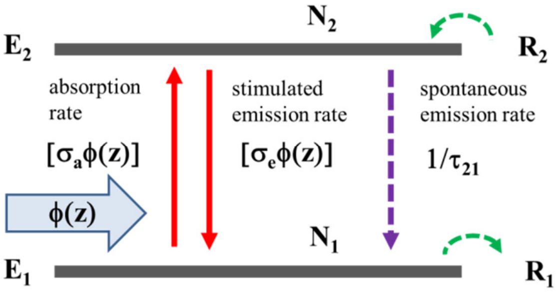

Figure 2-13 The population density N_2 and N_1 are determined by the rate of absorption, stimulated emission , spontaneous emission of photon as well as pumping and depumping rate of ion.

A monochromatic optical plane wave travelling in the z-direction with frequency ν and photon-flux density $\phi(z)$ will interact with a group of ions if the two relevant energy levels have an energy difference that nearly matches the photon energy $h\nu$ as illustrated in Figure 2-13. Let the number of ions per unit volume occupying energy levels E_2 and E_1, at time t, be $N_2(t)$ and $N_1(t)$ respectively. In the presence of energy degeneracy, the rate of change of $\phi(z)$ can be expressed as [13]:

$$\frac{\partial\phi(z)}{\partial z} = (N_2 - \frac{g_2}{g_1}N_1)\sigma(\nu)\phi(z),$$

$$\frac{\partial\phi(z)}{\partial z} = (N_2\sigma_e - N_1\sigma_a)\phi(z), \tag{2-53}$$

where g_2 and g_1 are the degeneracy factors. In the literature, the term $\sigma(\nu)$ can also be defined as the emission cross section, σ_e, and the term $\frac{g_1}{g_2}\sigma(\nu)$ is known as the absorption cross section, σ_a. The gain coefficient per unit length of the medium can then be expressed as

$$\gamma(z) = \sigma_e(\nu)N_2 - \sigma_a(\nu)N_1. \tag{2-54}$$

If $\gamma(z)$ is positive, the medium can act as an optical amplifier. If it is negative, the medium acts as an optical absorber. Specifically, if there is no ion occupies the energy level E_2 , i.e., $N_2 = 0$, Eq. (2-54) becomes

$$\gamma(z) = -N_1\sigma_a(\upsilon) = -\alpha(z), \tag{2-55}$$

$$\alpha(z) = N_1\sigma_a(\upsilon), \tag{2-56}$$

where $\alpha(z)$ is known as the absorption coefficient per unit length of the medium.

Through the stimulated emission and the absorption processes, the ions transit between the two energy levels and result in the change of $N_2(t)$ and $N_1(t)$. Furthermore, the population density can also change due to the presence of external pumping, which increases $N_2(t)$ at the rate of R_2 and decreases $N_1(t)$ at the rate of R_1 as illustrated in Figure 2-13. Hence, the rate equations that describe the rate of change of population densities $N_2(t)$ and $N_1(t)$ as a result of pumping, radiative and nonradiative transitions are given by [13]:

$$\frac{dN_2}{dt} = R_2 - \frac{N_2}{\tau_2} - N_2\sigma_e\phi(z) + N_1\sigma_a\phi(z), \qquad (2\text{-}57)$$

$$\frac{dN_1}{dt} = -R_1 - \frac{N_1}{\tau_1} + \frac{N_2}{\tau_{21}} + N_2\sigma_e\phi(z) - N_1\sigma_a\phi(z), \qquad (2\text{-}58)$$

where τ_2 and τ_1 are the overall life time of E_2 and E_1 respectively and τ_{21} is the life time for decay from level E_2 to E_1. When the non-radiative transition between E_2 to E_1 is negligible, $\tau_{21} \approx t_{sp}$.

2.3.2 Pump wavelengths for erbium ions

For the generation of ~1.55 μm radiation, the 3 most important manifolds for pumping the Er^{3+}-ions are the $^4I_{15/2}$ ground state manifold, the $^4I_{13/2}$ lasing manifold and the $^4I_{11/2}$ excited state manifold. Three kinds of pumping approaches to excite the Er^{3+}-ions into the $^4I_{13/2}$ lasing manifold are discussed below.

Traditonal 980 nm and EYDF pumping approach

For these two approaches, the Er^{3+}-ion is first excited to the short-lifetime $^4I_{11/2}$-level. The $^4I_{11/2}$-life time is ~5 μs in Al-Ge-silicate fibre [19]. This lifetime can be shortened to 0.1-5.0 μs by co-doping the silica fibre with phosphorous [20]. The Er^{3+}-ion nonradiatively decays from $^4I_{11/2}$ to the $^4I_{13/2}$ lasing manifold. The generation of ~1.55 μm radiation is achieved when the radiative decay take place between the $^4I_{13/2}$ lasing manifold and the $^4I_{15/2}$ ground state manifold.

In the traditional 980 nm pumping approach, the Er^{3+}-ion is directly excited from $^4I_{15/2}$ into the $^4I_{11/2}$-level by pumping with 980 nm pump as illustrated in Figure 1-2(a). An example of the σ_e and σ_a of Er^{3+}-doped Al-Ge-silicate fibre are shown in Figure 2-14, where the absorption peak at 980 nm is shown.

In EYDF approach, the Er^{3+}-ion is pumped to the $^4I_{11/2}$-level via the nonradiative, resonant energy transfer from Yb^{3+}-ion as illustrated in Figure 1-2(b). In this process, the pump photon is first absorbed by the Yb^{3+}-ion to move from $^2F_{7/2}$-level into the $^2F_{5/2}$-level. Due to the close proximity of the Er^{3+}-ion, the nonradiative, resonant energy transfer takes place between the excited Yb^{3+}-ion and the ground state $^4I_{15/2}$ of the Er^{3+}-ion exciting the Er^{3+}-ion to the $^4I_{11/2}$ level, while dropping the Yb^{3+}-ion back to the $^2F_{7/2}$ ground state [21]. An example of the σ_e and σ_a in an Er^{3+}/Yb^{3+}-codoped phosphosilicate fibre are shown in Figure 2-15. Since the absorption cross section of Yb^{3+}-ion (blue dashed line) is much higher and broader than Er^{3+}-ion (red dashed line) around 910-980 nm, a much higher population inversion of Er^{3+} can be built up at $^4I_{13/2}$ lasing manifold via EYDF approach compared to the traditional 980 nm approach.

In-band pumping/ tandem pumping/ resonant pumping

In the in-band pumping approach, the Er^{3+}-ions is directly excited from $^4I_{15/2}$ ground state manifold into the $^4I_{13/2}$-lasing manifold as illustrated in Figure 1-3. The population inversion is still possible due to the broad bandwidths of $^4I_{13/2}$- and $^4I_{15/2}$-manifolds. This kind of pumping scheme is known as in-band pumping, tandem pumping or resonant pumping in the literature since the Er^{3+}-ions are directly pumped to the lasing manifold. The main advantage of in-band pumping scheme is the potential low quantum defect (<2%) between the pump and the signal wavelengths.

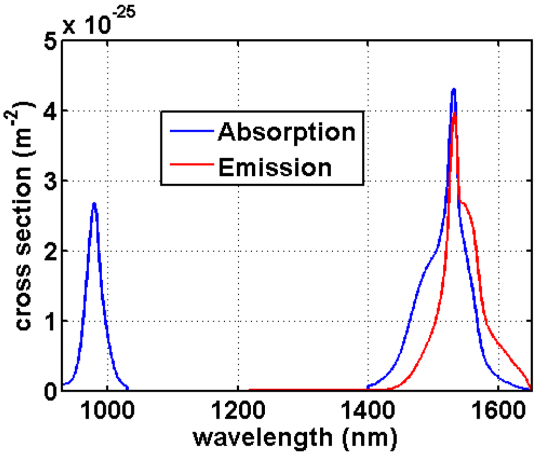

Figure 2-14 The absorption- and emission- cross sections of a typical Er^{3+}-doped Al-Ge-Silicate fibre. The cross section data is from [22].

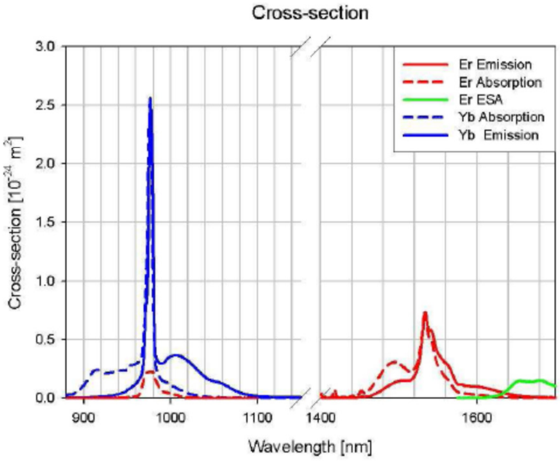

Figure 2-15 The absorption- (solid) and emission- (dotted) cross sections of a typical Er^{3+}/Yb^{3+} co-doped phosphosilicate fibre. The cross section data is from [23].

2.3.3 Pump coupling scheme for active fibres

In the active fibre devices, such as optical fibre amplifiers and fibre lasers, the pump power needs to be coupled into the active fibre for the excitation of the rare-earth ions. In this section, two fibrised pump coupling schemes are briefly described, namely core pumping scheme and cladding pumping scheme.

In the core pumping scheme, the single mode pump power and signal power are combined using a wavelength division multiplexer (WDM) into the core of the active fibre. Hence, the pump exhibits large overlap with the doped fibre core. The advantage of this scheme is that the pump light is guided in the core resulting in high pump intensity. Therefore, higher pump absorption and gain per unit length can be achieved for a given ion doping concentration. Conversely, for a given required pump absorption, a lower ion doping concentration can be used to avoid the parasitic ion-ion interaction (see Section 4.1.2). However, there are at most two pump input ports, i.e., the input and output ends in case of bidirectional pumping scheme, available to allow the pump power to couple into the active fibre. Furthermore, the pump power available from the single mode laser diode is much lower compared to the multimode laser diode. Hence, the core-pumped scheme is limited for power scaling due to the number of pump ports and pump power available.

The cladding pumping scheme can be implemented using two different technologies, namely double-clad fibre (DCF) and GTwave fibre a type of DCF. With the DCF, the pump power from the multimode laser diodes is coupled into the inner cladding of DCF via a multi-port tapered fibre bundle (TFB) [24]. A typical cross section of a DCF with an octagonal shape inner cladding is shown in Figure 1-1. The DCF consists of a rare earth dope core, an inner cladding and an outer cladding layer. The outer cladding typically is low-index polymer-coating but can also be glass. The signal light propagating in the rare-earth doped core is guided by the index difference between the core and the inner cladding. Meanwhile, the pump light propagating in the inner cladding is guided by the index difference between the inner cladding and the outer cladding. The NA of the core can be somewhere in between ~0.06-0.23, depending on the host materials and the detail refractive index profile. The inner cladding (typical NA of ~0.45) has non-circular shape (for example, octagonal shape as shown in Figure 1-1) to break the circular symmetry of the fibre. This serves to increase the pump absorption by preventing the multimode inner cladding from supporting skew pump modes that do not overlap with the signal core. Furthermore, since the pump absorption only occurs in the core area, where the pump and rare earth ions overlapped with each other, the cladding absorption of the pump light is lower than the core absorption. Typically, the cladding absorption is estimated to be lower than core absorption by a factor given by the area ratio of core and inner cladding [1].

GT-wave fibre is another implementation of cladding pumping scheme. In this case, the power from multimode pump is first coupled into a silica pump rod, which has a NA of ~0.45. This silica rod is then held in close optical contact with the signal fibre in a common low refractive index polymer outer cladding. As the pump light propagates along the GTwave-fibre, it couples continuously between pump and signal rods along the entire length through evanescent field interaction [25]. This leads to the absorption of pump light by the rare earth doped signal rod (illustrated in red in Figure 2-16), which exhibits a core NA of 0.06~0.23.

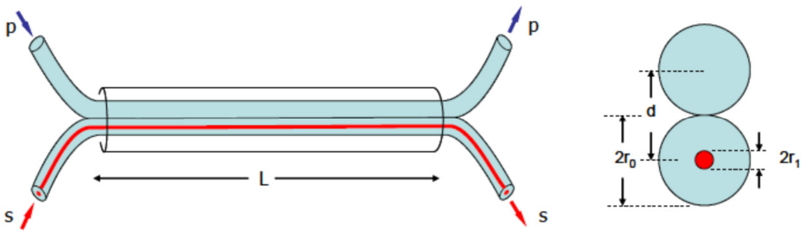

Figure 2-16 GTWave multimode fibre coupler schematic. s & p denote signal and pump rods, respectively [25].

In cladding pumping scheme, the multimode pump light propagates in the pump waveguide that has much larger cross sectional area and higher NA than the doped signal waveguide. As the multimode pump light is absorbed by the rare earth ions, the absorbed pump power is converted into the signal power through the process of stimulated emission and guides inside the core of the signal fibre. Hence, the beam quality of the output signal strongly depends on the modal property of the core. For example, if the signal fibre has a single mode core, the output signal will also be single moded.

To quantify the improvement of the quality of light as it converted from pump to signal power, it is useful to introduce a parameter known as brightness, B (unit: W/m^{2}sr), which is defined as [26]:

$$B = \frac{P}{A\Omega_{\mathrm{solid}}}, \tag{2-59}$$

where P is the optical power emitted from the light source, A is the area of the emitting surface and Ω_{solid} is the solid angle. The maximum solid angle of the output from a fibre is given as archsin(NA). Since the NA of signal is always less than the pump in cladding pumping scheme, the parameter Ω decreases in a cladding pumping scheme through the signal conversion process. Furthermore, the cross sectional area of signal is also smaller than pump in cladding pumping scheme. Hence, even though the signal power is unavoidably lower than the pump power, the brightness of the signal increases in cladding pumping scheme due to the reduction of both A and Ω_{solid}. This is known as the “brightness-enhancement” in the literature and is illustrated in Figure 2-17. In this illustration, the low beam quality pump light from laser diode at λ_p (the green colour beam at the right hand side) undergoes the brightness conversion process in the cladding pump fibre to generate the high beam quality signal light at λ_s (the red colour beam at the right hand side). Physically, the increase of B means that for the same average power, the signal light with a higher brightness can be focused to a smaller spot size and results in a higher intensity. This kind of property is useful in many laser applications.

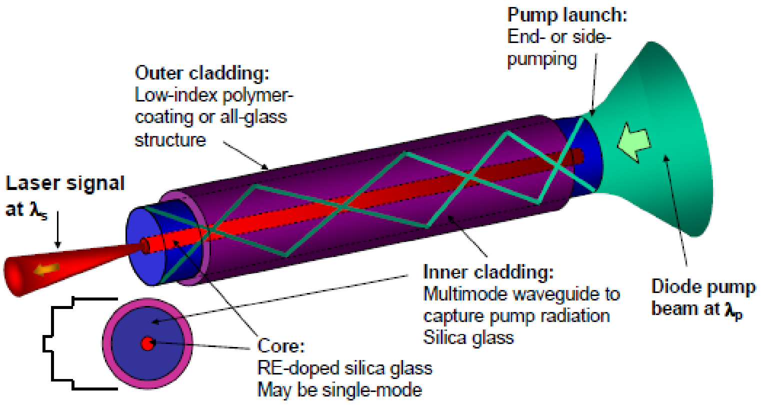

Figure 2-17 The brightness conversion in cladding pumped fibre [6].

The “brightness-enhancement” comes at a cost of having lower pump absorption per unit length compared to core pumping scheme for the same core design. Hence, to achieve the same absorbed pump power, a longer active fibre length or a higher ion doping concentration required in cladding pumping scheme. However, an increase in active fibre length increases the nonlinear length and an increase in ion concentration may induce detrimental ion-ion interactions. Therefore, cladding pumped fibre must be designed with care to achieve the brightness enhancement while minimising the detrimental effects.

2.3.4 Overlap factor

In deriving the rate equations and power propagation equations presented in Section 2.3.1, it is assumed that optical power and the doped ions exhibit spatial dependence only in the direction of the propagation of light. However, the amplification of the fibre modes in a fibre amplifier does exhibit transverse dependence due to the transverse intensity distribution of the fibre modes. Therefore, a fibre amplifier model with the transverse dependence should be implemented [27]. Nevertheless, if the doped fibre exhibits circular symmetry ion doping distribution and the optical powers are guided in the LP_{01} mode with mode field radius larger than the ion doping radius, the spatial dependence of the interaction between rare earth ions and optical modes can be parameterised by an overlap factor, Γ, given by [22] [28]:

$$\Gamma = 2\pi \int_0^{\infty} I^n(r) \frac{n(r)}{N} r dr, \qquad (2\text{-}60)$$

where r is the radial position, $n(r)$ is the actual ion doping profile, N average ion density and $I^n(r)$ is the normalised transverse mode intensity, such that $2\pi \int_0^{\infty} I^n(r) n(r) r \, dr = 1$.

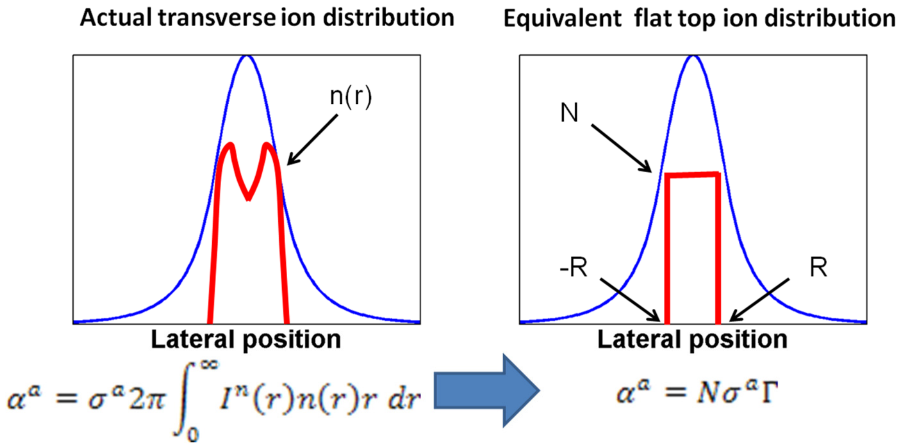

Figure 2-18 With the overlap factor, the circularly symmetric ion distribution profile is simplified into an equivalent flat-top ion distribution profile. The blue lines are the LP_{01} mode intensity profile and red lines are the ion distribution profile.

In this model, the actual transverse ion distribution is replaced with an equivalent "flat top ion distribution" as illustrated in Figure 2-18. The erbium distribution of this equivalent flat top structure is defined by two parameters, namely the equivalent ion density N and radius R given by

$$N = \frac{2\int_0^{\infty} n(r) r dr}{R^2}, \qquad (2\text{-}61)$$

and

$$R = \left(2\int_0^{\infty} \left(\frac{n(r)}{n(0)}\right) r dr\right)^{\frac{1}{2}}, \qquad (2\text{-}62)$$

respectively whereas the effective doping area is given by $A = \pi R^2$.

In addition, it is worth mentioning that if the overlap factor of the pump wavelength is known in the core pumping scheme, the overlap factor in a cladding pump scheme with the same rare earth doped core can be approximated by multiplying the core pumping scheme overlap factor with the area ratio of core and inner cladding [1].

2.3.5 Quasi-three level fibre amplifier model

In a quasi-three level fibre amplifier, the lasing transition involves only two energy manifolds. With the overlap factor and Eq. (2-53), the power propagation equations of quasi-three level fibre amplifiers for single pump and signal wavelength with the same propagation direction can be written as:

$$\frac{dP_p}{dz} = [N_2\,\sigma_e(\lambda_p) - N_1\,\sigma_a(\lambda_p)]\Gamma_p P_p, \tag{2-63}$$

$$\frac{dP_s}{dz} = [N_2\,\sigma_e(\lambda_s) - N_1\,\sigma_a(\lambda_s)]\Gamma_s P_s, \tag{2-64}$$

where P_p/P_s is the power at pump/signal wavelength with the corresponding overlap factor Γ_p/Γ_s. Similarly, the rate equation s of the upper and lower energy levels can be written as:

$$N = N_1 + N_2, \tag{2-65}$$

$$\begin{aligned}\frac{\partial N_2}{\partial t} = -\frac{N_2}{\tau} + \frac{\Gamma_p \lambda_p}{hcA}[\sigma_a(\lambda_p)N_1 - \sigma_e(\lambda_p)N_2]P_P \\ + \frac{\Gamma_s \lambda_s}{hcA}[\sigma_a(\lambda_s)N_1 - \sigma_e(\lambda_s)N_2]P_s,\end{aligned} \tag{2-66}$$

where A is the effective doping area. In the steady state, the condition $\frac{\partial N_2}{\partial t} = 0$ can be applied to Eq. (2-66) to determine the N_2 at each position. Despite the simplicity, Eqs. (2-63)-(2-66) is commonly used to model fibre amplifier behaviour.

An example of quasi-three level fibre amplifiers is the in-band pumped erbium doped fibre amplifiers, where the upper and lower energy levels are $^4I_{13/2}$ and $^4I_{15/2}$ respectively. More details of the quasi-three level nature of an in-band pumped erbium doped fibre amplifier will be discussed in Section 4.1.1. Furthermore, the traditional 980 nm pumped EDFA is often considered as quasi-three level fibre amplifiers due to the short life time (~5.2 μs) of $^4I_{11/2}$-manifold (see Section 4.1.2).

2.3.6 Amplified spontaneous emission

Besides stimulated emission, the population inversion also leads to spontaneous emission. The effect of spontaneous emission can significantly alter fibre amplifier behaviour especially in high population inversion condition through amplified spontaneous emission (ASE).

Generally, the spontaneous emission emits in all spatial direction but only those that are emitted into the guided modes can propagate in the fibre amplifier in both forward and backward directions. As the spontaneous emission starts to propagate along the fibre amplifier, it undergoes stimulated emission process and reduces the population inversion that could have otherwise contributed to the signal power. Therefore, the ASE is a parasitic effect that often limits the maximum achievable gain from a fibre amplifier.

A simple ASE model can be established by treating the ASE as a signal with a bandwidth corresponding to an effective bandwidth for the entire transition. The propagation equation expressing the ASE power propagating both in the forward and backward directions can then be written as [22]:

$$\frac{dP_{ASE}^{\pm}}{dz} = \mp\left(N_2\ \sigma_e(\lambda_{ASE}) - N_1\ \sigma_a(\lambda_{ASE})\right)\Gamma_{ASE}P_{ASE}^{\pm} \pm 2\sigma_e(\lambda_{ASE})N_2 h v_{ASE}\Delta v_{ASE}, \tag{2-67}$$

where $P_{ASE}^{\pm}$ is the ASE power, v_{ASE} and Δv_{ASE} is the central frequency and the bandwidth of the effective ASE. With such consideration, two additional terms must be added to the left hand side of Eq. (2-66) to account for the interaction of the forward and backward ASE powers with rare earth ions. In a more rigorous model, the ASE can be divided into many small frequency segments with equivalent bandwidth much smaller than the transition bandwidth [22].

The set of coupled differential equations, i.e., the propagation and the rate equations, that describes the fibre amplifier is a boundary value problem. In continuous wave operation, i.e., the steady state condition $\frac{\partial N_2}{\partial t} = 0$, it can be solved by numerical integration along the active fibre using relaxation method [29]. Since this is an important problem in the design of fibre amplifier, its numerical solution has been implemented in many commercial simulation softwares. In this work, I have simulated the fibre amplifier in continuous wave operation using the software known as Optisystem developed by Optiwave.

To illustrate the detrimental effects of ASE in the EDFA, I have simulated the behaviour of 980 nm pumped EDFA with and without ASE consideration. The main simulation parameters are as follow: total ion concentration=1×10^{25}m^{-3}, Er^{3+} life time=10 ms, core radius=2.2 µm, Er doping radius=2.2 µm, active fibre length=7 m, signal wavelength=1550 nm, input signal power=-20 dBm, input pump power=250 mW. When the ASE is considered, the ASE is considered to develop at ±50 nm around 1550 nm.

The simulated results are shown in Figure 2-19. The subfigure (a) shows the pump power distribution along the fibre position. Without the ASE, the pump power is used only for the amplification of the signal. Therefore, the pump power is slowly absorbed in the first 2 m of the fibre amplifier where the signal power is low. In contrast, in the presence of ASE, the pump power rapidly decreases in the first 2 m of the fibre amplifier. This can be understood using Figure 2-19(b) where the backward ASE reaches 70 mW at the input of the fibre amplifier. Hence, the rapid decrease of pump power is mainly caused by the conversion of pump power into the backward ASE power. The ASE also develops in the forward direction and reaches an average power of ~14 mW at the fibre output. Meanwhile, the ASE also changes the normalised inversion profile, especially at the fibre input end as shown in Figure 2-19(c). In the presence of ASE, the inversion reaches the maximum at ~2 m away from the input rather than at the input end where the pump power is the highest. This low inversion at the input end is again due to the strong ASE. Finally, due to the extraction of the inversion by ASE, the gain in the presence of ASE is less than those without the ASE as shown in Figure 2-19(d).

Hence, the ASE limits the maximum achievable gain as well as the maximum inversion from a fibre amplifier.

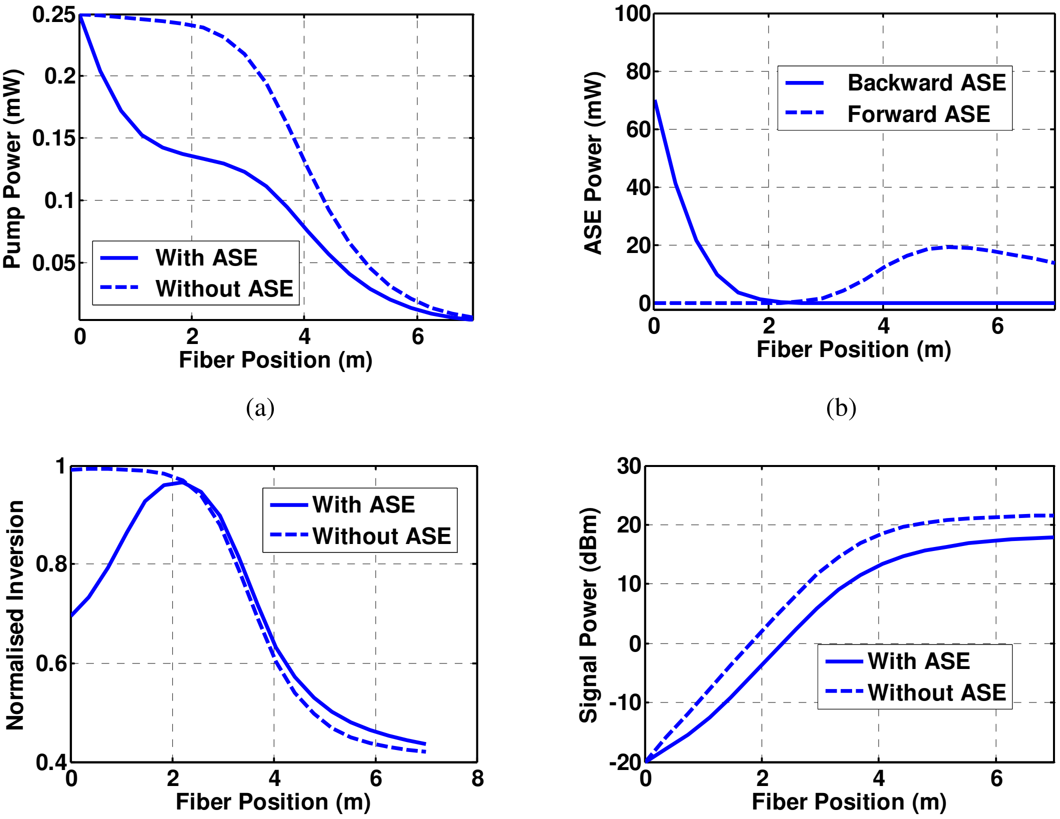

(a) (b)

(c) (d)

Figure 2-19 The simulated behaviour of 980 nm pumped EDFA along the fibre position with and without ASE consideration. (a) The pump power (b) The backward and forward ASE power (c) The populatin inversion (d) The signal power.

2.3.7 Master oscillator power amplifier

In the area of high power fibre laser, the master oscillator power amplifier (MOPA) architecture is often implemented to achieve high average power. In this section, the concept of the MOPA will be discussed from the system perspective.

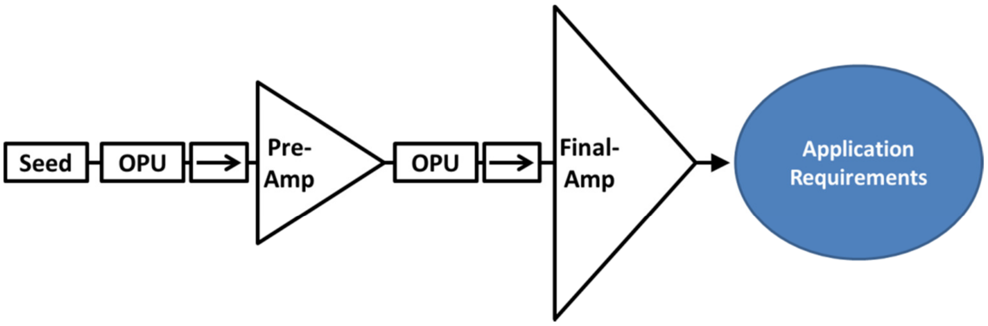

Figure 2-20 Schematic of a master oscillator power amplifier designed for a targeted application requirement. Seed: seed laser, pre-amp: preamplifier and final-amp: final stage amplifiers. The rectangular symbol with an arrow represents an optical isolator that prevents the backward amplified spontaneous emission (ASE) from

the next stage to influence the current stage. The optical processing unit (OPU) is a component used to tailor the characteristic of the signal light, for example, the spectral property can be tailored using fibrised filter and temporal characteristic can be tailored with electro-optic modulator.

A schematic of MOPA designed for a targeted application is shown in Figure 2-20. The MOPA can be divided into 3 stages namely seed, preamplifier (pre-amp) and final stage amplifier (final amp). In some cases it may be useful to insert optical processing unit (OPU) in between the stages to better serve the application requirements.

The seed, which is the master oscillator, can either be a semiconductor diode laser or solid state laser or fibre laser. It is desirable for the seed to have a fibre coupled output for ease of integration. The seed is typically chosen such that it exhibits the temporal and spectral characteristics similar to that required at the output of the MOPA. Typically, the power requirement is of secondary concern in choosing the seed as long as the seed output can be amplified without much degradation of the spectral and temporal characteristics. However, a low seed power leads to an increase number of preamplifier stages, which adds to the system complexity. It may be possible to add more fibrised components after the seed to further tailor the spectral and temporal characteristics. For example, a fibrised spectral filter can be used to remove the unwanted spectral components and electro-optic modulator can be used to create pulse from a continuous wave seed laser.

The output of the seed is first amplified by a preamplifier. The aim of the preamplifier is to increase the average power of signal such that it is sufficient to use as input to the final stage amplifier to reach the targeted output power. The management of ASE is an important issue in MOPA construction. Firstly, any high reflection point must be eliminated in the amplifier chain because the high reflection point can act as a “ASE-seed” [22]. A typical source of high reflection points in a fibre amplifier is the flat cleaved fibre end facet, which has a reflectivity of ~4%. This can be mitigated by having an angled cleaved fibre end facet or endcap [30]. Secondly, the preamplifier is often operated below the maximum achievable gain (for example, ~1-5 dB lower) even though this results in additional pre-amplifier stages along the MOPA chain. In this way, the ASE content in the output of each stage can be kept low, and is known as “gain staging” in literature. Even so, more ASE management strategy is still needed. The backward ASE (i.e., opposite to the input signal propagation direction) can alter the characteristic of previous stage. For example, if the previous stage is a seed laser, the backward ASE can potentially degrade, or sometimes even cause the catastrophic failure of the seed laser. Therefore, optical isolators must be used to reduce the backward ASE as shown in Figure 2-20. On the other hand, the forward ASE into the next amplifier stage can compete with the signal for the available population inversion. Hence, spectral filter is often added to remove ASE that is spectrally separated from the signal wavelength. In the case of pulse operation, the ASE can be removed by time gating the signal using either an acousto-optic modulator or an electro-optic modulator, i.e., switch the modulator into the high transmission state only when the signal pulse is present in the time domain. Alternatively, the pump power of the amplifier can also be modulated such that the inversion builds up only when amplification of signal pulse is required.

The final amplifier is the most crucial and complicated part, sometimes also the most dangerous part, of a high power MOPA system. It typically consists of a strongly pumped large mode area fibre to amplify the input signal to the desired output power. High average power at the final stage means that the thermal issues need to be managed. The typical hot spots are near the pump coupling point, splice point (if any) and bend section of the fibre. The heat from these sources must be dissipated to prevent a fire that often initiates from any flammable materials near the heat source or even the fibre coating itself. As an example, Figure 2-21 shows the aftermath of fire that happened during one of my experiment due to the improper management of the heat source due to bend section of the fibre.

Furthermore, the heat that builds along the length of the fibre amplifier from the incomplete conversion of the absorbed pump power to signal power can also lead to the temperature build up and can damage the fibre coating. Therefore, the temperature of the fibre should not be allowed to exceed 80 ^{O}C for long term reliability [6].

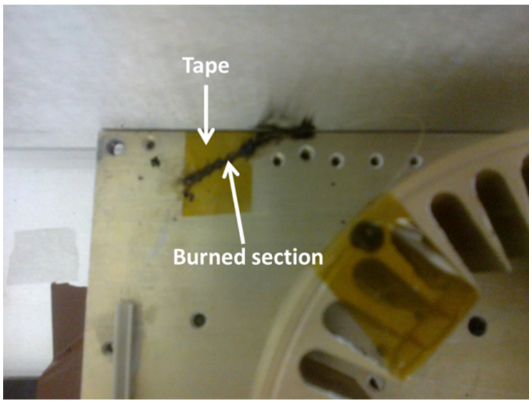

Figure 2-21 The aftermath of the fire that happened at a bent section of a cladding guided pump fibre. Due to the bending, the multimode pump power leaked out from the fibre and became a heat source, which eventually lead to the fire that initiate from the high temperature resistant kapton tape.

In a pulsed MOPA, the high average power often results in high peak power and/or high pulse energy. Therefore, the intensity at the output end facet can exceed the damage threshold of the glass (the glass-air damage threshold is 1×10^9 W/cm^2 in CW regime and the bulk damage threshold is 40 J/cm^2 @1ns in the pulse regime) [30]. Therefore, "end cap" must be applied to expand the output beam size at the glass-air interface to reduce the power and energy density. The associated high peak power may also initiate nonlinear processes (see Section 2.2) that can degrade the spectral characteristic of the MOPA output. Meanwhile, a pulse energy comparable to the saturation energy of the fibre leads to the gain saturation that distorted the input pulse shape (see Section 5.1.1). Moreover, much of the ASE consideration for preamplifier is still applicable in final stage amplifier. Finally, the build up of population inversion in the fibre amplifiers, in particular the final amplifier, must be extracted in a controlled and consistent manner. If this controlled energy extraction is accidentally stopped, the excessive gain can lead to catastrophic failure that can potentially destroy much of the MOPA setup [5, 30].

The discussion above shows that the implementation of MOPA can lead to many stages and each stage consists of multiple components to tailor the characteristics of the signal such that a desired output signal characteristics can be obtained at the output of the amplifier chain. Hence, the MOPA is rather complex compared to a laser oscillator. However, the MOPA architecture offers a systematic approach to increase the average output power of high quality seed laser while maintaining a high degree of control on other seed characteristics. Therefore, the MOPA is currently the most desirable architecture in the area of high power fibre lasers. Yet, due to the complex nature of the MOPA, the implementation of MOPA is a highly experiment oriented discipline that involves careful characterisation of laser performance at all foreseeable operating conditions after each amplifier, if not each component, is added to the MOPA chain.

Chapter 3 Q-switched fibre lasers

In this chapter, I describe my investigation to realise a Q-switched fibre laser suitable as a seed laser for the high energy in-band pumped pulsed MOPA in Chapter 5. The Q-switched fibre laser is chosen as it can generate relatively high pulse energy and, therefore, reduce the number of stages as well as system complexity of the high energy MOPA.

Q-switching is a widely used technique to create nanosecond high energy pulses. In the Q-switched process, through removal of the feedback mechanism, the laser medium builds up to a much higher population inversion than usual inside the laser cavity. When the cavity feedback is suddenly restored, the high level of population inversion, which has been previously built up, results in a short but intense burst of laser output [31].

Q-switched fibre lasers represent an attractive source of high-energy, nanosecond pulses. A typical Q-switched fibre laser consists of a length of active fibre, a pump coupler, cavity mirrors and a bulk-optic Q-switch – usually an acousto-optic modulator (AOM) [13]. However, since these components are typically free-space coupled to each other such lasers are relatively sensitive to environmental perturbations and this can compromise their practical applications. In comparison, an all-fibrised Q-switched laser, where all components are fusion-spliced together, is more robust and environmentally stable. However, the cavity round trip time (τ_{RT}) of such lasers is often relatively long due to the component fibre pigtails. This tends to result in longer pulses and can also give rise to what is referred to as the Multiple Peak Phenomena (MPP) in which the Q-switched pulse develops sub-structure and can even break up into multiple sub-pulses [32, 33]. This is clearly highly undesirable for many applications.

In addition, a long cavity length in combination with the high peak powers generated can give rise to significant nonlinear spectral distortions [34, 35]. These effects often occur concurrently and certain authors e.g., Upadhyaya et el. have performed experimental studies where they suggest that the MPP originates from nonlinear Stimulated Raman Scattering/Stimulated Brillouin Scattering (SRS/SBS) [35]. Wang et al. have also studied the effect of SRS and SBS on the performance of Yb-doped Q-switched lasers [34]. However, since there was no ready way of switching between smooth and unstructured pulses in these experiments, it was difficult to decouple the effect of MPP and nonlinearity making the results very difficult to interpret.

This chapter presents the experiment and simulation I undertook to realise an all-fibre erbium doped Q-switched laser with no MPP as well as my investigation into the interplay between MPP and nonlinear effects. First, the pulse shape of the traditional Q-switched model is briefly described in Section 3.1. Next, the MPP in a core-pumped Q-switched fibre lasers is investigated in Section 3.2. Finally, Section 3.3 investigates the MPP and nonlinear effects in a cladding-pumped Q-switched fibre laser.

3.1 Point model of Q-switched laser

In Q-switching, the laser cavity loss is modulated between a high value (OFF-state) and a low value (ON-state) to create a laser pulse. During the OFF-state, the build-up of laser radiation is prevented by the high loss. As a result, energy is stored in the laser gain medium during this period. When the loss is decreased suddenly, the laser medium has a very high gain, which can build up the laser radiation rapidly and creates a burst of energy. Once the gain is depleted below the cavity loss, the laser intensity starts to decrease (with a time constant in the order of the photon cavity life time, τ_p) [13].

The evolution of the photon density and the population inversion during the Q-switched process can be described by the following coupled rate equation [13]:

$$\frac{dn}{dt} = -\frac{n}{\tau_p} + \frac{N}{N_t}\frac{n}{\tau_p}, \tag{3-1}$$

$$\frac{dN}{dt} = -2\frac{N}{N_t}\frac{n}{\tau_p}, \tag{3-2}$$

where n is the photon number density, N is the population inversion and N_t is the threshold population difference. The N_t is given by $N_t = \frac{\alpha_r}{\sigma_e}$ and determines the minimum pumping rate for the initiation of the laser oscillation. τ_p is the photon life in the cavity and is defined as $\tau_p = \frac{1}{c\alpha_r}$, where α_r is the cavity loss per unit length. α_r is defined by $\alpha_r = \alpha_s + \frac{1}{2d} ln \frac{1}{R_1 R_2}$ for a linear laser cavity, where α_s is the absorption coefficient of the medium, d is the cavity length, $R_1(R_2)$ is the reflectivity of the first (second) mirror and σ_e is the emission cross section. The equations above are valid if the laser intensity can be assumed to be uniform along the laser cavity. The optical pulse characteristics can be obtained by numerically integrating the coupled differential equation above. Some examples of typical pulse shapes obtained are shown in Figure 3-1.

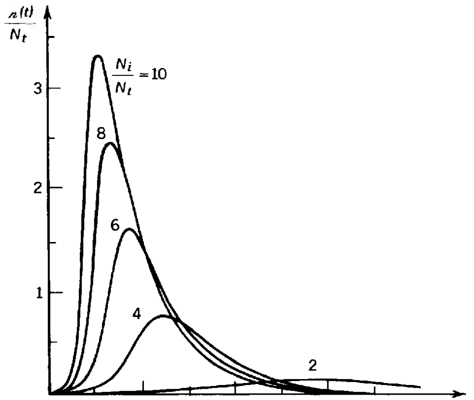

Figure 3-1 Typical Q-switched pulse shapes obtained from numerical integration of the rate equation of the point model at various initial population inversion (N_i). The photon-number density *n(t)* is normalised to the threshold population difference N_t and the time is normalised to the photon cavity lifetime τ_p [13].

3.2 The multiple-peak phenomena in core-pumped Q-switched fibre laser

In this section, the MPP in a core-pumped Q-switched fibre laser is investigated through experiment and simulation. Section 3.2.1 describes the experiment that demonstrates the elimination of MPP. Section 3.2.2 describes the simulation of the dynamics of Q-switched fibre laser based on the travelling wave model.

3.2.1 Experiment

3.2.1.1 Experimental setup

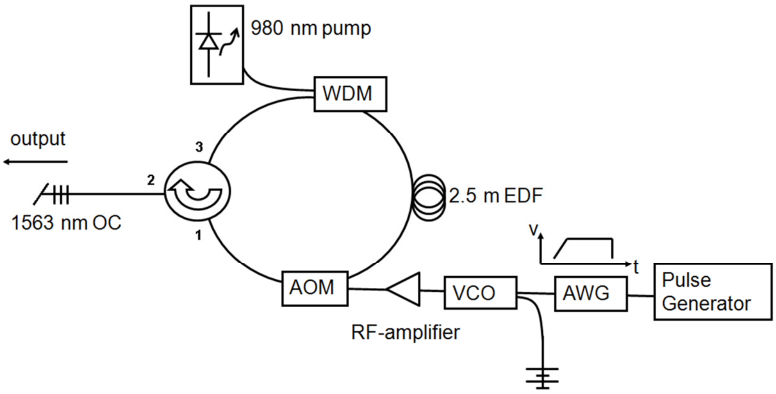

Figure 3-2 Experimental setup for the Q-switched all-fibre ring laser with an estimated cavity length of~6.4 m. The port 1, port 2 and port 3 of the circulator are labelled.

The setup consists of a ring laser cavity as shown in Figure 3-2. Unidirectional operation is ensured by a circulator with an isolation of ~54 dB between port 1 to port 2. A low reflectivity (~5%) fibre Bragg grating (FBG) with full-width-half-maximum (FWHM) of ~1.15 nm is spliced to port 2 of the circulator and serves as the laser output coupler. The output end of the output fibre is angled-cleaved to suppress Fresnel reflections back into the cavity. Port 3 of the circulator is spliced to a 980/1550 nm wavelength division multiplexer (WDM). The pump diode is a grating stabilised 980 nm diode laser with a maximum output power of ~170 mW. Through the WDM, the signal and pump lights are coupled into a 2.5 m Er^{3+}-doped fibre (EDF), which is the laser gain medium. The EDF has absorption of ~37.5 dB/m at 1530 nm wavelength. The total cavity was estimated to be around ~6.4 m.

The AOM is controlled by a chain of RF-amplifier, DC-power supply, voltage controlled oscillator (VCO), arbitrary waveform generator (AWG, Tektronix AWG 2021) and pulse generator (Stanford DG 535). The repetition rate is fixed at 5 kHz. The AWG sends a trapezoidal electrical control pulse to the AOM. The rise time of the AWG can be programmed to a resolution of 6 ns. By changing the ramp rate of the trapezoidal electrical pulse, the optical rise time of the AOM, τ_r, can be varied from a minimum of 70 ns and the maximum output voltage is 5 V. To achieve a shorter τ_r, the pulse generator (Stanford DG 535) is used to drive the AOM directly. In this way, a τ_r of 35 ns can be produced with a maximum output voltage of 4 V as limited by the pulse generator. The duration of the electrical pulse from the AWG is chosen to be 4 μs for all operating conditions and a longer electrical pulse does not change the Q-switched pulse characteristics. The temporal axes for all the pulse plots begin (i.e., time =0) when the AOM starts to open. The AOM was measured to have an insertion loss of 7.87 dB (including a RF insertion loss of 4 dB) and an extinction ratio of 38.77 dB.

3.2.1.2 Switching response of AOM

As it will be shown in Section 3.2.2, the rise time of the AOM is an important parameter that affects the Q-switched pulse shape. The rise of the AOM is determined by fitting the experimental optical switching response of the AOM to the following function [33]:

$$T(t) = \left\{ \begin{array}{cc} T_{off} & t < t_0 \\ \frac{1}{2}\left\{1 + sin\frac{\pi(t - t_0 - 0.5\tau_r)}{\tau_r}\right\}T_{on}\,, & t_0 < t < t_0 + \tau_r \\ & T_{on} t_0 + \tau_r < t \end{array} \right\}, \qquad (3\text{-}3)$$

where $T(t)$ is the power transmission function, T_{on} is power transmission of the AOM in the ON-state and it is related to the insertion loss of the AOM, T_{off} is power transmission of the AOM in the OFF-state and it is related to the insertion loss and the extinction ratio of the AOM, t_0 is the time the AOM starts to open and τ_r is the rise time of the AOM. Next, the experimentally measured AOM response is fitted with Eq. (3-3) to determine the corresponding AOM rise time. An example of such fitting is shown in Figure 3-3. In this example, the measured AOM response function corresponds to the AWG electrical rise time of 24 ns. Through fitting, τ_r is determined to be 70 ns. This fitting function will be used in Section 3.2.2 to simulate the properties of the Q-switched ring laser.

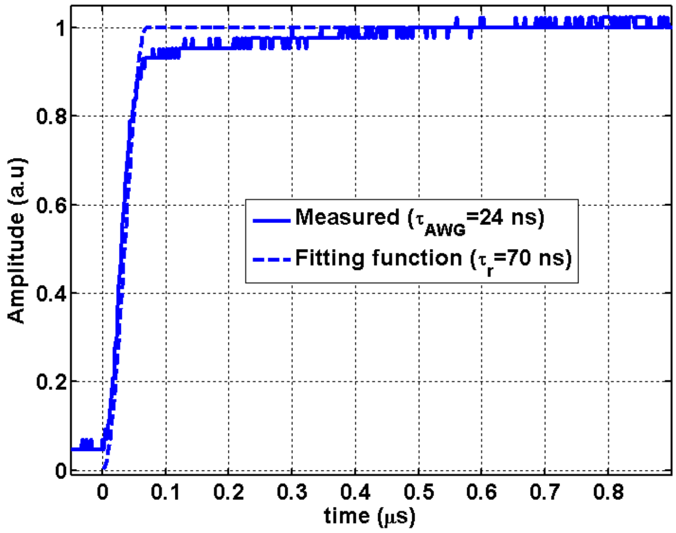

Figure 3-3 The measured AOM switching response (solid line) with AWG rise time (τ_{AWG}) of 24 ns and the corresponding fitting function (dashed line) using Eq. (3-3) with rise time (τ_r) of 70 ns.

3.2.1.3 *Experimental Result*

The effect of AOM rise time, τ_r, is investigated by changing the electrical pulse that is used to drive the AOM. When the AOM is driven directly with the Stanford pulse generator (without the AWG), the τ_r is measured to be 35 ns. However, when the AWG is used to drive the AOM, a rise time of more than 70 ns can be generated. Figure 3-4 shows the pulse shape generated by operating the AOM at three different rise times at 5 kHz repetition rate. The pulse shape generated with 35 ns rise time is different from those expected from the point model as shown in Figure 3-1. The modulated output pulse shape is caused by the MPP, which will be further discussed in Section 3.2.2. When τ_r is 70 ns, the pulse looks more similar to those predicted by the point model but with a slightly modulated top. When τ_r is 150 ns, the modulation is no longer visible. Therefore, the MPP can be eliminated by increasing the AOM rise time.

The average output power measured are 13.50 mW, 16.75 mW and 16.75 mW for rise time of 35 ns, 70 ns and 150 ns respectively. The lower measured average power for the case of 35 ns rise time might be attributed to the fact that the AOM cannot be fully switched ON by using the 4 V output from the Stanford pulse generator because 5 V is needed to fully switch on the AOM. Figure 3-5 shows the typical spectrum from the Q-switched laser. The ASE level is low due to the judicious positioning of AOM and circulator such that the unwanted ASE is not coupled to the output FBG during the OFF-state. Thus, by using an AOM rise time of 150 ns, a Q-switched all-fibre ring laser with no MPP is realised at 5 kHz repetition rate with an average output power of 16.75 mW and a pulse width of ~100 ns.

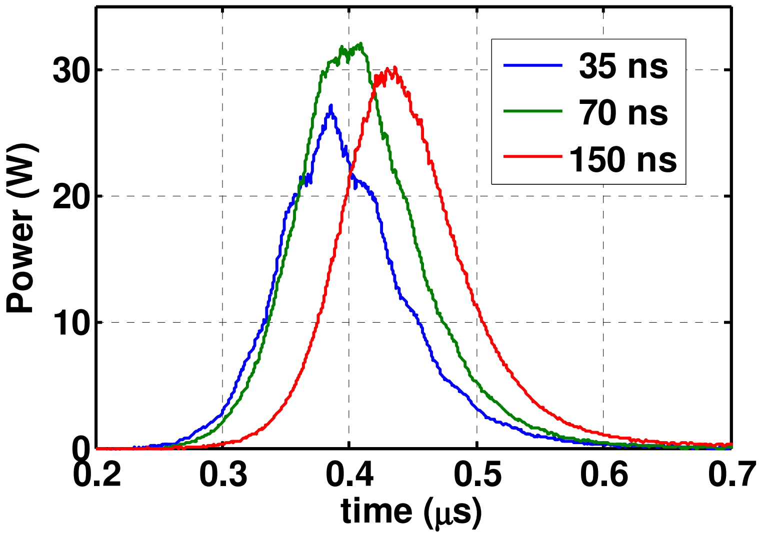

Figure 3-4 The temporal characteristic of pulsed produce with 3 different AOM rise times measured with Thorlabs D400FC InGaAs detector at 5 kHz repetition rate with AOM opening time of 1 μs. The average powers measured are 13.50 mW, 16.75 mW and 16.75 mW for rise time of 35 ns, 70 ns and 150 ns respectively. The pulse widths are ~100 ns for all cases.

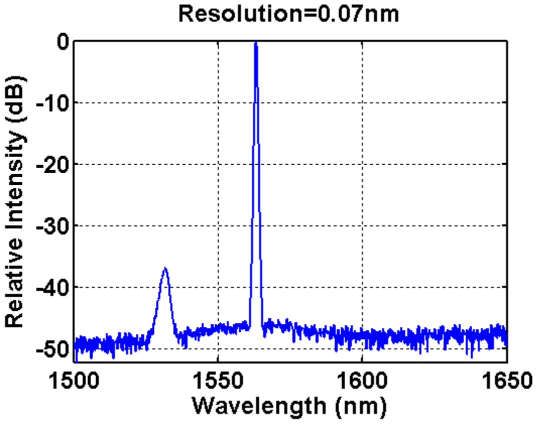

Figure 3-5 A typical spectrum of the Q-switched all-fibre ring laser measured with HP 86140A optical spectrum analyser with 0.07 nm resolution. The FWHM of the spectrum is determined as 0.22 nm.

3.2.2 Simulation

A typical fibre laser has a relatively long laser gain medium compared to a traditional solid state laser. Therefore, instead of the point model described in Section 3.1, the travelling wave model (TWM) of the fibre laser is needed to take into account the longitudinal variation of population inversion and photon density along the fibre laser [36].

3.2.2.1 Travelling wave model for the Q-switched ring laser

In an EDF gain medium that is pumped by 980 nm pump, it is usually sufficient to consider the ion in ground state ($^4I_{15/2}$) population, N_1, and upper-energy level ($^4I_{13/2}$) population, N_2, because the intermediate energy ($^4I_{11/2}$) has a short life time (~5.2 μs) compared to the upper-energy level, which has a life time of ~ 10-12 ms. With the assumption that the dopant concentration is uniform across the EDF, the simplified laser rate equation can be derived from Eqs. (2-57), (2-58) and (5-2) and expressed as below [34]:

$$N = N_1 + N_2, \tag{3-4}$$

$$\begin{aligned}\frac{\partial N_2}{\partial t} + \frac{N_2}{\tau} = \frac{\Gamma_p \lambda_p}{hcA}\left[\sigma_a(\lambda_p)N_1 - \sigma_e(\lambda_p)N_2\right](P_p^+ + P_p^-) \\ + \frac{\Gamma_s \lambda_s}{hcA}[\sigma_a(\lambda_s)N_1 - \sigma_e(\lambda_s)N_2](P_s^+ + P_s^-),\end{aligned} \tag{3-5}$$

$$\pm\frac{\partial P_p^\pm}{\partial z} + \frac{1}{v_p}\frac{\partial P_p^\pm}{\partial t} = \Gamma_p\left[\sigma_e(\lambda_p)N_2 - \sigma_a(\lambda_p)N_1\right]P_p^\pm - \alpha_p(\lambda_p)P_p^\pm, \tag{3-6}$$

$$\pm\frac{\partial P_s^{\pm}}{\partial z}+\frac{1}{v_s}\frac{\partial P_s^{\pm}}{\partial t}=\Gamma_s[\sigma_e(\lambda_s)N_2-\sigma_a(\lambda_s)N_1]P_s^{\pm}-\alpha_s(\lambda_s)P_s^{\pm}$$
$$+2\sigma_e(\lambda_s)N_2\frac{hc^2}{\lambda_s^3}\Delta\lambda_s, \qquad (3\text{-}7)$$

where N is the total dopant concentration, N_1 and N_2, which are both position(z) and time(t) dependent, are the ground- and upper-level population densities, $P_p^{\pm}$ and $P_s^{\pm}$ are the pump and the amplified spontaneous emission (ASE) powers at wavelength λ_p and λ_s respectively. The ± sign corresponds to the forward/backward propagation direction, and v_p and v_s are the group velocities of the pump and the ASE in the fibre respectively. For simplicity, only the ASE lies in the reflection band of the FBG is considered for the build-up of the laser emission. τ is the upper-level lifetime. A is the doped area of the fibre, Γ_p (Γ_s) is the overlapping factor between the pump (the ASE) and the fibre doped area, $\alpha(\lambda)$ is the fibre attenuation coefficient. $\sigma_e(\lambda)$ and $\sigma_a(\lambda)$ are the emission and the absorption cross sections of the doped fibre. $\Delta\lambda_s=\frac{\Delta\nu_s\lambda_s^2}{c}$ and $\Delta\nu_s$ is the bandwidth of the spontaneous emission. h is the Planck's constant and c is the speed of light in vacuum. The coupled partial differential equations above must be solved simultaneously with the appropriate boundary conditions, which depend on the cavity structure and the ON-OFF behaviour of the Q-switching process.

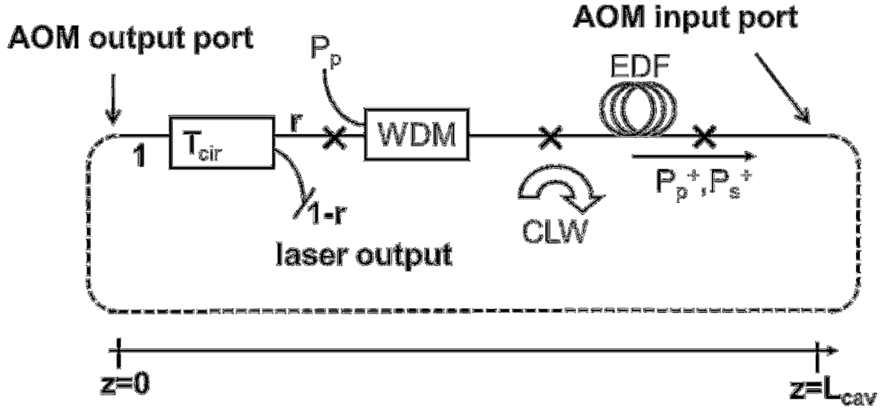

Figure 3-6 Model of the Q-switched fibre ring laser shown in Figure 3-2. CLW: the clock-wise direction.

In an all-fibre Q-switched laser, the passive fibre length comprised of a significant part of the laser cavity length. For example, the passive fibre make up of more than half of the total cavity length in the setup shown in Figure 3-2. Therefore, the effect of the passive fibre must be considered. A simplified model of the laser configuration is shown in Figure 3-6.

The spatial coordinate is chosen to start at the output port of the fibrised AOM (*z=0*) and end at the input port of the AOM (*z=L*). The corresponding boundary conditions for the all-fibre ring laser can be written as:

- For the pump power at the pump coupling point, i.e., the WDM:

$$P_p(z_{WDM},t)=\eta_p P_{p\_LD}, \qquad (3\text{-}8)$$

where η_p is the coupling efficiency of the WDM, P_{p_LD} is the power of the 980 nm pump diode.

- For the pump power at the beginning $P_p(0,t)$ and at the end $P_p(L,t)$ of the spatial coordinate:

$$P_p(0,t) = T_p P_p(L,t), \tag{3-9}$$

  where T_p is the transmission of the pump power across the AOM and is assume to be zero, i.e., no pump light will couple through the AOM.

- For the signal power at port 1 of the circulator $P_s^+(z_{port\,1},t)$and the reflected wave from the output FBG at port 3 of the circulator $P_s^+(z_{port\,3},t)$:

$$P_s^+(z_{port\,3},t) = \eta_c r P_s^+(z_{port\,1},t), \tag{3-10}$$

  where η_c is related to the insertion loss of the circulator and r is related to the reflectivity of the output FBG.

- For the signal power at the beginning $P_s^+(0,t)$ and at the end $P_s^+(L,t)$ of the spatial coordinate:

$$P_s^+(0,t) = P_s^+(L,t)T(t), \tag{3-11}$$

  where $T(t)$ is the optical switching response of AOM as defined in Eq. (3-3).

In the simulation model, the effect of backward-travelling wave (the isolation of the circulator is ~54 dB) and the effect of out-of-band ASE are neglected. The laser dynamic reaches the steady state after about tenth Q-switched pulse [34] and, hence, the fifteenth Q-switched pulse is shown in Figure 3-8(a) as the steady-state pulse profile.

3.2.2.2 Finite difference method

One of the common numerical methods to solve coupled partial differential equations is the finite difference method. In this section, the implementation of finite difference method to solve the travelling wave equations, i.e., Eqs. (3-4) to (3-7), is briefly discussed.

The travelling wave equation is similar to the prototypical general flux-conservative equation as shown in Eq. (3-12), which describes the transportation of *u* by a "fluid flow" with a velocity [37].

$$\frac{\partial u}{\partial t} = -v\frac{\partial u}{\partial x}. \tag{3-12}$$

To implement the finite difference method, the equation is first discretised at equally spaced points along both *t*- and *x*-axes, such that:

$$x_{i+1} = x_i + j\Delta x, \;\; j = 0, 1, \dots, J \;, \tag{3-13}$$

$$t_{i+1} = t_i + n\Delta t, \;\; n = 0, 1, \dots, N \;, \tag{3-14}$$

where x_i denotes the discretised spatial position with index i, Δx is the spatial step size, J is the total number of spatial points, t_i denotes the discretised temporal position with index i, Δt is the temporal step size, N is the total number of temporal points.

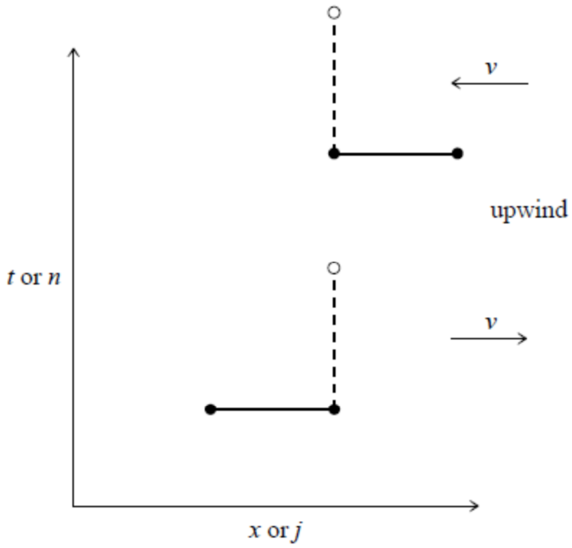

Figure 3-7 Representation of upwind differencing schemes. The upper scheme is stable when the advection constant v is negative, as shown; the lower scheme is stable when the advection constant v is positive, also as shown. The Courant condition must also be satisfied [37].

A common scheme to discretise such equations is known as upwind differencing, which is illustrated in Figure 3-7. The value of the function at time t_n and position x_j , i.e., $u(t_n, x_j)$, is denoted as u_j^n. On one hand, if the fluid flow is travelling in the positive direction as the spatial coordinate, the future value u_j^{n+1} is calculated from the u_j^n and u_{j-1}^n. On the other hand, if the fluid flow is travelling in the negative direction as the spatial coordinate, the future value u_j^{n+1} is calculated from the u_j^n and u_{j+1}^n. This scheme can be expressed as:

$$\frac{u_j^{n+1}-u_j^n}{\Delta t} = -v_j^n \begin{cases} \frac{u_j^n-u_{j-1}^n}{\Delta t}, & v_j^n > 0 \\ \frac{u_{j+1}^n-u_j^n}{\Delta t}, & v_j^n < 0 \end{cases}. \tag{3-15}$$

Furthermore, the spatial and temporal step size must be chosen such that the condition

$$C = \frac{|v|\Delta t}{\Delta x} \le 1, \tag{3-16}$$

is satisfied. This condition is known as the Courant condition and C is known as the Courant number. This is a necessary condition for the convergence of the solution of the difference equations. In the MATLAB program that I have developed, the Eqs. (3-4)-(3-7) are solved using the upwind differencing scheme by using a Courant number of ~0.8.

3.2.2.3 Comparison between simulated and measured pulses

In Section 3.2.1.3, the experimental results for different optical rises time are presented. In this section, the experimental condition is simulated by using the MATLAB program with the parameters shown in Table 3.

Table 3 Main parameters for the simulation of the Q-switched fibre ring lasers shown in Figure 3-2.

Parameter	Value	Notes
Pump wavelength	980 nm	Experimental value
Pump absorption cross section	$2.6842 \times 10^{-25}\mathrm{m}^2$	Based on Figure 2-14
Pump power	170 mW	Experimental value
Signal wavelength	1563 nm	Experimental value
Signal absorption cross section	$1.20639 \times 10^{-25}\mathrm{m}^2$	Based on Figure 2-14
Signal emission cross section	$2.11642 \times 10^{-25}\mathrm{m}^2$	Based on Figure 2-14
Er-ion lifetime at 13/2-level	11 ms	[22]
Mode radius of signal	2.75µm	Given in fibre datasheet
Signal overlap factor	0.6	Calculate from fibre datasheet assuming Gaussian mode profile.
Pump overlap factor	0.81	Calculate from fibre datasheet assuming Gaussian mode profile.
Absorption at 1530 nm	37.5 dB/m	Given in fibre datasheet
Absorption cross section at 1530 nm	$2.11642 \times 10^{-25}\mathrm{m}^2$	Based on Figure 2-14
Output FBG reflectivity	0.05	From FBG specification sheet
AOM insertion loss	7.87 dB	Measured value
AOM Extinction ratio	38.77 dB	Measured value
Courant number	0.8	Chosen
Temporal step size	0.435 ns	Chosen
Bandwidth of spontaneous emission	0.8 nm	Chosen
η_p,η_c	1	Chosen
Γ_s	0.60	Calculated
Refractive index of the fibre	1.45	[34]

The simulated and the measured pulses are compared in Figure 3-8. With the rise time of AOM is 35 ns, both the simulated pulse and the measured pulse (blue solid curve in Figure 3-8) exhibit similar pulse shape with the presence of MPP. An increase of AOM rise time to 70 ns makes the MPP less obvious in both simulation and experiment (green solid curve). With 150-ns AOM rise time, both the simulated pulse and the measured pulse exhibit similar pulse shape without MPP. Furthermore, the FWHM of the pulse are ~100 ns in all cases.

The measured pulse energies are ~2.70 µJ, 3.35 µJ and 3.35 µJ for the AOM rise times of 35 ns, 70 ns and 150 ns respectively. In comparison, the simulated pulse energies remains unchanged at 3.05 µJ for all AOM rise times. The lower measured pulse energy for the 35 ns rise time may due to the fact that the AOM cannot be fully switched ON by the 4 V output available from the Stanford pulse generator. Therefore, it is plausible to postulate that 3.35 µJ can be produced if the AWG can produce a 35 ns rise time. The postulated 3.35 µJ pulse is shown with blue dashed line in Figure 3-8(b). With this postulation, the relative peak power among the measured pulses are found to be very similar to the relative peak power of the simulated pulses, i.e., the pulse generated with a shorter AOM rise time has a higher peak power and the peak powers are around 30 W. Finally, it should be noted that no "fitted" parameter has been used in this experiment.

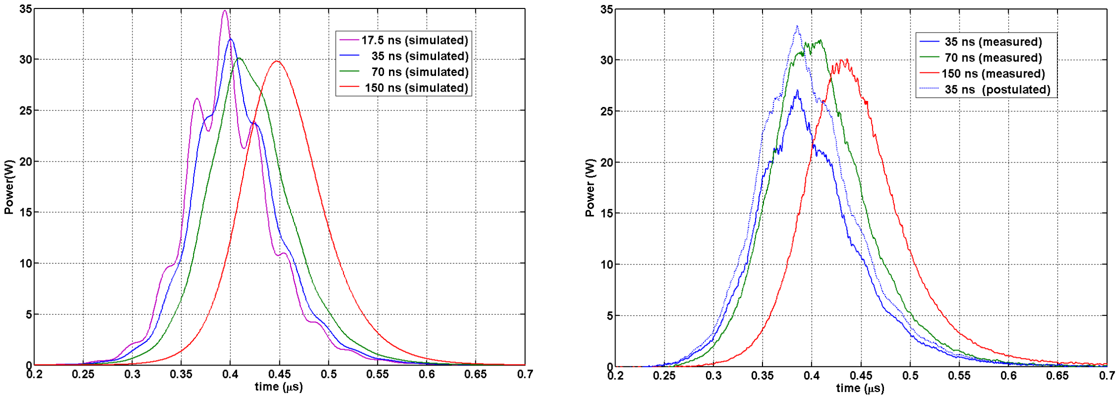

(a) (b)

Figure 3-8 Comparison of (a) simulated (b) measured and postulated pulses with different AOM rise time, τ_r.

From the discussion above, the simulated and the measured pulses are consistent with each other in term of pulse shape, pulse width, pulse energy and peak power. Therefore, the simulation model should be able to explain the general trends of the laser dynamics and the formation of MPP.

3.2.2.4 The origin and elimination of MPP

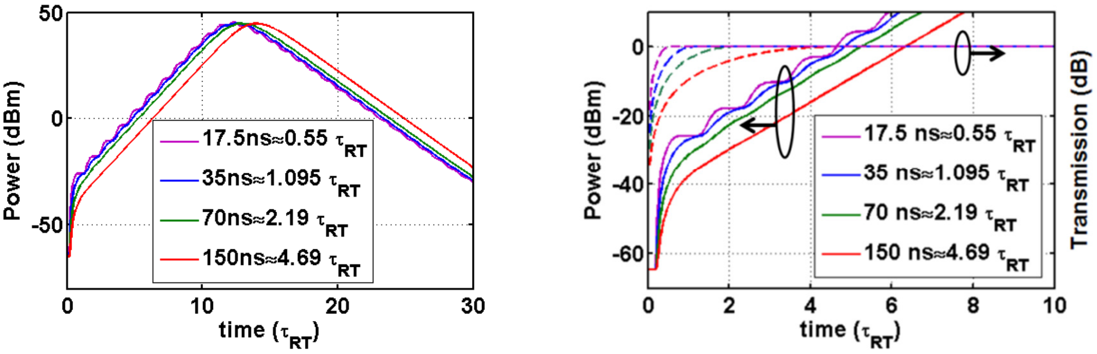

(a) (b)

Figure 3-9 Output pulses for various AOM rise times in dBm scale. The time axis is normalised to the cavity round trip time of the laser cavity. (b) Solid lines: the close-out of output pulses. Dashed line: the normalised transmission function of AOM, i.e., 0 dB corresponds to the maximum transmission of the AOM.

The elimination of MPP as the τ_r increases can be understood by considering the detailed pulse evolution process within the cavity. Figure 3-9(a) replots the Figure 3-8(a) such that the power is in dBm and the temporal axis is normalised to the cavity round trip time of the laser cavity. With this representation, MPP is apparent from the beginning of the pulse build up process. Solid lines of Figure 3-9(b) show the close up of output pulse evolution at the early stage of the pulse formation with different AOM transmission functions shown by the dashed lines with the corresponding colour.

In the early stages of pulse evolution i.e., soon after the AOM begins to open ($t < \tau_{RT}$), the output pulse profile follows the AOM switching profile. Hence, a fast AOM rise time (i.e., a small τ_r/τ_{RT}) defines a “seed pulse” during the first cavity circulation with a “step-like” pulse profile. For example with τ_r =17.5 ns, the “step-like” transmission function (dashed purple line) produces a “step-like” output pulse shape (solid purple line). When this “seed pulse” gets amplified during subsequent round trips through the amplifier and a pulse with a “staircase-like” envelope with a period of τ_{RT} emerges at the laser output. As the pulse energy increases and amplifier saturation takes place the step features on the original seed pulse increasingly sharpen (see purple line of Figure 3-8(a)) leading to the apparent substructure within the longer overall Q-switched pulse envelope. For longer AOM rise times the amplitude variation across the “seed pulse” formed during the first cavity round trip is less pronounced and a smooth pulse profile emerges during repeated cycles of amplification.

3.3 The MPP and nonlinear effects in Q-switched cladding-pumped fibre lasers

In this section, the nonlinear effects in cladding-pumped Q-switched fibre laser are investigated. Compared to the core pumping scheme laser in Section 3.2, a higher pulse energy can be generated in the cladding pumping scheme with the higher pump power available. However, as the pulse energy increases, the corresponding higher peak power starts to generate nonlinear effects. Hence, this section investigates the nonlinear effects in the Q-switched laser.

In Section 3.3.1, I show that nonlinearity is NOT required to initiate the MPP whereas previous work suggested that SRS/SBS might be responsible for MPP [35]. Next, the nonlinear effects occurs in my laser cavity are identified in Section 3.3.2. Section 3.3.3 investigates the interplay between MPP and nonlinear effects.

3.3.1 MPP in Q-switched cladding-pumped fibre lasers

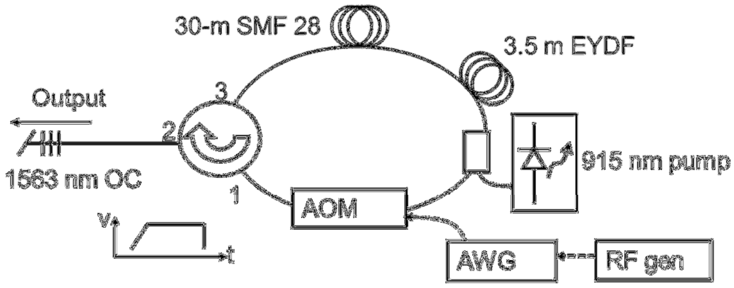

Figure 3-10 The schematic of the experimental setup for the Q-switched fibre ring laser. The estimated cavity length is ~37.5 m. The "V-t" plot illustrates the trapezoidal electrical gating pulse sent to the AOM.

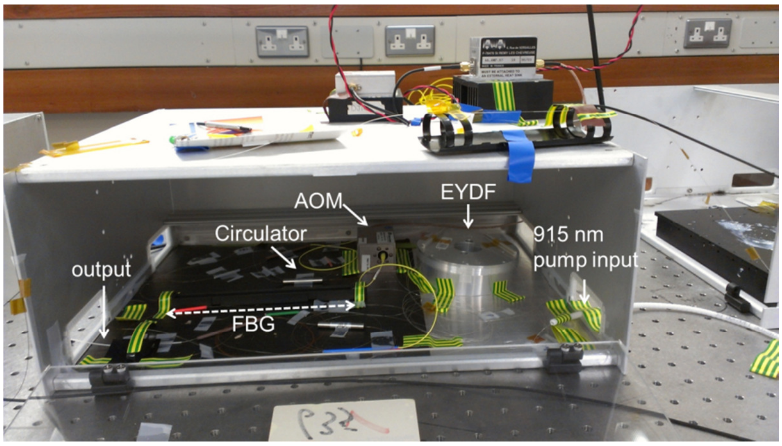

Figure 3-11 The Q-switched fibre ring laser is packaged in a metal box.

The experimental setup consists of a ring laser cavity as shown in Figure 3-10, which is similar to the Figure 3-2. The active fibre is a 3.5 m long Er/Yb-codoped GTwave fibre [25], which is pumped by a 915 nm multimode laser diode (LD). Furthermore, a 30-m SMF 28 fibre is included to exacerbate the MPP. The photo of the experiment setup is shown in Figure 3-11.

Figure 3-12 shows the pulse shapes generated with four different values of τ_r at a fixed pump power. The pulse shape generated with 70 ns τ_r (~0.37 τ_{RT}) is modulated with a subpeak distance of ~187 ns, corresponding to the round trip time (τ_{RT}) of the ring cavity. When τ_r is increased, the temporal modulation of the Q-switched pulse decreases. With a τ_r of 500 ns (~2.67 τ_{RT}), the modulation is no longer visible. Therefore, the MPP can be eliminated solely by increasing τ_r.

The average output powers remain at ~134 mW for all values of τ_r. This shows that the change of τ_r does not affect the energy extraction process despite the markedly different pulse shapes. The inset of Figure 3-12 shows the pulse spectrum measured with an optical spectrum analyzer (ANDO 6317B), which also remains unchanged for the various τ_r. No signature of a Raman peak can be observed at ~1660 nm in the measured spectrum. Hence, nonlinearity is not required to initiate the MPP.

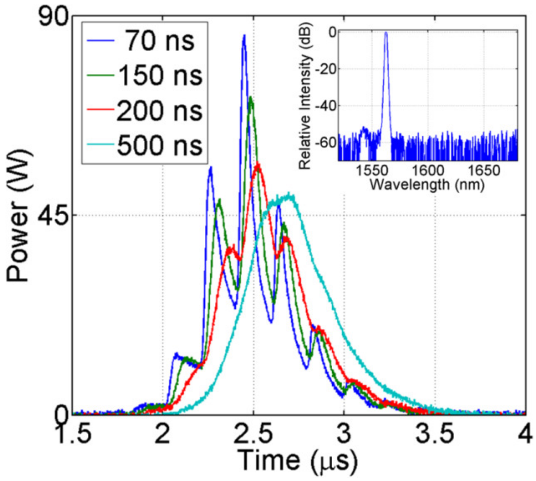

Figure 3-12 The pulses produced with 4 different values of τ_r at fixed pump power. The pulse spectrum (resolution=2 nm) is shown inset.

3.3.2 Nonlinear effects in Q-switched cladding-pumped fibre lasers

For a fixed pump power, a shorter laser cavity results in a shorter pulse width and a correspondingly higher peak power [31]. Therefore to see the impact of nonlinearity on a Q-switched pulse, the 30-m long SMF-28 fibre shown in Figure 3-10 was removed. With τ_r fixed at 500 ns, smooth single peak pulses are measured at all output power levels whilst changing the pump power. As an example, the pulse for an average power of 121 mW is shown in the inset of Figure 3-13.

Figure 3-13 also shows the spectra at various output power levels. At an average power of ~72 mW, the output spectrum is centred at 1562.5 nm (Peak A) and has a pulse width of 182 ns. When the output power is increased to ~92 mW, the pulse width decreases to 134 ns due to gain saturation [5]. The higher average power and shorter pulse width result in a higher peak power and consequently severe distortion to the output spectrum. Two sidebands at ~1550 nm and ~1574 nm start to appear in the output spectrum with a sideband suppression ratio (SBSR) of ~47 dB.

When the output power reaches ~121 mW, the SBSR decreases sharply to ~31 dB. At this power level, several sidebands are present, i.e., Peak B (~1576 nm), Peak C (~1584 nm), Peak D (~1605 nm) and Peak E (~ 1625 nm). This average output power corresponds to an estimated pulse peak power of ~1.3 kW after the active fibre (taking into account the insertion loss of the AOM of ~7.97 dB). At this peak power and anomalous dispersion of the cavity fibre, the spectral position of Peak C is consistent with peak C being generated from the high peak power pulses at Peak A via modulation instability (MI) [38]. The peak D (Peak E) are created through four wave mixing (FWM) between Peak A and C (Peak C and Peak D) respectively. Peak B is the MI-sideband created in the output fibre after the Q-switched pulse passes through the AOM and out of the system. Furthermore, the absence of a Raman stokes at ~1660 nm in the measured spectrum, shows that the threshold of nonlinear wavelength conversion due to MI and FWM is lower than that of stimulated Raman scattering (SRS).

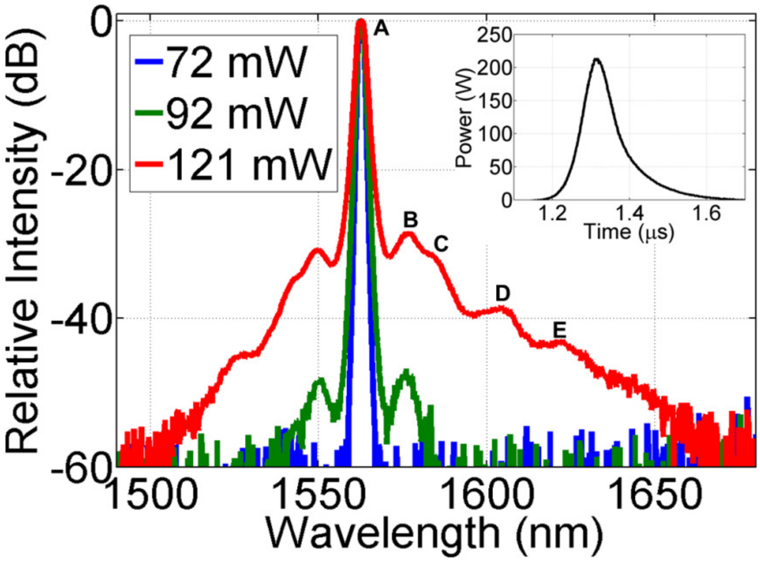

Figure 3-13 The normalised output spectra (resolution= 2 nm) at 3 average output powers. The spectra correspond to the average power (estimated peak power/ pulse width) of 72 mW (71 W/182 ns), 92 mW (115 W/ 134 ns), 121 mW (208 W/ 92 ns. Inset shows the pulse corresponding to 121-mW average power.

3.3.3 The interplay of MPP and nonlinearity

The interplay of MPP and nonlinearity was then studied by reducing τ_r from 500 ns to 70 ns at a fixed pump power. While both the average output power (i.e., ~121-mW) and output spectra remain unchanged, the single temporal peak pulse (lower inset of Figure 3-14(b)) evolves into a double-peak pulse (lower inset of Figure 3-14(c)). The spectral evolution across the pulse was measured by using a spectrally resolved optical time gating technique as shown in Figure 3-14(a). The output of the Q-switched laser is fed into an electro-optic modulator (EOM) through a 20-dB tap coupler. A radio frequency generator (RF gen) is used to trigger both the Q-switched laser and a square-pulse generator (SQRT-pulse gen). The SQRT-pulse gen the EOM with a pulse width and time delay that can be varied by a personal computer (PC). Note that the spectra obtained at various time delays also consist of a background component due to the limited EOM-extinction ratio (~35 dB) which needs to be removed during the data analysis.

For the case of τ_r = 500 ns (Figure 3-14(b)), the central wavelength (~1562.5 nm, corresponding to Peak A in Figure 3-13) of the pulse spectrum remains unchanged across the pulse. The effect of self-phase modulation (SPM) can be seen as the spectrum broadens monotonically towards the peak of the pulse (at ~1320 ns) and narrows down thereafter. The MI and FWM result in a larger temporal width at the spectral position of ~1576 nm, ~1584 nm and ~1605 nm corresponding to Peak B, Peak C and Peak D respectively in Figure 3-13.

The near-uniform temporal spacing between the contours at times before 1250 ns shows that the signal (Peak A) builds up exponentially during the initial phase. The growth of the signal starts to saturate at ~1290 ns accompanied by the formation of MI-sidebands (Peaks B and C). The growth of the MI-sidebands starts to saturate (at ~1310 ns) when the FWM-sideband (Peak D) starts to appear. Beyond the pulse peak the signal decays at a slower rate than the initial growth rate as indicated by the larger temporal spacing between the contours.

Figure 3-14(c) shows the spectral evolution for τ_r =70 ns. In contrast to the previous case, MPP does not allow the pulse to build up in a purely exponential manner as indicated by the non-uniform temporal spacing between the contour lines before 1050 ns. Furthermore, the pulse spectral evolution exhibits a local minimum (i.e., the spectrum is the narrowest) at ~1105 ns and two local maxima at ~1090 ns and ~1120 ns. The 1090-ns and 1120-ns maxima correspond to the two sub-peaks of the temporal pulse profile shown by the lower inset whilst the 1105-ns region occurs due to the reduced pulse intensity in-between the sub-peaks. The stronger nonlinearity at the second sub-peak compared to the first sub-peak is consistent with the higher peak power associated with the second sub-peak. The interplay of MPP and nonlinearity is thus seen to strongly affect the detailed spectral evolution.

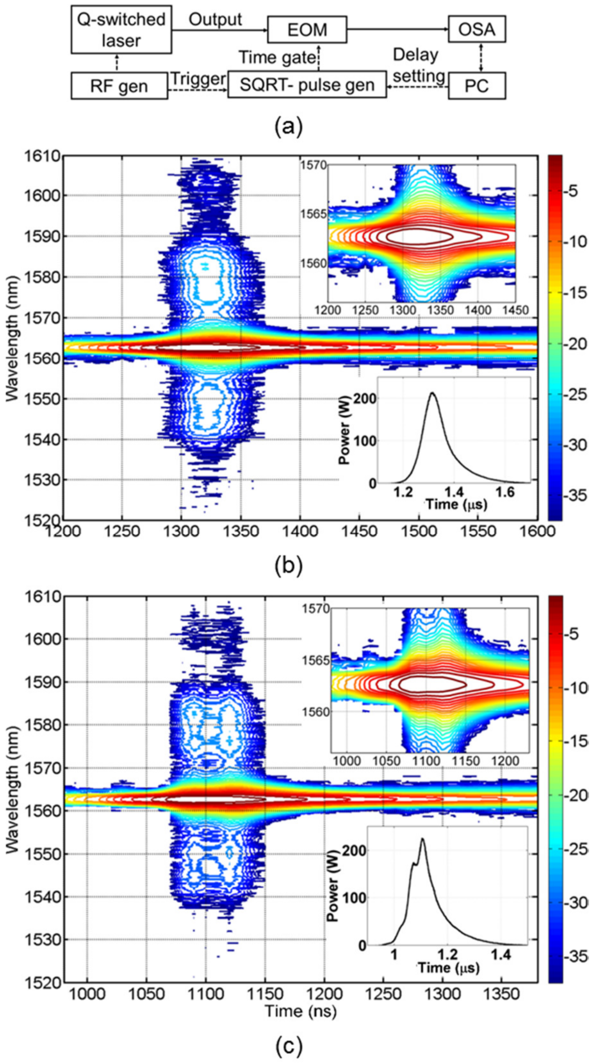

Figure 3-14 (a) Setup for spectrally resolved optical time gating method. The optical fibre/ electronic connections are shown in solid/dashed lines. The normalised pulse-spectrum evolution with a τ_r of (b) 500 ns and (c) 70 ns respectively (temporal resolution=10 ns, wavelength resolution=2 nm). The contour lines are separated by 1.50 dB step. In (b) and (c), the upper and lower insets show the close-up of the spectral and temporal evolution of the pulse.

3.4 Conclusion

I have investigated through experiment and simulation the impact of shaping the Q-switch gating window in Q-switch fibre lasers and have shown that the MPP can be simply eliminated in this way. I have shown that nonlinear effects play no role in instigating the MPP and it is due to gain dynamics/the AOM rise time alone. My results show that MI can develop within an anomalous dispersive, Q-switched fibre laser and that the complex interplay of MPP and nonlinearity changes the detail of the spectral evolution. My results highlight the value of using spectrally resolved time gating to study pulse formation in Q-switch fibre lasers.

Chapter 4 Continuous wave in-band pumped fibre amplifiers

High power 1.55 µm erbium (Er) based fibre lasers are attractive for numerous applications, such as materials processing and military applications, where light scattered off-target is a great concern in terms of eye safety. The realization of high power 1.55 µm Er-based high power lasers however presents a number of key challenges, not least, achieving sufficient pump absorption per unit length, obtaining sufficiently high power conversion efficiency and the availability of suitably high brightness pumps at the desired wavelengths. Compromises need to be struck to realise practical devices and the optimum design choices made will depend strongly on the specific application. In this chapter, the strategy for the power scaling of high power continuous wave in-band pumped Er-based fibre amplifiers is investigated.

Chapter 4.1 describes the background for this chapter, which furthers the discussion on the properties of erbium doped fibre amplifiers in Section 2.3. Section 4.2 presents the state of the arts in this area. Section 4.3 presents the characteristics of the in-band pump source used in this chapter and Chapter 5.

In Section 4.4, I assess the performance of two different fibres and develop simulation models that are fitted to experimental results for both fibres. The simulations show that the performance of the high power fibre amplifier is strongly affected by concentration quenching. In Section 4.5, with the experimentally validated model, I compare the performance of the amplifiers with different pumping arrangements, i.e., the core-pumping scheme (CRS) versus cladding-pumping scheme (CLS) and the forward-pumping (FP) versus backward-pumping (BP) scheme. My results show that the both CLS and BP can be exploited to mitigate the detrimental effect of concentration quenching. Hence, I predict that ~ 77% PCE with high output power is feasible using backward cladding pumping in conjunction with operation at long signal wavelengths around 1605 nm. Finally, I validate this prediction with cladding pumped experiments identifying in the process that excess pump loss in this instance due to the high absorption by the cladding materials is an impediment to this in current commercial fibres

4.1 Background

In this section, I start by introducing the concept of net cross section in Section 4.1.1. In Section 4.1.2, I describe the energy transitions of erbium ions that lead to the non-radiative loss of pump photon energy. Section 4.1.3 describes the simulation model for the concentration quenching in EDF. Section 4.1.4 further discusses concentration quenching in highly doped erbium doped fibres. Section 4.1.5 discussed the codoping of ytterbium in EDF for the in-band pumped EDFA.

4.1.1 Net cross section and transparency inversion

In this section, I discuss the net cross section in in-band pumped erbium doped fibre amplifier, which can be used to analyse the general trends in the behaviour of in-band pumped erbium doped fibre amplifiers. Based on Eq. (2-53), we can define the net cross section per ion basis as [22]:

$$\sigma_{net}(\lambda) = \sigma_e(\lambda)n_2 - \sigma_a(\lambda)n_1, \quad (4\text{-}1)$$

where n_2 and n_1 are the normalised ion densities (with respect to the total ions) in the upper and lower energy level respectively, while $\sigma_e(\lambda)$ and $\sigma_a(\lambda)$ are the emission and absorption cross section respectively. The net cross-section describes the gain and the absorption properties of fibre amplifiers at a particular inversion level.

An in-band pumped erbium doped fibre amplifier is essentially a quasi-three level laser system which involves only two energy manifolds, i.e., the $^4I_{15/2}$ ground-state manifold and the $^4I_{13/2}$ lasing manifold. In such a laser system, there is an inversion level where pump saturation occurs, i.e., no further pump photons can be absorbed to excite ions from the ground-state level into the lasing level. In the literature this situation is typically known as pump saturation and, in this thesis, I also refer to it as population inversion saturation. When the saturation of pump absorption and population inversion occurs, the active medium exhibits neither amplification nor absorption and becomes transparent at the pump wavelength, i.e., $\sigma_{net}(\lambda) = 0$. From Eq. (4-1), the transparency inversion level can be derived as:

$$n_{transparency} = \frac{\sigma_a(\lambda)}{\sigma_e(\lambda)+\sigma_a(\lambda)}. \quad (4\text{-}2)$$

Based on the cross section in Figure 2-14, the transparency inversion across wavelength is shown in Figure 4-1. For a given in-band pump wavelength, the transparency inversion level corresponds to the maximum inversion level that can be achieved, when the active fibre is pumped at the pump wavelength. The two red dashed lines show that the maximum inversion of ~0.78 and ~0.50 can be reached when the active fibre is pumped at 1480 nm and 1535 nm respectively. Similarly, for a given signal wavelength, the input signal can extract gain from the active fibre only when the inversion level is above the transparency level. The two blue dashed lines shows that the signal at 1565 nm and 1605 nm can extract gain from the EDF until an inversion level of ~0.35 and ~0.20 respectively.

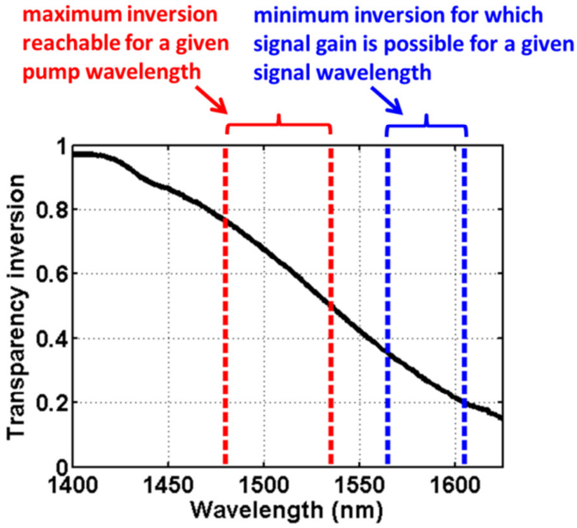

Figure 4-1 The transparency inversion across wavelength based on the cross section in Figure 2-14. The two red dashed lines show that when the erbium fibre amplifier is pumped at 1480 nm and 1535 nm, the maximum inversion that can be reached is ~0.78 and ~0.50 respectively. Similarly, the blue dashed lines show that the

signal at 1565 nm and 1605 nm can extract gain from the EDFA until an inversion level of ~0.35 and ~0.20 respectively.

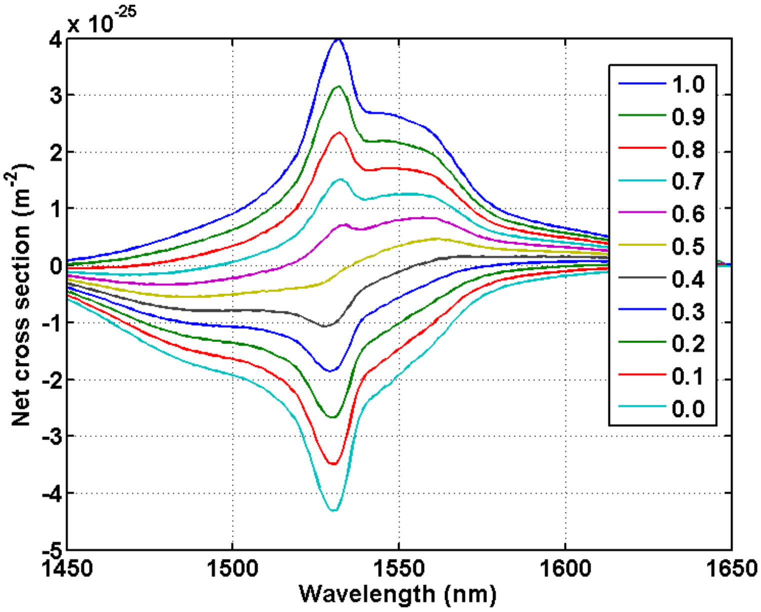

Figure 4-2 Net cross section for various inversion levels between $^4I_{15/2}$ and $^4I_{13/2}$ manifolds of the erbium ion based on the cross section in Figure 2-14.

Based on the cross section in Figure 2-14, the $\sigma_{net}(\lambda)$ at the different inversion levels are shown in Figure 4-2. At a normalised inversion of 0.0, the ion exhibits absorption across the spectrum with the maximum absorption peak at 1530 nm. In my experiments I use a pump wavelength of ~1535 nm since this represents the shortest wavelength that my pump fibre laser can operate efficiently at. When the erbium doped fibre is pumped at 1535 nm, the inversion level starts to increase and the absorption at 1535 nm decreases. At the transparency inversion of ~0.5, the $\sigma_{net}(\lambda)$ exhibits a zero crossing at 1535 nm. At this inversion, the ion exhibits absorption below 1535 nm and amplification above 1535 nm. The gain peak at this inversion level locates at ~1562.5 nm. However, if the EDF is pumped with 1480 nm, the inversion can further develop up to 0.78 with the gain peak located at ~1535 nm.

Between inversion levels of 0.0-0.4, $\sigma_{net}(\lambda)$ exhibits stronger absorption at 1535 nm than at 1480 nm. Hence, at these inversion levels, the pump absorption at 1535 nm is more efficient than at 1480 nm. In another words, for the same pump power available and same active fibre length, the EDF can absorb more 1535 nm pump power than 1480 nm pump power. Therefore, even though it is possible to achieve a higher inversion level with 1480 nm pump wavelength, the 1535 nm pump wavelength will be more pump power-efficient for the in-band pumping scheme if low inversion level operation can be accepted.

4.1.2 More on erbium ion transitions

The discussion so far involved only the transition between the three most important energy levels of Er^{3+} for the 1.55-µm radiation generation, i.e., the $^4I_{15/2}$ ground-state manifold, the $^4I_{13/2}$ lasing manifold and the $^4I_{11/2}$ excited manifold (see Section 2.3.2). However, the Er^{3+} ion exhibits many more energy levels as shown in Figure 4-3. As a result, many other transitions are possible in the Er^{3+}-ion even just with a pump wavelength of ~1.55 µm [39, 40]. In the in-band pumped EDFA, the Er^{3+} ion is directly excited to the $^4I_{13/2}$ level for the amplification of the signal power through the stimulated emission between $^4I_{13/2}$ and $^4I_{15/2}$ levels. Therefore, any transitions of the $^4I_{13/2}$-ions to higher energy levels (such as $^4I_{9/2}$ level) are detrimental for the in-band pumped EDFA because it consumes the energy from the $^4I_{13/2}$-ions, which would otherwise be used to amplify the signal power if these detrimental transitions are absent. As a result, the conversion efficiency of the absorbed pump power to the signal power decreases.

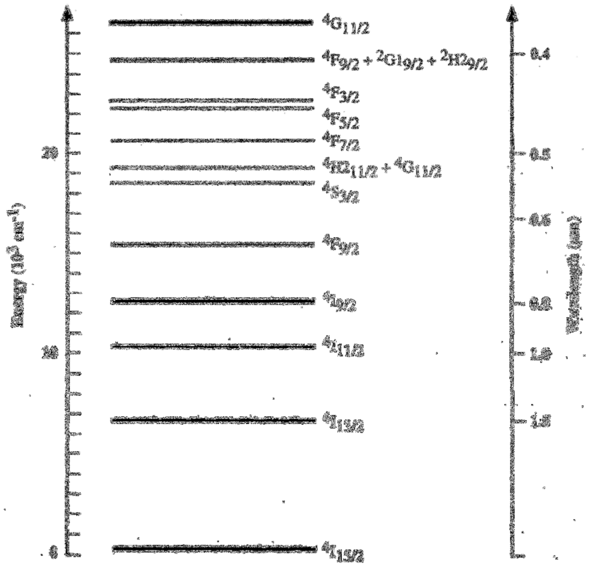

Figure 4-3 Energy level structure of erbium ion. The wavelength scale corresponds to the wavelength of the transition from a given energy level to the ground state [22].

In the following, I briefly describe the different mechanisms that allow the transition of $^4I_{13/2}$-erbium ions to the $^4I_{9/2}$ level. From the $^4I_{9/2}$ level, most of the ions decay to the $^4I_{11/2}$-intermediate level. While at $^4I_{11/2}$ level, some of the ions can make a direct transition to the $^4I_{15/2}$ ground-state with the generation of 980 nm radiation.

4.1.2.1 Excited state absorption (ESA)

An erbium ion in the excited state exhibits its own absorption cross section. Hence, if the pump or signal wavelength falls within the absorption band of the excited ions, excited state absorption (ESA) will happen. Since ESA is the absorption property of the ions in a certain state, it is a process that is concentration independent. In this work, the $^4I_{13/2}$-ion exhibits absorption at both pump and signal wavelengths, i.e., 1.5-1.6 µm [19, 39, 41] that allow the $^4I_{13/2}$-ion to make a transition to $^4I_{9/2}$ level, as illustrated in Figure 4-4(a). Furthermore, with the long life time of the erbium ion in the $^4I_{13/2}$ level, the transition originating from the erbium ion in the $^4I_{13/2}$ level is likely to occur. The ions decay rapidly from $^4I_{9/2}$ level to $^4I_{11/2}$ level with a lifetime of ~5 ns [41]. However, the life time of the $^4I_{11/2}$ level is rather long (i.e., ~5.2 µs). During this duration, about 1 out of 1000 of the ions can make a direct transition to $^4I_{15/2}$

level by emitting 980 nm photon [19]. Meanwhile, the ions at the $^4I_{11/2}$ level also exhibit an absorption cross section at ~980 nm [41]. Hence, the 980 nm radiation emission from the ions can also be re-absorbed by other erbium ions at $^4I_{11/2}$ level through ESA and allow the ion to transit to $^4F_{7/2}$/ $^2H_{11/2}$/ $^4S_{3/2}$ level, as shown in Figure 4-4(b). This results in the characteristic green emission at ~520-545 nm, which can be easily observed with the naked eye. The effect of ESA can be modelled by introducing the excited state absorption cross section to the power propagation equation of the wavelength under consideration and the corresponding change in the rate equation for the ions at the different energy states [22, 41].

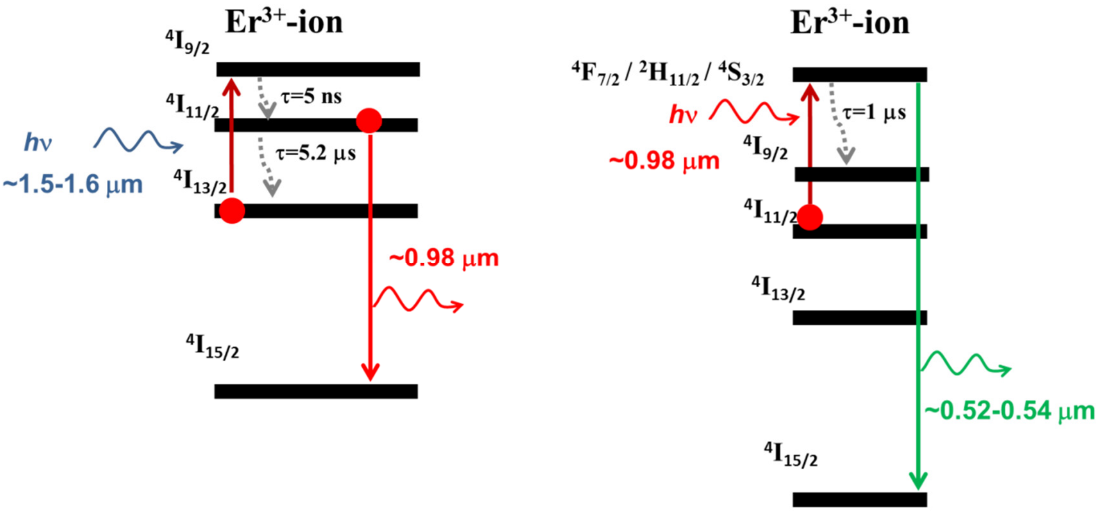

(a) (b)

Figure 4-4 (a) An illustration of the excited state absorption of 1.5-1.6-µm radiation by erbium ions in the $^4I_{13/2}$ level. (b) An illustration of the excited state absorption of ~0.98 µm radiation by an erbium ion in the $^4I_{11/2}$ level. Some of the ions at the $^4F_{7/2}$/ $^2H_{11/2}$/ $^4S_{3/2}$ level will emit green radiation at ~0.52-0.54 µm.

4.1.2.2 Upconversion

The upconversion is an ion-ion interaction process, meaning that the ions exchange energy with each other non-radiatively. In this work, I only consider the interaction between two erbium ions in the $^4I_{13/2}$ level (see Figure 4-5). When the $^4I_{13/2}$-ions exchange energy, the energy that is transferred from the donor ion to the acceptor ion corresponds to the energy gap between $^4I_{13/2}$ and $^4I_{9/2}$. Hence, the acceptor will be excited to $^4I_{9/2}$ while the donor losses it's energy and decays to $^4I_{15/2}$. After that, the excited ion at $^4I_{9/2}$ level can undergo the decay process illustrated in Figure 4-4(a), as well as the 980 nm ESA illustrated in Figure 4-4(b). Consequently, the upconversion also results in the characteristic green emission at ~520-545 nm. The upconversion becomes dominant with an increase in ion concentration. Hence, it is also known as concentration quenching in the literature.

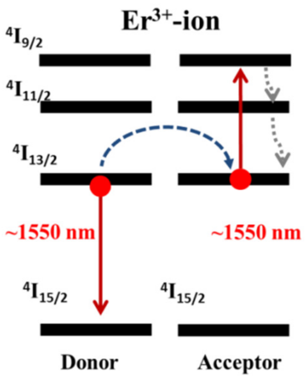

Figure 4-5 An illustration of the energy level diagram in the upconversion process of erbium ion in $^4I_{13/2}$.

The nature of the upconversion strongly depends on the physical distance of the interacting ions from each other [42]. The typical average distance between the ions in an EDF is on the nm-scale. For example, based on the cross-section data in Figure 2-14 the concentration of the pure erbium doped fibre EDF (Liekki Er 60-40/140DC) used in my experimental was estimated as N=3.23×10^{25} /m^3, which corresponds to an average ion-ion distance (r) of ~3.14 nm, i.e., $r=(1/N)^{1/3}$. However, in practice, the ion distribution is not fully random and many ions reside closer to each other than the average distance and this can lead to concentration quenching. Several models to describe the concentration quenching in erbium doped fibre are to be found in the literature [22, 42-45].

In this work, the concentration quenching is modelled using the homogenous upconversion (HUC) and pair induced quenching (PIQ) models, which has successfully been used previously to characterize and describe the performance of high concentration EDFAs [22, 42, 43]. In Figure 4-6, the glass matrix of the optical fibre is represented in two dimensions. The open structure of the glass matrix results in relatively large gaps between atoms, in which erbium ions can be incorporated [42]. In the upper part of the figure, the homogenous upconversion (HUC) between the erbium ions is illustrated. In the lower part, the inhomogeneous upconversion of two erbium ions known as pair induced quenching (PIQ) is illustrated.

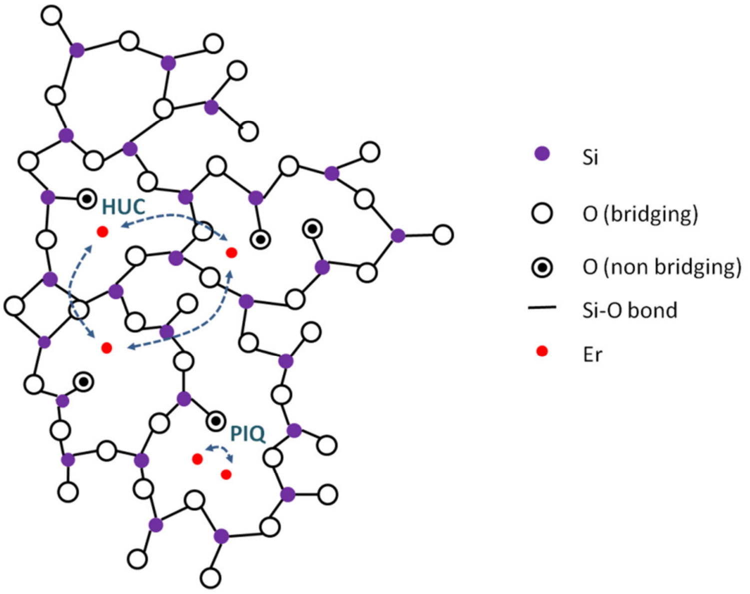

Figure 4-6 A two dimensional model of silica glass network with erbium doping. The two different types of upconversion, i.e., the homogenous upconversion (HUC) and the pair induced quenching (PIQ) are schematically shown [42].

Homogenous upconversion (HUC)

The homogenous upconversion among two erbium ions occurs when the local inter-ion distance is ~2 nm [46]. The ions can be assumed to be uniformly distributed such that the probability of energy exchange among all the ions is the same. The homogenous upconversion between two erbium ions can then be modelled by introducing the term $-C(N_2)^2$ in the rate equation of the population density, where C is the upconversion coefficient. This term can be expressed as $-C{\bullet}N_2.N_2= -W_{UC}{\bullet}N_2$ where $W_{UC}= C{\bullet}N_2$ is the rate of upconversion. Therefore, we see that the upconversion rate W_{UC} is proportional to the population density of erbium ions in the $^4I_{13/2}$ level [47]. The upconversion lifetime τ_{UC} is defined as $1/N_TC$, with N_T the total ion concentration. With the typical value of C and the N_T, the upconversion lifetime is typically in the range of millisecond range [48].

Pair induced quenching (PIQ)

In this process, the local inter-ion distance is about the same order of the diameter of the erbium ion, i.e., ~0.2 nm, such that the two closely spaced ions form an ion-pair [46] as illustrated in the lower part of Figure 4-6. The close distance of the ions is a result of the inhomogeneity in the ion distribution in the active region, rather the average distance between the ions. Due to the close distance, the energy transfer between the two $^4I_{13/2}$-ions is rapid. In fact, it has been measured that the lifetime that both $^4I_{13/2}$-ions of the ions-pair remain in $^4I_{13/2}$ is ~50 ns [49] before the energy exchange between them occurs. Therefore, in the continuous wave operation, it can be assumed that there is only one of the ions in the ion-pair is in the $^4I_{13/2}$ level at any one time. To model this effect in the case of continuous wave operation, the ions-pair is assumed to make transition between two states. In State I, the probability of an ion-pair absorbing a photon is twice that of a single independent ion because an ion-pair in State I consists of two ground state ions. On the other hand, in State II, the stimulated emission rate of ion-pair is the same as the single excited ions because an ion-pair in State II consists of only one excited state ion. Furthermore, since the PIQ is due to local inhomogeneity of the ion concentration, the fraction of ions exhibit the PIQ is expressed as *2k*, where *k* is known as the pair ion ratio.

4.1.3 Simulation model for the upconversion of erbium ions

In this section, the simulation model for the concentration quenching in erbium doped fibre is briefly described. Since the average ion separation of the fibre used in this work is ~3 nm, I have neglected the effect of ESA at 1.5-1.6 μm as will be explained in Section 4.1.4. In fact, I have also attempted to incorporated the effect of ESA with the absorption cross section data from [50] and found that the ESA induced pump energy loss is too large, and therefore is unphysical, in comparison to my experimental result. Thus, only the effect of homogeneous upconversion (HUC) and pair induced quenching (PIQ) are considered in this fibre.

The optical power in the amplifier was modelled using the propagation equation in the standard EDFA model (see Section 2.3.1), while the effect of the concentration quenching is considered in the rate equation for the erbium ions in the active fibre [22, 42, 43, 48, 51, 52]. The ions are assumed to have undergone two possible types of ion-ion interactions, namely the HUC and PIQ [22, 42, 43, 48, 51, 52]. In this model, all ions are classified as belonging to one of two distinct species of ion: independent ions and paired-ions. In the case of paired-ions, two ions form an ion-cluster due to their close proximity. If *2k* is defined as the fraction of paired-ions and N_t is the total ion concentration, then the total ion concentration existing in a paired-ion state, N_t^k, is given by $N_t^k = 2kN_t$. Likewise, the total number of independent ions, N_t^i, is given by $N_t^i = N_t - N_t^k = N_t(1-2k)$.

The independent ions can undergo HUC, where the non-radiative energy transfer between the two $^4I_{13/2}$-excited ions results in one ion decaying to the ground state whilst another ion is excited to the $^4I_{9/2}$-level. The $^4I_{9/2}$-excited ions then rapidly relax to either the $^4I_{11/2}$ or $^4I_{15/2}$-level. Under the steady state condition, the rate equation for independent ions is [22, 48] :

$$N_2^i = \frac{R_{12}^i N_t^i}{A_i + R_{12}^i + R_{21}^i + (1+\frac{1}{m})CN_2^i}. \tag{4-3}$$

In the above equation, the superscript *i* signifies rates for independent ions. $1/m$ is the branching ratio for the relaxation process to $^4I_{11/2}$ and $^4I_{15/2}$, N_2^i is the population density of the upper lasing level ($^4I_{13/2}$), C is the upconversion coefficient. R_{12}^i, R_{21}^i and A^i are the absorption, stimulated emission and spontaneous emission rates respectively.

In the paired-ion case, when both ions of the ion-cluster are excited, the non-radiative energy transfer between them is so fast that only one ion of the ion-cluster can remain in the excited state [22, 42, 43, 51]. The difference between PIQ and HUC is that, in the case of HUC, if an ion is excited, it does not prohibit neighbouring ions moving to the excited state. However, in the case of PIQ, when one ion of an ion-cluster goes to the excited state, the other ion in the ion-cluster must be in its ground state [22]. As a result, the ion-cluster can be in either of two states: State I: two ions in the ground state, or State II: one ion in the excited state and one ion in the ground state. Under steady state conditions, the rate equation describing the ion population density of paired ions is [51]:

$$N_2^k = \frac{R_{12}^i N_t^k}{A_i + 2R_{12}^i + R_{21}^i}. \tag{4-4}$$

In the above equation, the superscript k signifies the rate for the ion-cluster. N_2^k is the ion population density of paired ions in the upper lasing level ($^4I_{13/2}$).

Overall, the population density of the excited ions in the steady state considering the effects of both HUC and PIQ is [42]:

$$N_2 = N_2^i + N_2^k = \frac{R_{12}^i N_t (1-2k)}{A_i + R_{12}^i + R_{21}^i + (1+\frac{1}{m})CN_2^i} + \frac{R_{12}^i 2kN_t}{A_i + 2R_{12}^i + R_{21}^i}. \tag{4-5}$$

If the HUC is neglected, i.e., (C=0), the first and second term in the right hand of Eq. (4-5) represent the normal ions without upconversion and the paired-ions respectively. By comparing the denominators of the two terms, one can see that even though the absorption rate of paired-ions ($2R_{12}^i$) is twice that of normal ions (R_{12}^i), their rate of stimulated emission (R_{21}^i) and spontaneous emission (A^i) are the same as for the normal ions. The extra absorbed energy of the paired-ions is lost through the non-radiative process illustrated in Figure 4-5. The detailed derivation of Eqs. (4-3) to (4-5) can be found in Section 7.1.

In this work, the Optisystem program was used to model the concentration quenching based on the model described above.

4.1.4 Discussion on ion concentration quenching

Figure 4-7 shows the picture taken in ambient lighting showing the characteristic green emission through the process illustrated in Figure 4-4(b). This can be induced by any combination of the transitions originating from $^4I_{13/2}$ as described in Section 4.1.2, i.e., the 1.5-1.6-μm ESA, homogeneous upconversion and pair induced quenching.

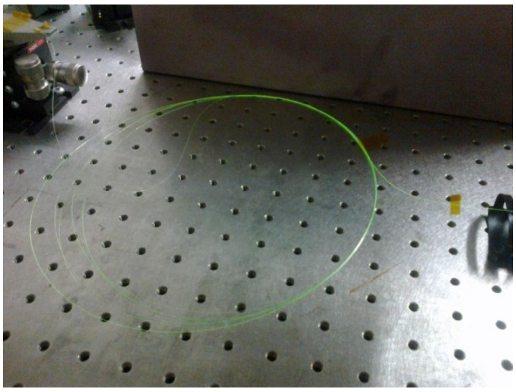

Figure 4-7 The green florescence emission when pure-erbium doped large mode area (Liekki Er 60-40/140DC) is strongly pumped by 1535 nm at 16-W input pump with core-pumping scheme.

The dominant transition in a particular experiment mainly depends on the ion concentration, host material and the fabrication process of the EDF under test. This can be best illustrated with reference to a series of experiment performed by J. Nilsson et al. [19] on EDF with the following core composition $SiO_2/GeO_2/Al_2O_3$ of 93/5/1% by weight. Figure 4-8 (a) shows the 980 nm fluorescence measured from a series of 7 fibres pumped at 1480 nm under the same conditions. Below ion separations of ~8 nm, the 980 nm fluorescence increases rapidly (Note the logarithmic scale.). This implies that below ~8 nm the upconversion processes dominates over ESA because upconversion is concentration dependent while the ESA is not. For lower concentrations, ESA seems to dominate. (Note that even though there are only limited sample points at large ion separations (>9 nm), this conclusion is consistent with the literature that ESA is dominant only at low ion concentrations [41]). Figure 4-8(b) shows the 980 nm fluorescence power plotted against the 1500 nm fluorescence power of the fibre for an ion separation of ~5.4 nm (620 ppm by weight). If there is only an HUC process, the relations between the powers of the 980 nm fluorescence and of the 1500 nm fluorescence while increasing the pump power should, on a logarithmic scale, be linear because the 980 nm fluorescence depends of the square of the population inversion and the 1500 nm fluorescence has a linear relationship with population inversion. On the other hand, the PIQ contribution would grow in a different manner [19]. The result (see Figure 4-8(b)) shows that the relationship between the two fluorescence powers clearly deviates from linear. Hence, the PIQ is present and may be accompanied by HUC. Even though the PIQ model has been able to explain many experiment results, there is no direct proof of ion-pair formation in silica glass [44, 45, 52]. Hence, the pair ion ratio of fibre is determined through the fitting of simulation results to experimental results [42]. In this work, I choose to fit the MOPA behaviour under high power operation because this is the actual operating condition in my MOPA system.

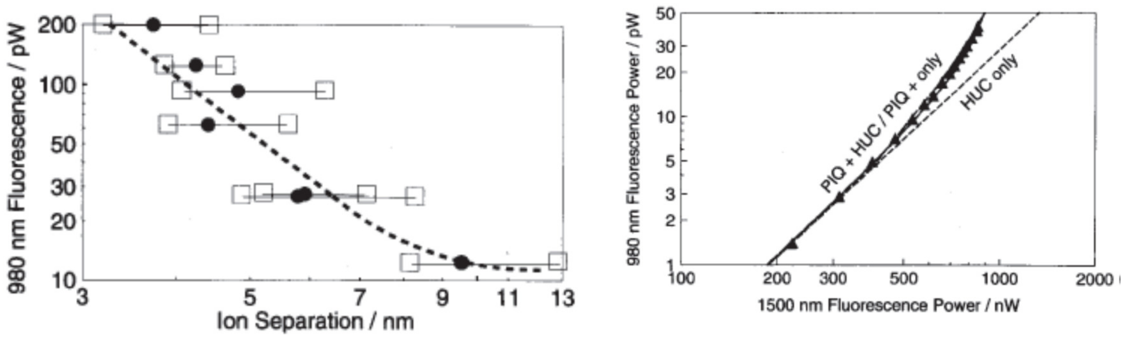

(a) (b)

Figure 4-8 Measured backward fluorescence power at 980 nm for seven different long fibres when pumped by 25 mW at 1480 nm [19]. Note that the graphs are on a logarithmic scale.

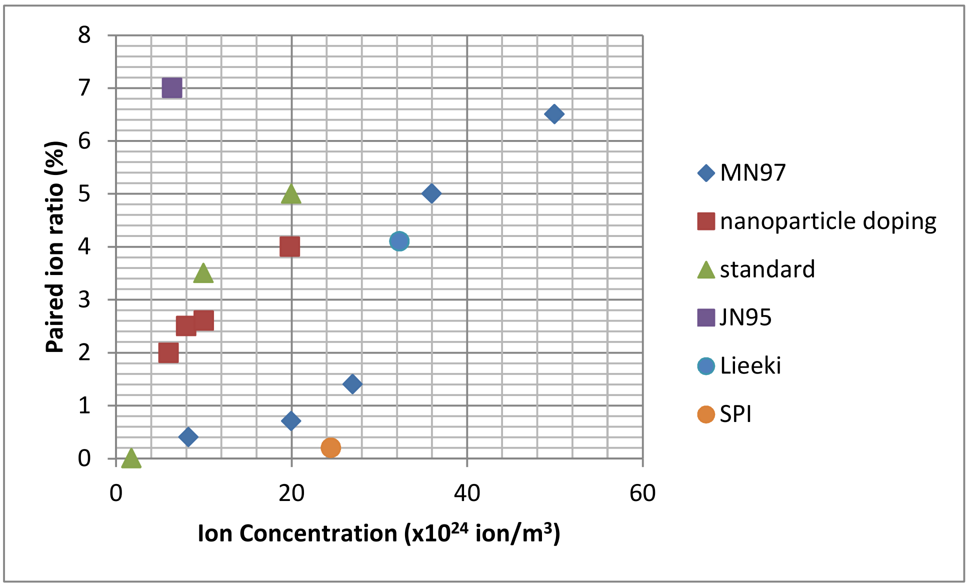

Figure 4-9 The fitted paired ion ratio against ion concentration. The MN 97 corresponds to [42]. The nanoparticle doping and standard corresponds to the fibre in [52] fabricated with nanoparticle-enabled and standard MCVD respectively. JN95 corresponds to the fibre in [19]. Lieeki corresponds to the Er-LMA used in Section 4.4. SPI corresponds to the EYDF used in Section 4.4.

Figure 4-9 shows the paired ion ratio against the ion concentration determined in the literature. The trend in the figure shows that within the same series of tests (as indicated by the same markers), the pair ion ratio increases with the ion concentration. This is consistent with the data shown in Figure 4-8(a). Furthermore, the fibres tested in “MN97” [42], “JN95” [19], “Standard” [52] and “nanoparticle doping” [52] have been co-doped with aluminium as it has been reported by many authors that the incorporation of aluminium reduces the PIQ [53, 54]. With the molecular chemical vapour deposition (MCVD)-compatible nanoparticle doping method developed by Draka, the level of PIQ has been reduced as shown by the lower pair ion ratio of “nanoparticle doping” compared to “standard” [46, 52, 55]. Furthermore, the MCVD-nanoparticle doping has also produced fibre that exhibits HUC that is independent of ion concentration. The data point “Lieeki” in Figure 4-9 corresponds to the paired ion ratio of the the commercial pure-Er LMA (Liekki Er60-40/140) used in Section 4.4. I am not able to elaborate much on the host composition because this information is unavailable. However, the fibre is likely to be fabricated with the direct nanoparticle deposition (DND) developed by Liekki. The fibre fabricated with this method has also demonstrated the suppression of pair induced quenching in EDF [56, 57].

4.1.5 Ytterbium codoping in in-band pumped EDFA

The “SPI” in Figure 4-9 exhibits an extremely low paired ion ratio. This fibre corresponds to the in-house fibre used to demonstrate a record 80% power conversion efficiency (PCE) in Section 4.4. The PCE is defined as the ratio between the converted signal power to the absorbed pump power.

Originally, this fibre was designed to operate as a 9xx nm pumped EYDF, in which the ratio of ion concentration of ytterbium to erbium is probably ~15-18 with a phosphosilicate host [21]. A possible explanation for such a low pair ion ratio when this fibre is in-band pumped is that the ion diameters of erbium (~0.206 nm) and ytterbium (~0.232 nm) are similar and have a tendency to form erbium-ytterbium ion clusters. This is one of the reasons why energy can be effectively transferred from the ytterbium to erbium in a 9xx nm pumped EYDF. Since the ion concentration of ytterbium ions is much more than erbium ions, the erbium-ytterbium ion cluster is probably formed between one erbium ion and several ytterbium ions. In the 9xx nm pumped EYDF, the energy transfer between erbium in the $^4I_{11/2}$ level and ytterbium in the $^2F_{7/2}$ level can be efficient due to the similar energy gap between the $^4I_{11/2}$ and $^4I_{15/2}$ levels of erbium and the $^2F_{5/2}$ and $^2F_{7/2}$ levels of ytterbium. However, when the erbium ion of the erbium-ytterbium ion cluster is excited to the $^4I_{13/2}$ level through in-band pumping, the energy of the erbium ion cannot be transferred to the neighbouring ytterbium ions due to energy gap between the $^4I_{11/2}$ and $^4I_{13/2}$ levels of erbium ion (6500 cm^{-1}) as illustrated in Figure 4-10. Furthermore, the ytterbium ions not only do not accept energy from the $^4I_{13/2}$ level erbium ion, but also serve to isolate the erbium ions within different erbium-ytterbium ion clusters from each other. Hence, the ytterbium codopant inhibits the energy transfer as well as the pair induced quenching when this "SPI" fibre is in-band pumped [58].

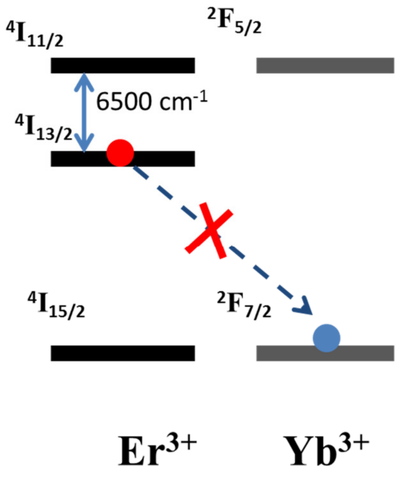

Figure 4-10 The energy gap between $^4I_{11/2}$ and $^4I_{13/2}$ of erbium manifolds (6500 cm^{-1}) prevents the energy transfer from the $^4I_{13/2}$ level Er^{3+} ion to the $^2F_{7/2}$ level Yb^{3+} ion.

The above hypothesis was first shown by K. Aiso et al. [59] to suppress the PIQ in an alumina-germano-silicate EYDF. The authors measured the power dependence of the $^4I_{13/2}$-lifetime of EDFs with and without ytterbium codoping. It was found that, without the ytterbium doping, the $^4I_{13/2}$-lifetime of the EDF decreases when the pump power increases at an erbium concentration of 1000 ppm by weight. The decrease of life time indicates the occurrence of PIQ. In contrast, the EDF codoped with ytterbium exhibits a $^4I_{13/2}$-lifetime that is independent of pump power even with an erbium concentration of 2000 ppm by weight. This ion concentration corresponds to an absorption of 22.7 dB/m at 1530 nm. After that, the EYDF fibre was used to demonstrate a 76% power conversion efficiency (PCE) with an output power of 350 mW using 1490 nm pump laser diodes. The 76% PCE reported is rather high in comparison with the 68% PCE demonstrated with an EDF that exhibits a a similar absorption of 21 dB/m at 1530 nm [60]. This comparison indicates that co-doping the EDF with ytterbium may inhibit the PIQ. Furthermore, it is interesting to note that no phosphorous is codoped in the EYDF fibre in [59], which is in contrast to the phosphosilicate-based EYDF designed for 9xx nm pumping [21]. This suggests that phosphorous may not be essential for the suppression of pair induced quenching on in their experiment. In fact, the study by E. Delavaque et. al. also indicates that the suppression of PIQ with phosphorous is less effective than with aluminium [43]. Hence, the low pair ion ratio in the SPI fibre is likely due to the formation of erbium-ytterbium clusters that mitigate the pair induced quenching and the phosphorous doping plays a minor role. Recently, ytterbium has also been codoped as a concentration quenching inhibitor to demonstrate 103 W with 76% conversion efficiency in a fibre with ~74 dB/m small signal absorption at 1535 nm [61]. Therefore, co-doping of ytterbium in EDF for the in-band pumped EDFA is a promising approach to reduce the detrimental effect of PIQ and to achieve high PCE.

4.2 State of the arts

Table 4 lists the recent progress in the high average power erbium doped fibre lasers and amplifiers and the corresponding experimental parameters. To achieve high average power, a fundamental requirement is clearly that sufficient pump power must first be absorbed by the active fibre over a reasonably short length scale in order to generate high signal output power. However, the absorption coefficient of the Er^{3+} ion at the peak absorption wavelength of ~ 980 nm is rather low compared to the absorption coefficient of the Yb^{3+} (as shown in Figure 2-15). To circumvent this, erbium doped fibre (EDF) has been co-doped with ytterbium (Yb) ions to increase the pump absorption. The absorbed pump energy is then resonantly transferred from the Yb^{3+} to the Er^{3+} ions with high efficiency. Using this approach, average output powers as high as 297 W have been demonstrated in the year 2007 [5]. However, under high power operations, this pumping scheme is prone to spurious lasing of the Yb^{3+} ions at wavelengths around 1.06 μm which results in a decrease in conversion efficiency at higher power levels from 40% to 19%. Furthermore, the relatively large quantum defect results in a high thermal load per unit length which further limits the prospect for substantial power scaling.

To improve the conversion efficiency significantly an in-band pump approach can be employed, (also known either as resonant or tandem-pumping), theoretically enabling quantum defects of less than 5%. To date the best conversion efficiency reported (output power/absorbed pump power) is 84.3% obtained in a pure erbium-doped fibre operated in a core pumped configuration at low average powers of up to just 0.35 W [62]. The gain fibre used in this instance was engineered to have low Er^{3+} ion clustering and the core composition carefully optimised to provide a high pump to signal conversion efficiency with a core absorption of ~ 9 dB/m at 1530 nm. Similarly, 101 W with a conversion efficiency of 71% has also been generated by core pumping a pure erbium doped fibre with a core absorption of ~ 6 dB/m at 1530 nm [63]. In these two experiments, the core absorption of the fibre is far too low to allow the same fibre core composition to be realistically used for simple power scaling via direct diode based cladding pumping since the pump absorption would be reduced to impractical levels by the low core to inner cladding area ratio. Therefore, the core pumping scheme is viable only if a high power high brightness pump source is available.

To increase the absorption would necessitate a higher Er-concentration. However, as the Er^{3+} ion concentration is increased the concentration quenching effect rapidly starts to become significant (see Section 4.1.2), resulting in lower optical-to-optical conversion efficiencies.

So far the record value of conversion efficiency in the multi-Watt regime for a cladding pumped pure erbium doped fibre laser is ~ 69% with 88 W average power [64]. It is important to note that this laser was pumped directly using a high power InGaAs/InP laser diode module which is highly desirable from a practical perspective. The sub-quantum limit conversion efficiency can be attributed to the concentration quenching and can only be improved through improvement in glass composition [65, 66]. However, by codoping the Yb-ions as a concentration quenching inhibitor, I demonstrated 80% power conversion efficiency (18 W output power) in a core pumping scheme. Similarly, a separate group also demonstrated 74% conversion efficiency (103 W output power) [61] conversion efficiency in a cladding pumping scheme with a ytterbium codoped EDF.

Table 4 Recent progress in high average power erbium doped fibre lasers and amplifiers

Year	Fibre	Pump wavelength	Scheme	Power (W)	η_L or η_A (%)[1]	Absorption (dB/m)[2]	$d_{core}/d_{cladding}$ (μm)	NA	Ref.
2007	Er/Yb	975	CLS	279	$\eta_L \approx 19$-40[3]	54	30/600	0.21	[5]
2008	Er/Yb	1535	CLS	10	$\eta_A \approx 34$	-[4]	12/160	-[4]	[67]
2008	Er	1535	CRS	9.3	$\eta_A \approx 50$	60	20/125	0.08	[68]
2009	Er	1535	CLS	48	$\eta_A \approx 56.7$	60	20/125	0.08	[69]
2009	Er	1476	CRS	0.35	$\eta_L \approx 84.3$	9	7/125	0.20	[62]
2011	Er	976	CLS	67	$\eta_A \approx 30$	60	40/140	0.08	[3]
2011	Er	1530	CLS	88	$\eta_A \approx 69$	60	20/125	0.08	[64]
2011	Er/Yb	1535	CRS	18	$\eta_L \approx 80$	71.2	12/160	0.22	[70]
2012	Er	1480	CRS	101	$\eta_L \approx 71$	6	3/125[5]	0.23	[63]
2012	Er	976	CLS	7.5	$\eta_A \approx 40$	83	22/95	0.06[5]	[66]
2012	Er/Yb	1535	CLS	103	$\eta_L \approx 76$	73.7	17/125	0.08	[61]

Note 1: η_L and η_A are the output efficiency with respect to the launched and absorbed pump power respectively as given in the original reference.

Note 2: This is the small signal core absorption at 1530 nm. When the cladding absorption is given in the original reference, it is converted into core absorption using the area ratio. When the absorption is given at slightly different wavelength, it is converted to 1530 nm using the absorption cross section in [22].

Note 3: The efficiency before Yb-colasing in the absence and presence Yb-colasing parameter are 40% and 19% respectively. The Yb-colasing is required for the stable operation of laser.

Note 4: The parameter is not available in the reference.

Note 5: The core diameter is estimated from the cut off wavelength.

4.3 Characteristics of the pump source

The in-band pump source in this work is a 1535 nm fibre laser with a maximum output power of 24 W and FWHM of 0.25 nm, as shown in Figure 4-11. It consists of an Er/Yb co-doped GT-wave fibre and a pair of fibre Bragg gratings (FBGs), which were used to define the laser emission wavelength. The maximum output power of 24 W was achieved using a 4.5 m GTwave fibre with a launched pump power of ~60 W, i.e., the conversion efficiency was ~40%. The output spectra of the laser at various output powers are shown in Figure 4-12. At an output power of 3.56 W, the ratio of the 1535 nm laser output to the unwanted patristic lasing (around 1550 nm) is ~38 dB. As the output power was increased, the 1535 nm lasing peak increased while the noise level around 1550 nm remained almost the same. At the maximum output of 24 W, 1535 nm lasing peak was about 50 dB higher than the noise level. The photo of the experiment setup was shown in Figure 4-13.

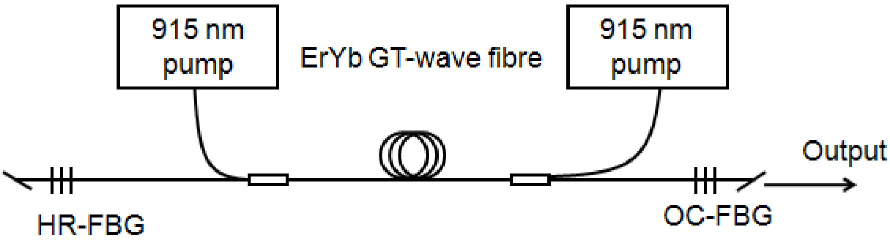

Figure 4-11 Setup configuration of the in-band pump source. HR-FBG: high-reflectivity FBG, OC-FBG: output coupling FBG.

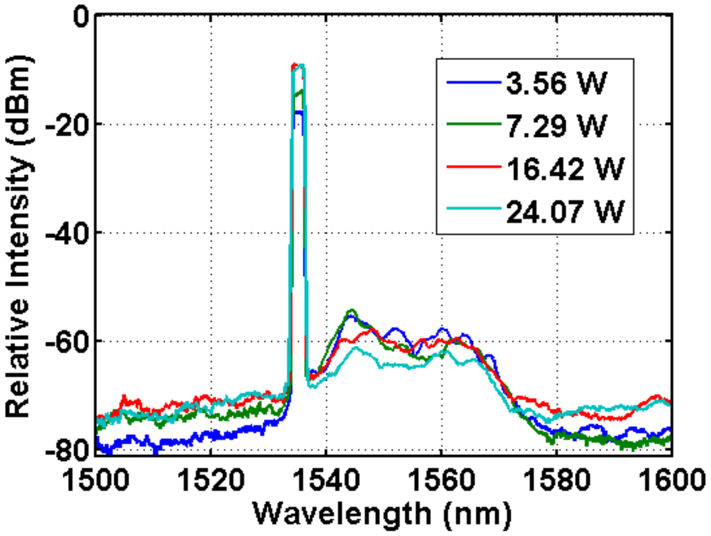

Figure 4-12 Spectral plots of the 1535 nm pump laser at various output powers.

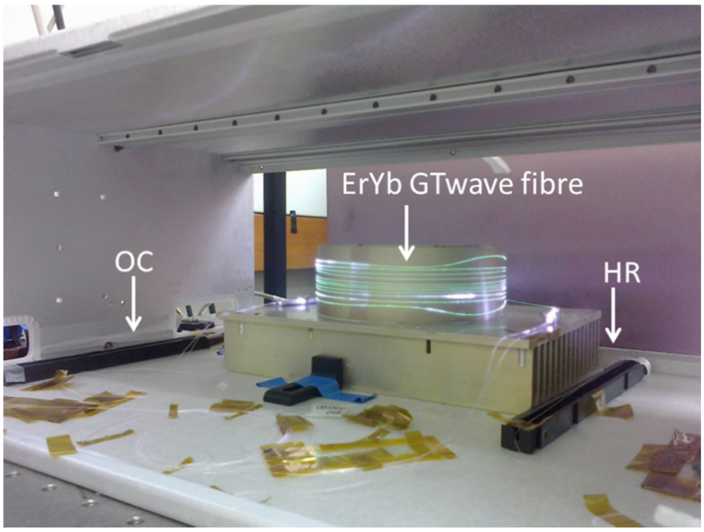

Figure 4-13 The experimental setup for the 1535 nm pump fibre laser. The green fluorescence is due to the the upconversion of erbium ions while the violet fluorescence is due to the of 915 nm radiation induced fluorescence in camera.

4.4 Core-pumped MOPA

4.4.1 Experiment setup

Figure 4-14 shows the experimental setup of a FP-CRS master oscillator power amplifier (MOPA) system. The seed is an external cavity tuneable laser (Agilent 8164A) delivering 1 mW of average output power in the C-band. A commercial high power amplifier (IPG-EAD-5-K-C) is used to boost the seed power. The pump source is a fibre Bragg grating (FBG) stabilised 1535 nm single mode fibre laser (see Section 4.3). The signal and pump beams are combined and launched into the core of the gain fibre via a wavelength division multiplexer (WDM). I have investigated two different active fibres, namely Fibre 1 and Fibre 2.

Fibre 1 is an in-house made EYDF with an estimated mode field diameter (MFD) of 12 µm (fundamental mode) and a core numerical aperture (NA) of 0.22. The measured core absorption is ~ 58 dB/m at 1535 nm. With the core absorption, I estimate the optimal fibre length for the CRS experiment in the absence of concentration quenching as ~ 3.5 m. Hence, a 3.75 m fibre was used. Fibre 2 is a commercial pure erbium doped double clad fibre (Liekki Er 60-40/140DC) with a 40 µm core diameter with a corresponding NA of 0.10, a cladding diameter of 140 µm with a corresponding NA of 0.46. The core absorption is 60 dB/m at 1530 nm. Based on the core absorption, I estimated the optimal length as ~ 3 m prior to the purchase of the fibre. In the absence of concentration quenching, the output power is not strongly dependent on optimal fibre length (see the discussion relating to Figure 4-16 in Section 4.4.2). Hence, I opted to purchase 5 m of the fibre for use in my experiments. The fibre length was reduced by ~ 0.1 m as a result of preliminary splicing trials. Hence, the actual length of Fibre 2 used in my experiments was ~ 4.9 m.

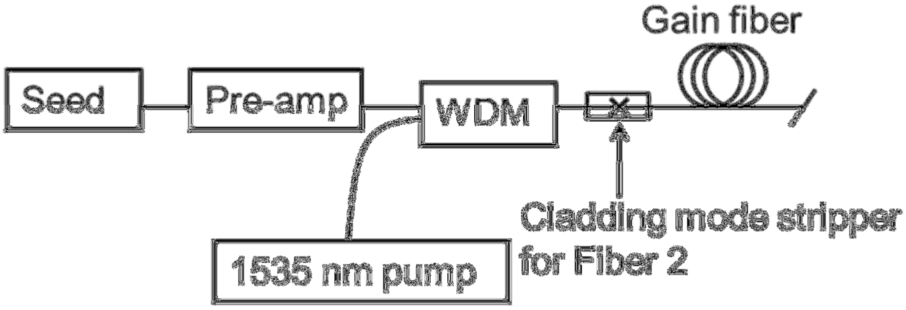

Figure 4-14 Experimental setup of the FP-CRS configuration. Cladding mode stripper was used only for Fibre 2.

The performance of Fibre 1 was first investigated at a signal wavelength of 1565 nm for input signal power levels of 62.5 mW, 250 mW and 1000 mW as shown in Figure 4-15(a) with circles. The results show that a high input signal level is needed to achieve a high PCE (PCE= (output signal power-input signal power)/absorbed pump power). The optimal wavelength of operation of the final stage amplifier was determined to be ~1562.5 nm. For an input signal power of 1.5 W at 1562.5 nm, the MOPA output increased linearly with increasing 1535 nm input pump power. A maximum output power of 18.45 W was measured for 21.38 W of input pump power, corresponding to a PCE of ~ 80%. The absence of roll-off of the signal output power at the maximum available pump power signifies that the maximum signal output power is pump-power limited. The output spectrum at maximum power (inset in Figure 4-15(a)) shows a good Optical to Signal Noise Ratio (OSNR) and negligible residual pump power. Overall, the performance of Fibre 1 agrees with my initial estimation.

The performance of Fibre 2 was tested in a similar manner. Since this was a double-clad fibre, a cladding mode stripper was used at the splice point between the WDM and Fibre 2 (as shown in Figure 4-14) to ensure that any optical power leaking into the cladding was cleanly and safely removed from the system so as to minimize any measurement uncertainties at the amplifier output. The measured splice loss between the two quite dissimilar fibres was ~ 2 dB. As a result only 60% of the available pump and signal power was coupled into the fibre core. The performance of the fibre was tested at a signal wavelength of 1565 nm for input signal-power levels of 24 mW, 70 mW, 140 mW, 282 mW and 563 mW as shown in Figure 4-15(b) (circles). The maximum signal output power was measured to be ~ 1.93 W at 0.563 W of input signal power and 7.05 W input pump power, which corresponded to a maximum PCE of ~ 19.4%. It should be mentioned that no residual pump was measurable in the experiment. This experiment result differs significantly from my initial estimation, and motivates us to investigate the impact of concentration quenching to the performance of the high power erbium doped fibre amplifier (EDFA).

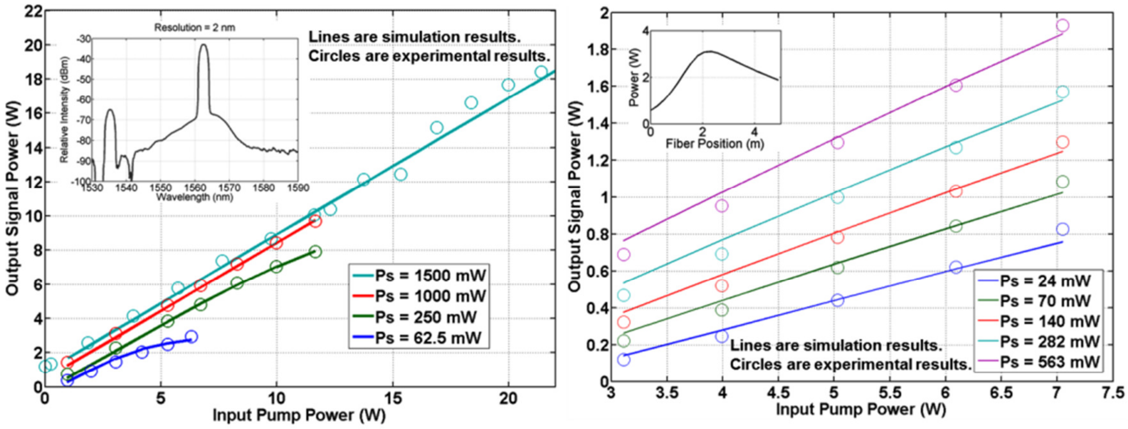

(a) (b)

Figure 4-15 Experimental (circles) and simulation (lines) results for (a) Fibre 1 and (b) Fibre 2. The inset in (a) is the output spectrum of Fibre 1 at the maximum output signal power. The inset in (b) is the simulated signal power distribution along Fibre 2 for the case of 563 mW input signal power and 7.05 W input pump power.

4.4.2 Fitting results

Although Fibre 1 is an Er/Yb co-doped fibre, the Yb^{3+} ions do not play any active role in the amplification process since Yb^{3+} ion does not exhibit emission and absorption in 1.5-1.6 µm spectral range. Therefore, the Yb^{3+} ions can be neglected in the simulation. In the fitting process, the following parameters are either known or estimated: length of the EYDF = 3.75 m, core absorption = 58 dB/m at 1535 nm, core diameter =14 µm, the Er-doping diameter = 8.9 µm and concentration of Er^{3+} ion = 2.45×10^{25} /m^3. The following parameters are obtained from literature: m = 1×10^4 [48], $^4I_{13/2}$ fluorescence lifetime of Er^{3+} ion = 10 ms [22] and the emission and absorption cross sections from [71]. The values of C and k are obtained as fitting parameters. The behaviour of the amplifier can be best-fitted with $C = 2.0\times10^{-22}$ m^3/s and $k = 0.2\%$ (shown by the lines in Figure 4-15(a)). Similarly for Fibre 2, the following parameters are known or estimated: fibre length = 4.9 m, core absorption = 60 dB/m at 1530 nm, Er-doping diameter = 40 µm, core diameter = 40 µm, concentration of Er^{3+} ion = 3.23×10^{25} /m^3. The $^4I_{13/2}$ fluorescence lifetime of Er^{3+} ion = 10 ms and the absorption/emission cross section from [22]. With k as the fitting parameter and $C = 0$, a good fit is achieved with $k = 4.1\%$ (shown by the lines in Figure 4-15(b)). The inset in Figure 4-15(b) shows the simulated signal distribution along the fibre for 563 mW input signal and 7.05 W input pump power. Based on the simulation results, I predict that a maximum signal power of ~ 3.1 W could be achieved if ~ 2.3 m of active fibre were to be used, corresponding to an estimated PCE of ~ 37%. Hence, even using an optimum fibre length, the PCE is still far from the quantum limit due to the presence of PIQ. I did not cut back my sole sample of Fibre 2 to validate this prediction since it was needed for other experiments, for example the experiment described in Section 4.5.2 and Chapter 5.

The lower k-value of Fibre 1 compared to Fibre 2 may be due to the lower Er^{3+} ion concentration of Fibre 1, the high solubility of Er^{3+} ion in the EYDF phosphosilicate-glass host and/or the presence of Yb^{3+} ions in the EYDF (see Section 4.1.3). Meanwhile, for a pure Er-doped fibre, the k-value of Fibre 2 is reasonable compared to those reported in [42]. This low k-value can be attributed to the direct nanoparticle deposition (DND) technologies used in the fibre fabrication process [57]. To further illustrate the detrimental effect of PIQ, the signal distribution along the fibre for a 0.5 W input signal power at 1565 nm and 20 W of input pump power is simulated for 5 different *k*-values in the forward core pumping configuration as shown in Figure 4-16 (all the simulations are based on the parameters of Fibre 2, unless specified otherwise). The result shows that an increase in *k*-value from 0.0% to 1.1% decreases the PCE from ~ 93% to ~ 67%, while it drops down to ~ 30% when the *k*-value increases to 4.1%. After the optimal fibre length (~ 3.5 - 4.0 m), the signal power with a higher *k*-value decreases more rapidly. This increase of signal reabsorption is caused by the PIQ. Hence, a stronger PIQ causes the output signal power to be far more sensitive to the optimal choice of fibre length.

These results signify the importance of minimizing PIQ in high power CRS-EDFAs. I have demonstrated better than 80% PCE from an EDF with low PIQ and further enhancement in PCE may be possible by eliminating the PIQ completely.

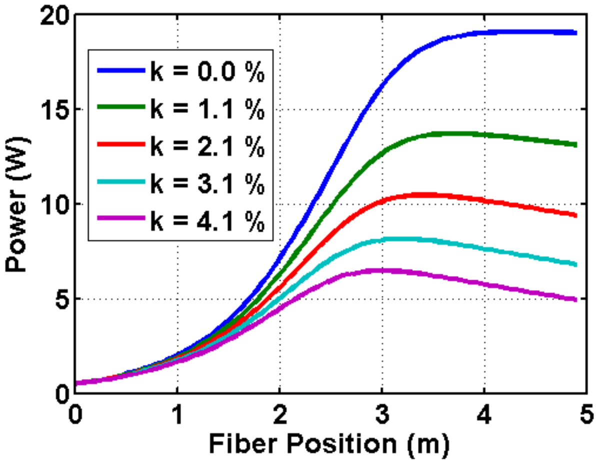

Figure 4-16 Simulated signal power distribution along the gain fibre for 5 different k-values with 0.5 W 1565 nm input signal power and 20 W input pump power in FP-CRS configuration.

4.5 Power scaling of in-band pumped EDF

4.5.1 Simulation

Although I have achieved 18 W of output power with a record PCE, power scaling in this scheme will ultimately be limited by the availability of high power single mode pump sources at 1535 nm as well as passive optical components e.g., WDM couplers capable of handling such high average power. Moreover, the optical-to-optical efficiency from diode to laser output is only ~ 32%. To improve the efficiency figure and to avoid the potential power scaling bottleneck presented by the need for an intermediary fibre pump laser, direct cladding pumping using InGaAs/InP-laser diodes will be the preferred solution [64].

To assess the performance and to identify the optimum pump configuration for power scaling of in-band pumped EDF MOPAs, and to investigate the impact of PIQ in this instance, I have modelled such systems for different pumping arrangements using the parameters of Fibre 2 but choosing the *k*-value to be either *k* = 0.2% (as for Fibre 1) or 4.1% (as for Fibre 2). In this work, I have simulated the fibre amplifier in continuous wave operation using the software developed by the company Optiwave known as Optisystem.

For ease of discussion, I label the various pumping schemes with the following notation "signal wavelength-pumping direction-pump coupling mechanism". For example, the notation "1565 nm-FP-CRS" represents the pumping condition where the 1565 nm signal is amplified using a forward-propagating (FP) core-pumped amplifier (CRS). The input signal and pump powers are assumed to be 1 W and 100 W respectively. The signal wavelengths of 1565 nm and 1605 nm are studied, as each of them represents the optimal wavelength for CRS and CLS respectively. In the case of CLS, the overlap factor at the pump wavelength is reduced by a factor given by the ratio between the core to the inner cladding area.

In the case of CRS, a fibre length of 4.4 m was chosen since this represents the length at which the maximum output power is achieved for a 1565 nm-BP-CRS system with k = 4.1%. With this length, the pump absorption at 1535 nm was estimated to be > 18 dB in the case of a 1565 nm signal. In the case of CLS, an active fibre length of 15.0 m was chosen since this represents the length where the maximum output power can be achieved for a 1605 nm-BP-CLS with k = 4.1%. With this length, the pump absorptions are > 14 dB in the case of 1565 nm signal and > 21 dB in the case of 1605 nm signal. The difference in the pump absorption is due to the difference in the signal saturation power, P_{sat}, which is inversely proportional to ($\sigma_e + \sigma_a$), where σ_e and σ_a are the emission and the absorption cross sections at the signal wavelength respectively. The lower P_{sat} at 1565 nm leads to reabsorption of the signal and increases the inversion level of the gain medium. Therefore, the pump absorption in the presence of the 1565 nm signal is lower than is the case of a 1605 nm signal. Overall, most of the pump power has been absorbed in all cases. Furthermore, a slight variation of fibre length (± 0.1 m) does not change the simulation results significantly.

The results for FP are presented in Figure 4-17(a). When k = 0.2% (similar to the case for Fibre 1), the maximum signal powers, P_{max}, for 1565 nm-FP-CRS (blue solid line), 1565 nm-FP-CLS (green solid line) and 1605 nm-FP-CLS (red solid line) pumping schemes are 89.7 W, 85.5 W and 91.5 W respectively. The maximum signal powers for various cases are also tabulated in Table 5. When the k-value increases to 4.1% (as for Fibre 2), P_{max} for 1565 nm-FP-CRS (blue dash line), 1565 nm-FP-CLS (green dash line) and 1605 nm-FP-CLS (red dash line) are 26.1 W, 34.9 W and 63.1 W respectively. (Note that the location of the P_{max} is different for the various configurations. For example, with k = 4.1%, the P_{max} occurs at 8 m for 1565 nm-FP-CLS and 12.2 m for 1605 nm-FP-CLS.) Therefore as the k-factor increases from 0.2% to 4.1%, the P_{max} is reduced by 70.95%, 59.20% and 31.03% for 1565 nm-FP-CRS, 1565 nm-FP-CLS and 1605 nm-FP-CLS pumping schemes respectively. By comparing the reduction of 1565 nm-FP-CRS and 1565 nm-FP-CLS, we see that the effect of PIQ is less severe in the case of CLS. The advantage of CLS is even more obvious comparing the 1605 nm-FP-CLS case with the 1565 nm-FP-CRS case. In the CLS, the lower pump intensity reduces the detrimental effect of PIQ. Furthermore, since the ground state absorption at 1605 nm is lower, the 1605 nm signal is less likely to suffer from PIQ compared to the 1565 nm signal. These results clearly highlight that the CLS is far less susceptible to the detrimental effects of PIQ compared to the CRS. The simulation also indicates that with 1605 nm-FP-CLS and k = 4.1%, the PCE can be of the order of 64%, which is comparable to the 69% reported in [64], where a similar fibre was used in a forward-pumped laser oscillator.

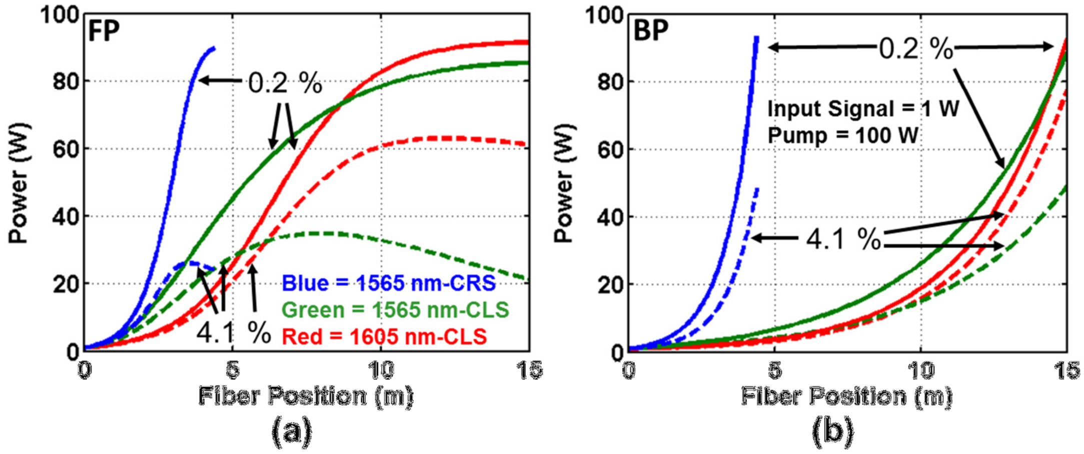

Figure 4-17 Signal distribution at two different k-values (0.2% (solid lines) and 4.1% (dashed lines) under (a) forward-pumping scheme (FP) and (b) backward-pumping scheme (BP). Blue lines are 1565 nm-CRS, green-lines are 1565 nm-CLS and red lines are 1605 nm-CLS. The input signal power is 1 W and the input pump is 100 W.

Figure 4-17(b) shows the simulation results for the BP condition. In this case, the reductions in P_{max} as the *k*-value increases from 0.2% to 4.1% are 51.07% (93.6 W to 45.8 W), 43.68% (88.7 W to 50.0 W) and 16.34% (92.6 W to 77.5 W) for the 1565 nm-BP-CRS (blue lines), 1565 nm-BP-CLS (green lines) and 1605 nm-BP-CLS (red lines) pumping schemes respectively. Similar to the FP scheme, the reduction in efficiency due to PIQ for the CRS is more than that of the CLS. Furthermore, by comparing the P_{max}-reduction for FP and BP for the same pump-coupling architecture and the same signal-wavelength (e.g., the reduction for 1565 nm-FP-CRS is 70.95% and for 1565 nm-BP-CRS is 51.07%), I conclude that the BP is less susceptible to the detrimental effects of PIQ compared to the FP. The physical reason for this is that in the case of BP, the backward propagating pump is strongest in the region where the signal is strongest. Thus, the inversion can be most efficiently depleted by the signal thereby reducing the peak local inversion within the fibre and thereby reducing the efficiency and net effect of the PIQ. Hence, the detrimental effect of the PIQ is mitigated. In terms of PCE, my simulation predicts that, with 1605 nm-BP-CLS and *k* = 4.1%, ~ 77% PCE with high output power is feasible with the current commercially available fibre. A PCE of better than 90% should be possible if the *k*-value can be brought down to the level that I have achieved with the in-house fabricated fibre. The key results for the various schemes are summarised in Table 5.

To check the scalability of the simulation results, I repeated the simulation at much-higher pump powers (up to 10 kW) while keeping the input pump to signal ratio constant (i.e., at 100). The results show that the PCE and the signal gain are similar at higher pump powers and therefore indicate that the analysis for the different pump conditions is scalable to lasers with kW class output power.

Table 5 Summary of key results for various schemes for 1 W input signal and 100 W input pump

Scheme	$k = 0.2\%$		$k = 4.1\%$		P_{max}-reduction when k-value increases from 0.2 to 4.1% (%)
	P_{max} (W)	PCE (%)	P_{max} (W)	PCE (%)	
1565 nm-FP-CRS	89.7	90	26.1	25	70.95
1565 nm-FP-CLS	85.5	88	34.9	44	59.20
1605 nm-FP-CLS	91.5	91	63.1	64	31.03
1565 nm-BP-CRS	93.6	94	45.8	45	51.07
1565 nm-BP-CLS	88.7	91	50.0	51	43.68
1605 nm-BP-CLS	92.6	92	77.5	77	16.34

4.5.2 Experimental validation: cladding pump case

To support the outcome of my numerical modelling, I performed a cladding pumped experiment with Fibre 2. The experimental setup was very similar to that for the core-pumped scheme shown in Figure 4-14 other than that a tapered fibre bundle (TFB) was used to combine the pump and signal beams instead of a single mode WDM coupler. The 1535 nm single mode pump laser was spliced to the signal port of the TFB to explore the cladding pumping option. A commercial L-band high power amplifier (Keopsys CEFA-L-PB-HP) was used to boost the seed laser power into the final amplifier at both 1565 nm and 1605 nm.

The output powers with respect to the absorbed pump powers at the two signal wavelengths are shown in Figure 4-18. In both cases 0.61 W of signal input power was coupled into the final amplifier. For ~ 11.5 W of absorbed pump, the output signal power was measured to be ~ 6.0 W for the 1605 nm case and ~ 4.6 W for the 1565 nm case. The corresponding PCEs are ~ 47% and ~ 38% for signal wavelengths of 1605 nm and 1565 nm respectively. These values are significantly lower than predicted by my theory. Finally, I did not perform the backward pumping experiment because it was not possible to buy a dichroic mirror that can separate the 1535 nm and 1565 nm wavelength.

In trying to establish the reason for these relatively low measured PCEs I first characterised the pump absorption within the fibre. Using a passive version of Fibre 2 (Liekki Passive-40/140 DC) I measured the background loss of the cladding guided pump light to be ~0.15 dB/m at 1535 nm – a surprisingly large number. When this background loss is introduced into the simulation model, I obtained a very good fit (lines in Figure 4-18) to the experimental results. This simple experiment clearly supports the prediction that the cladding pumping scheme in conjunction with a longer signal wavelength can mitigate the detrimental effects of concentration quenching and increase the PCE. In order to realise the predicted ~ 77% PCE and to achieve high power without damage concerns will require use of a different low-index polymer coating (the current coatings being suitable and optimised for diode pumping at shorter wavelengths). Furthermore, I did not perform the backward pumping experiment because I did not manage to find a supplier that could supply a dichroic mirror to separate the spectrally close 1535 nm pump and 1565 nm signal wavelength.

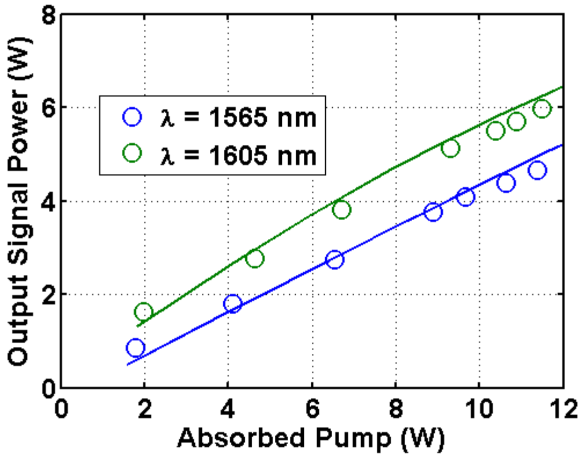

Figure 4-18 The simulated (solid lines) and the experimental (circles) output signal power with respect to the absorbed pump power for the cladding pumped MOPA with input signals of 0.61 W at 1565 nm and 1605 nm

4.6 Conclusion

In conclusion, a highly efficient (~ 80%), high power (18.45 W) in-band core pumped, all-fibre EYDF MOPA is demonstrated. To the best of my knowledge, this represents the highest power conversion efficiency achieved from a "multi-watt" fibre amplifier at 1.5 µm. I have identified through the fitting of the experimental results that concentration quenching can represent a major limiting factor in achieving highly efficient, high power, in-band pumped EDFAs. Furthermore, I believe that the high efficiency demonstrated with my in-band pumped EYDF fibre is due to the formation of erbium-ytterbium ion cluster that inhibits the pair induced quenching. Through the use of numerical modelling, I have concluded that a backward, in-band cladding pumping with a signal wavelength at ~ 1605 nm should be employed not only to scale up the output power to the kW regime but also to mitigate the effect of concentration quenching. I have also validated my simulation results with a simple cladding pumped experiment. Based on my simulations and experiments, I predict that a ~ 77% power conversion efficiency with high output power is feasible providing the background loss suffered by the cladding guided 1535 nm pump can be reduced. This should open up the possibility for kW-class fibre lasers at 1.55 µm once high-brightness multimode pumps at 153x nm become commercially available.

Chapter 5 High energy in-band pumped fibre amplifiers

Eye safe, high energy erbium based 1.55 μm pulsed sources are highly desirable for many practical applications such as remote sensing where light scattering from targets gives rise to eye-safety concerns. Furthermore, due to the availability of telecom grade components, the system functionality and cost of 1.55 μm pulsed fibre lasers is expected, in the short term at least, to be more attractive than thulium based 1.90 μm eye-safe pulsed variants.

The two main figures of merit for such laser sources are the pulse energy and beam quality. In terms of pulse energy, up to 17 mJ (M^2~13-16) has been reported using erbium doped fibre (EDF) with 100 μm core diameter [72], although as of yet very few published details are provided in relation to this experiment. The next highest reported pulse energy is 1.4 mJ (1.1 ns, M^2~8.5) generated from an erbium doped fibre amplifier pumped by a 980 nm [73] multimode laser bar. In terms of best output beam quality, an M^2 of 1.65 had been reported for a pulse energy of 1.15 mJ pulse and a pulse width of 575 ns [7]. However, due to the uncontrolled multiple-peak phenomenon (MPP) in the Q-switched seed [74], the output pulse exhibited significant temporal substructure. This kind of pulse shape is highly undesirable for many applications.

Recently, in-band pumped (also known as resonantly-pumped or tandem-pumped) erbium doped fibre amplifiers (IP-EDFAs) have attracted considerable interest as a potential approach to address the low-efficiency commonly found in 980 nm pumped EDFAs and 9xx nm pumped Er/Yb co-doped fibre (EYDF) amplifiers. In particular, optical-to-optical conversion efficiencies of ~69% and ~80% have been demonstrated in cladding- and core-pumped implementations respectively [64, 74]. However, it has been found that the conversion efficiency can be impaired by concentration quenching effects in higher erbium concentration fibres (see Chapter 4). The use of a core pumping scheme (CRS) is particularly attractive for pulsed amplifiers since it allows for lower doping concentrations (which helps reduce concentration quenching effects) and also provides for shorter pump absorption lengths - resulting in an inherently shorter device and thus reduced effective nonlinear lengths [75].

The IP-EDFA is also attractive as a pulse amplifier for high pulse energy extraction. In such systems, the maximum extractable energy is typically limited by the maximum stored energy of the active fibre before self-saturation by amplified spontaneous emission (ASE), or spurious lasing set in. The extent of ASE build-up depends on the level of backscattered light due to reflection at the fibre facets as well as Rayleigh back-scattering (RBS). While the fibre facet reflection can be managed by the use of an end-cap, the RBS can only be reduced by using a doped fibre with a lower core numerical aperture (NA) since the fraction of RBS captured back into the guided mode is proportional to NA^2 [76]. A typical ytterbium-sensitised EDF has ~0.22 core NA, due to the phosphorous-doping required for efficient pump energy transfer. In comparison, the IP-EDFA permits the use of pure erbium doped fibre, where an NA as low as ~0.066 has been demonstrated in an index guided fibre [77] or <0.04 in a photonic crystal fibre [3]. Therefore, the pure-erbium doped fibre can potentially reduce RBS by >14 dB, i.e., $(0.22/0.04)^2 \approx 30.25$, compared to EYDF-based systems. Meanwhile, the absence of ytterbium in pure erbium doped fibre completely eliminates the possibility of ytterbium co-lasing [5], which can be difficult to manage, especially in a low repetition rate EYDF system. The use of low NA fibre also reduces the number of guided modes and improves the output beam quality for a given core diameter.

This chapter describes my work on high energy in-band pumped fibre amplifiers. Section 5.1 describes the analytical and numerical models to understand the behaviour of pulse amplifier. Section 5.2 presents the state of the arts in this area. In Section 5.3 and 5.4, I investigate through experiment the characteristics of high energy, IP-EDFAs operating at 1562.5 nm for both core pumping scheme (CRS) and cladding pumping scheme (CLS) based, fully-fibrised, master oscillator power amplifier (MOPA) configurations. Section 5.5 presents the numerical model used to help identify and understand the mechanism that leads to the saturation of pulse energy observed in my experiments.

5.1 Background

5.1.1 Pulse amplification and energy extraction

Consider an optical pulse with intensity $I(z,t)$ travels through a laser medium with population inversion $\Delta N(z,t)$ (see Figure 5-1). The $I(z,t)$ can be related to the electromagnetic energy density, ρ_{em} (J/m^3), through $I(z,t) = \rho_{em} v_g$, where v_g is the group velocity inside the laser medium. In the short segment Δz, the rate of change of stored energy can be expressed as:

$$\begin{aligned}&\text{The rate of change of stored energy in } \Delta z \\ &\qquad = \text{energy flux into } \Delta z - \text{energy flux out from } \Delta z \\ &\qquad + \text{net rate of stimulated emission within } \Delta z.\end{aligned}$$

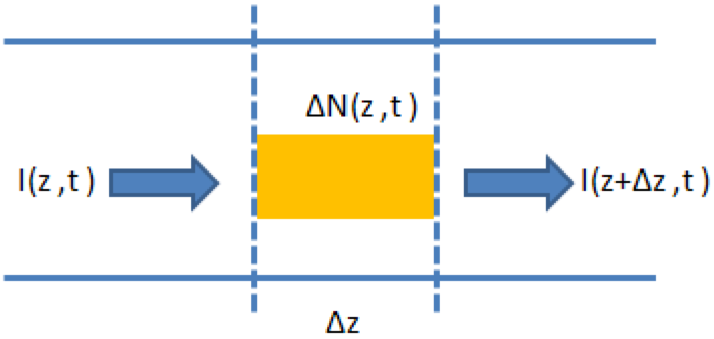

Figure 5-1 Optical signal passing through a short segment of an amplifier.

Mathematically, the statement can expressed as [31]:

$$\frac{\partial}{\partial t}[\rho_{em}\Delta z] = I(z,t) - I(z+\Delta z) + \sigma \Delta N I(z,t)\Delta z\,. \tag{5-1}$$

Using $I(z,t) = \rho_{em} v_g$, the amplification of the pulse in the laser medium can be described by

$$\frac{\partial I(z,t)}{\partial t} + v_g \frac{\partial I(z,t)}{\partial z} = \sigma_e v_g \Delta N(z,t) I(z,t), \tag{5-2}$$

and using the rate equations, i.e., Eqs. (2-57) and (2-58):

$$\frac{\partial \Delta N(z,t)}{\partial t} = \sigma_e \frac{I(z,t)}{h\nu} \Delta N(z,t), \tag{5-3}$$

where v_g is the group velocity of the pulse and ν is the frequency of the signal light. Eqs. (5-2) and (5-3) describe the spatiotemporal behaviour of the pulse as it undergoes amplification in the laser medium. These equations are further-developed in Section 3.2.2 for the case of a three-level laser system into travelling wave rate equations, i.e., Eqs. (3-4) to (3-7).

The maximum energy that can be extracted is intrinsically related to the energy stored in the laser gain medium. An important parameter that characterises the energy storage in a laser medium is the saturation energy E_{sat} [31]:

$$E_{sat} = \frac{h\nu A_{core}}{(\sigma_e + \sigma_a)\Gamma_s}, \tag{5-4}$$

where $h\nu$ is the energy of the signal photon, σ_e and σ_a are the emission and absorption cross-sections at the signal wavelength, A_{core} is the doped core area and Γ_s is the signal overlap with the doped area. The physical interpretation of the saturation energy is that if a signal with energy E_{sat} impinges on an ion in a time much less than the fluorescence life time of the active ion, the ion has essentially a 50% chance of making a stimulated transition from one level to the other during the time of travel of the pulse [31].

Typically, the extractable energy in a fibre is limited to around 10 times the saturation energy. Above that, any additional pump power used to create population inversion is simply lost in the form of amplified spontaneous emission (ASE), without significantly increasing the stored energy [78]. The factor $(\sigma_e + \sigma_a)$ in Eq. (5-4) is fixed by the material properties. For the LP_{01} mode of the LMA fibre, the Γ_s has a value near ~1 due to typically higher confinement of the LP_{01} mode in few-moded LMA fibres. As a result, A_{core} is the only parameter to engineer to increase the E_{sat}. In Figure 5-2, the dependence of the saturation energy on the core diameter at 1565 nm is calculated using the EDF-cross section shown in Figure 2-14 with the assumption that $\Gamma_s = 1$.

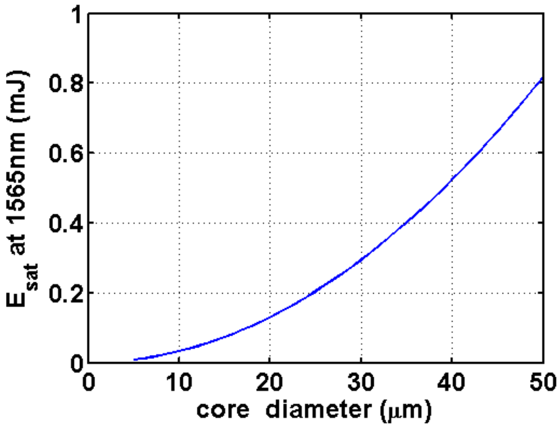

Figure 5-2 The calculated saturation energy dependence on the core diameter at 1565 nm wavelength according to the EDF-cross section shown in Figure 2-14.

The output pulse profile for a given input pulse profile can be described by the expression [31]:

$$I_{out}(t) = \frac{G_0}{G_0 - (G_0 - 1)\exp[-\frac{U_{in}(t)}{U_{sat}})]} I_{in}(t), \quad (5\text{-}5)$$

where $I_{out}(t)$ and $I_{in}(t)$ are the output and input intensity profiles of the pulse in the moving pulse frame, G_0 is the linear gain in the fibre immediately before the pulse enter, $U_{in}(t)$ is the accumulated signal energies per unit area and U_{sat} is the saturation energy per unit area.

With the above equation, the amplification of a Gaussian pulse in a pulsed fibre amplifier is calculated with the following parameters: FWHM pulse width= 100 ns, pulse energy=0.1 mJ, signal wavelength=1565 nm and the mode field diameter= 38 µm. The input and output intensity profiles of the pulse at 20 dB and 30 dB signal gain are shown in Figure 5-3(a). As the input Gaussian pulse (blue curve) is amplified to a higher energy, the peak of the pulse appears to shift in time due to the gain saturation effect. The leading edge of the pulse also becomes sharper due to the higher gain experienced by the front end of the pulse. Figure 5-3(b) shows that the output pulse broaden as the gain increases, for example, the pulse width is broadened by ~1.12 times at 30 dB gain level. In this thesis, this kind of pulse width broadening is referred as "dynamic gain saturation broadening" and was observed in the pulsed MOPA described in Section 5.3.

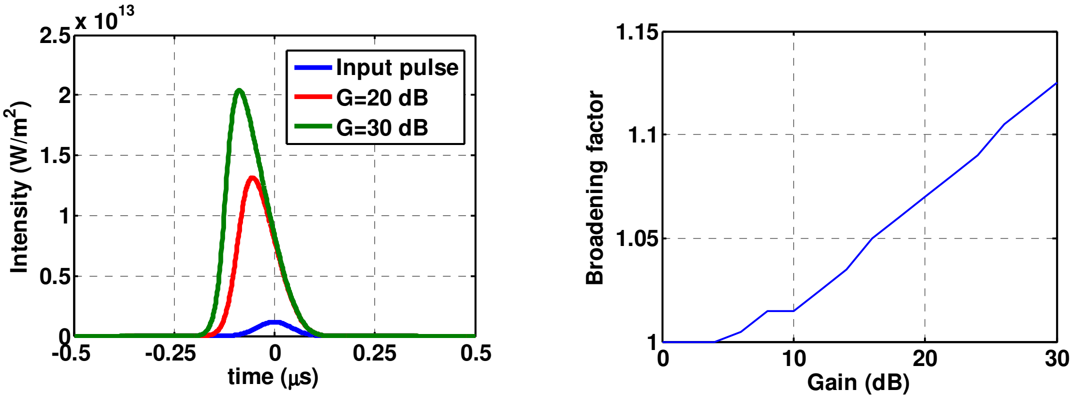

(a) (b)

Figure 5-3 (a) The intensity profiles of the Gaussian input pulse (blue) and output pulses at 20 dB (red) and 30 dB (green) gain respectively. The horizontal temporal axis is the coordinate in the moving pulse frame. (b) The ratio of FWHM of the output pulse to the input pulse, defined as broadening factor, at different gain levels.

5.1.2 Simulation model for pulse fibre amplifier

This section describes the progress in the simulation of pulsed fibre amplifiers, where pulse energy is comparable to the saturation energy (E_{sat}) while the effects of both nonlinearity and dispersion are assumed to be negligible. The general approach and equations to model this kind of pulse amplifier is the same as that for Q-switched fibre lasers (see Section 3.2.2), i.e., solving the travelling wave rate equations with the finite difference method. However, the simulation of pulsed fibre amplifier has some considerations that have not been previously described in Chapter 3.

In literature, the most useful analytical expressions to analyse this kind of pulsed fibre amplifiers have been described in Section 5.1.1 [31]. However, they are not able to provide the complete information on the behaviour of the amplifiers, for example, the dependence of the pulse energy on pump power. Therefore, many simulation models have been developed to understand the behaviour of the pulsed fibre amplifiers.

For a low repetition rate pulsed amplifier, when the inter-pulse duration is long enough for the population inversion to reach its steady-state in the absence of signal light, it is possible to separate the excitation of rare earth ions and the pulse amplification steps [79]. With this separation, the numerical challenge is reduced because the pumping of the rare earth ion is simulated with continuous rate equations and the travelling wave rate equations are solved only during the pulse amplification. On the other hand, if steady state population inversion is not reached in between the pulses, the behaviour at all spatial-temporal step must be simulated [80].

In the simulation models described above, the interaction between the optical field and the rare-earth ions is considered by the overlap factor as defined by Eq. (2-60). This approximation is valid when the mode area is larger than the core area, which is often the case for fibre amplifier for optical communication applications. However, for large mode area (LMA) fibres which are often used to extract high pulse energy due to their high saturation energy and therefore the stored energy in the fibres, a large intensity variation across the core is possible as shown in Figure 2-2 . This results in a large variation in the saturation of the population inversion across the transverse direction of the core, which renders the "overlap factor" approach to lose its accuracy. Hence, the radially dependent model (RDM) has been developed to consider the pulse amplification in LMA fibres [27].

Figure 5-4 compares the simulated amplified pulse based on the overlap factor model (OFM) and the RDM for a 30 μm and a 6 μm core fibres respectively. In both case, the OFM always overestimates the gain and exhibits a slower amplifier saturation relative to the RDM. In addition, the error introduced by the OFM is 10% for the 6 μm core fibre and goes up to 30% for the 30 μm core fibre [27]. In Section 5.5, I attribute the error introduced by the OFM as one of the limitations for the simulation model used in this thesis.

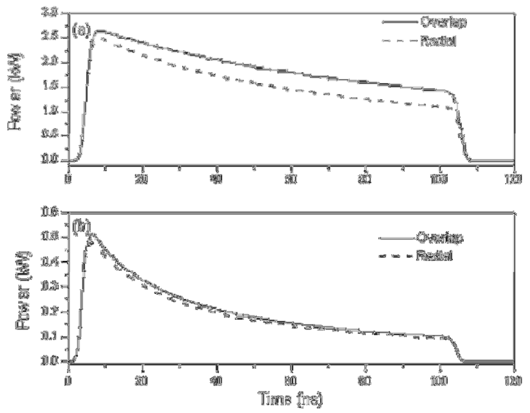

Figure 5-4 Comparison between the radially dependent model (dashed curves) and the overlap model (solid curves) for the amplification of 100 ns pulses in a (a) 30 μm core fibre pumped with 20 W and with 10 W input peak power and (b) 6 μm core fibre pumped with 10 W and with 1 W input peak power [27].

Finally, the pulse amplification in a high concentration core pumped erbium doped fibre amplifier in the presence of PIQ has also been simulated previously [81]. The result shows that the pair induced quenching can reduce the energy stored and therefore the output pulse energy from the fibre amplifier.

5.2 State of the arts

Besides the average output power, many applications, such as LIDAR, require atmospheric propagation of "eye-safe" high energy pulses. Therefore, generation of high energy pulse with EDFAs has long been pursued as shown in Figure 5-5. In this figure, the progress in the pulse energies of the ~1.55-μm nanosecond pulses are classified into 2 categories, i.e., category with $M^2>1.65$ and $M^2<1.65$. The $M^2<1.65$ is chosen arbitrarily to represent beam with a relatively good beam quality even though it is non-diffraction limited.

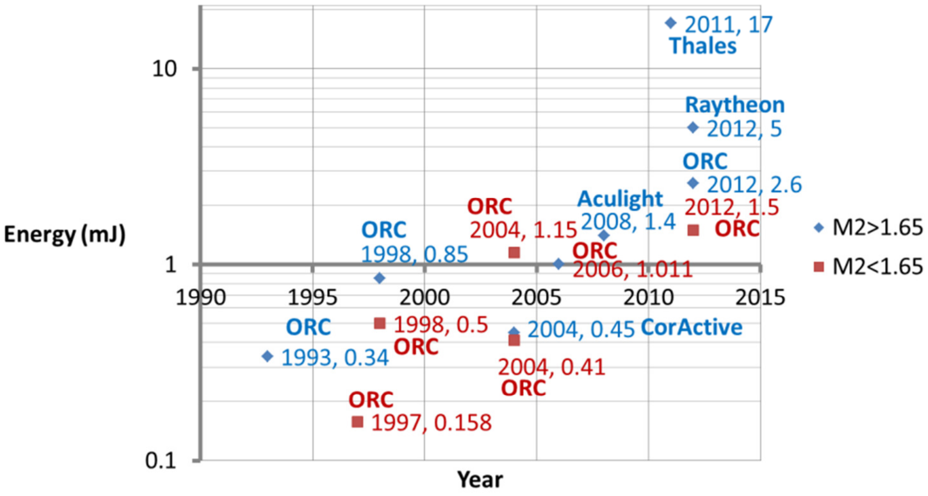

Figure 5-5 The progress of pulse energy extracted from the erbium-doped or erbium-ytterbium co-doped fibres [7, 72, 73, 77, 82-87].The results are divided into 2 categories, i.e., M2<1.65, which represents the relatively good output beam quality and M2>1.65.

In 1993, a 10-ns pulse with 0.34 mJ was successfully generated by using a multimode erbium doped fibre with 25 μm core diameter and NA of ~0.12 [82]. With the invention of the low-NA large mode area (LMA) fibre, a diffraction-limited 1 ns pulse with energy of 0.158 mJ was generated using a fibre with 310 μm^2 mode field area and 0.066 NA in 1997 [77]. The main idea of this low-NA LMA fibre is to maintain the single-mode guiding condition by reducing the NA while increasing the core area to increase the energy storage of the fibre. In the following year, the concept was further extended by having an outer ring of raised index, which increases the spot size of the fundamental mode and reduces the bending loss [83]. Furthermore, the depressed index at the centre of the core also creates a differential gain that favours the fundamental mode. As a result, a 0.52 mJ pulse (pulse width=70 ns) was generated with an effective fibre mode area of ~910 μm^2 and $M^2<1.2$. Using a slightly multi-mode fibre (core diameter of ~27 μm) 0.85 mJ pulse with M^2~2 was also generated [83].

In 2004, there were 3 separate reports on high energy pulses with good beam qualities. Two of the reports were from V. Philippov and co-workers. In the first report, 1.15 mJ pulse (pulse width=500 ns and bandwidth of 7.3 nm) was generated with M^2~1.6 by using EYDF [7]. In the second report, the same authors reported narrow linewidth 0.41 mJ pulse (pulse width=90 ns and bandwidth of 0.4 nm) with M^2~1.65 by using a cladding-pumped EYDF with A_{eff} of ~960 μm^2, core NA=0.2 corresponding to a V-number=16 [84]. The good beam quality was attributed to the selective excitation and propagation of the modes by using tapered splice techniques and controlling the bend radius of the fibre. In the third report, the 0.45 mJ (pulse width=80 ns) was reported by using a pure erbium doped fibre [85]. The power amplifier of the MOPA was a double-clad EDF (NA~0.09 and core diameter of 32 μm) pumped by 980 nm pump diode. In 2006, 1.011 mJ pulse (pulse width=88 ns) was generated by using a four stage MOPA with a power amplifier consist of a cladding-pumped EYDF with 90 μm core diameter [86].

In 2008, a 1.4-mJ pulse (pulse width=88 ns, M^2~8.5) was obtained using a cladding-pumped EDF (core diameter of ~65 μm) pumped by 980 nm laser diodes [73]. In 2009, 11-mJ pulse (pulse width=140 ns, M^2~6) was generated from a Q-switched laser using a double-clad EDF fibre with a core diameter of ~100 μm and pumped by 980 nm laser diodes. Despite the high energy, the reported spectrum consists of two peaks located at 1.56 μm and 1.59 μm with a -10 dB spectral width of 60 nm [72]. Recently, a 5 mJ pulse energy was achieved using Er-doped high aspect ratio core rectangular fibre [87].

In this work, I investigated the in-band pumping approach to achieve high pulse energy. I demonstrated ~1.5 mJ with $M^2<1.6$ and ~2.6 mJ with $M^2<4.0$ using a 40 μm core diameter pure erbium doped fibres pumped by 1535 nm fibre laser.

5.3 Experimental setup

Figure 5-6 shows my experimental setup based on a two-stage MOPA. The seed was an actively Q-switched fibre ring laser, which could be operated any user selected repetition rate between 0.3 to 5.0 kHz at ~1562.5 nm (see Chapter 3 for details about the operation of the Q-switched fibre laser). The pre-amplifier was a 4.55 m long EYDF (12 μm MFD) backward-pumped by a 915 nm multimode laser diode using GTwave-pump technology [25]. The final stage, forward-pumped CRS and CLS IP-EDFAs were realised using exactly the same piece of active fibre - a 4.9 m length of commercial (Liekki Er 60-40/140DC) pure erbium doped large mode area (Er-LMA) double clad fibre with a 40 μm core diameter, 140 μm cladding diameter, core NA of 0.1 and a core absorption of 60 dB/m at 1530 nm. In the next section, it will be shown that, at the maximum available pump power, i.e., 16 W, the chosen 4.9 m fibre is shorter than the optimal length when operating below 1.0 kHz and is longer than the optimal length when operating above 5.0 kHz for both the CRS and CLS implementations.

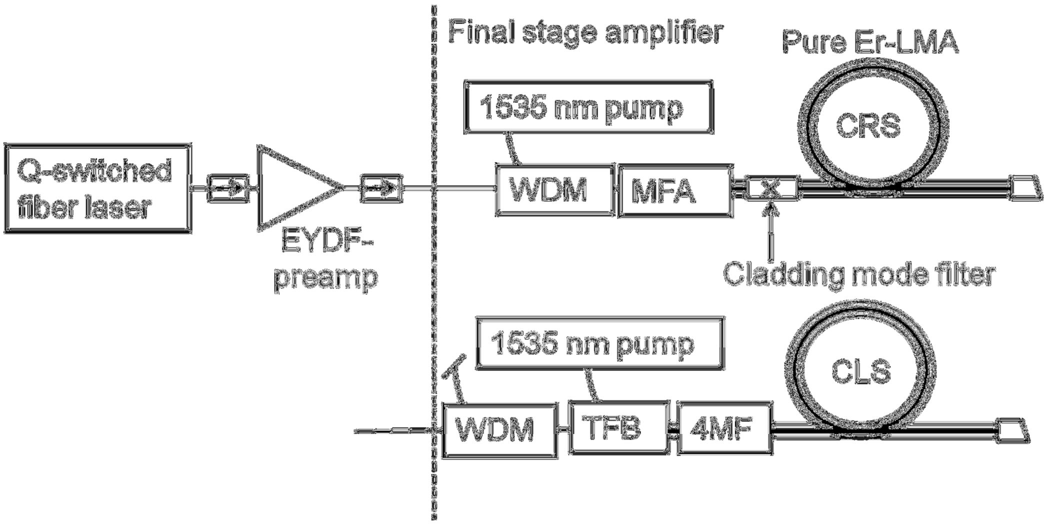

Figure 5-6 Schematic view of all-fibrised master oscillator power amplifier systems with an in-band pumped erbium-doped final amplifier stage. The upper setup represents the core pumping scheme (CRS). Since both the CRS and the cladding pumping scheme (CLS) have the same seed laser and preamplifier, only the final amplifier stage of the CLS is shown in the lower setup.

For the CRS, the signal and pump were combined and launched into the final stage Er-LMA fibre via a conventional, single-mode wavelength division multiplexer (WDM). The measured pulse energy after the WDM was 130 μJ. The pump source was a fibre Bragg grating stabilised 1535 nm single mode fibre laser (see Section 4.2). Due to the large mode field mismatch between the Er-LMA and the SMF-28 fibre based WDM coupler, a mode field adaptor (MFA) was used between the WDM output and the Er-LMA fibre. The MFA comprised a short length of intermediate fibre with a 25 μm core diameter and 0.1 NA that was carefully tapered-spliced between the Er-LMA and SMF-28 such that most of the power was coupled into the LP_{01}-mode. Since the Er-LMA was a double-clad fibre, a cladding-mode filter was used to remove any power inadvertently launched into the cladding. Overall, 89% of the available pump and signal powers after the WDM coupler were coupled into the Er-LMA fibre core.

For the CLS, a tapered fibre bundle (TFB) was spliced to the output of the WDM (which was retained in the CLS setup since it served to help eliminate out-of-band ASE). The 1535 nm pump laser was then spliced to one of the pump ports of the TFB to facilitate cladding pumping of the active fibre. We found that the MFA used within the CRS-setup introduced a relatively high insertion loss for pump light launched into the inner cladding, which was likely due to scattering of light at the glass-air interface along the taper. To avoid this loss, the TFB output was spliced to an intermediate passive fibre (4MF) with 24/125 μm core/cladding diameter and a core NA of 0.12 (supporting 4 transverse modes at 1550 nm). This intermediate fibre was then spliced to the active fibre.

The fibre length of the pump port of the TFB was ~1.5 m. From beam divergence measurements we established the effective NA of the TFB input fibre for the cladding guided light to be similar to that of the single-mode launch fibre. However, after the TFB (i.e., at the double-clad end), we estimated the effective NA of the pump guide to be ~0.30. The length of the 4MF spliced between the TFB and the active fibre was ~2 cm and the polymer coating was stripped off of this fibre to allow the pump light to be guided by the air-silica interface. Given the short length we would expect the effective NA at the 4MF output to also be ~ 0.3 and that the beam launched into the inner-cladding of the doped fibre would substantially fill the modal phase space available; providing for good cladding-pumping. Using this approach we achieved a coupling efficiency of 96% for the inner-cladding guided pump light and 59% for the core guided signal beam.

5.4 Experiment

The MOPA setup shown in Figure 5-6 can be divided into 3 different stages, i.e., the Q-switched seed laser, the pre-amplifier and the final stage IP-EDFA. The characteristics of the seed laser and the pre-amplifier are briefly described below, followed by a detailed discussion on the respective performance of the CRS and CLS IP-EDFAs.

5.4.1 Seed laser characteristics

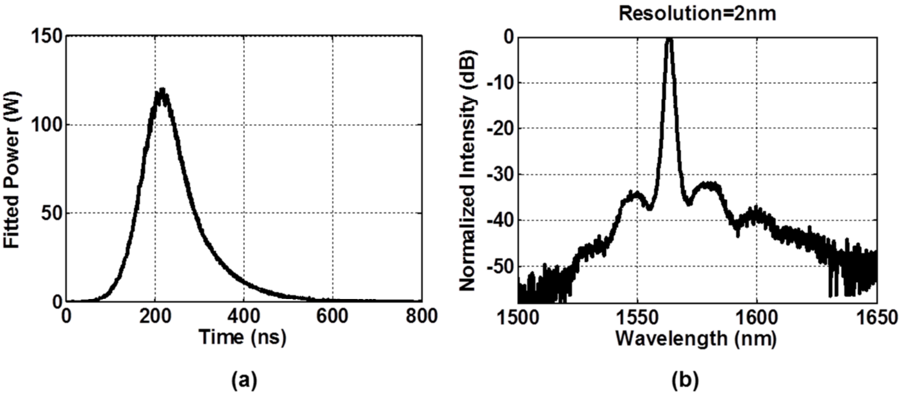

Figure 5-7 (a) The seed pulse shape (with the peak power determined by fitting the area under the measured pulse shape to the measured pulse energy). (b) The normalised output spectrum of the Q-switched seed laser.

Figure 5-7(a) shows the output pulse from the Q-switched seed fibre laser with a 500 ns AOM-rise time so as to avoid the modulated pulse envelope frequently obtained from Q-switched fibre lasers as discussed in Chapter 3. A well-defined single-peak pulse shape with no observable multiple-peak phenomenon was obtained. The measured spectrum (see Figure 5-7(b)) exhibits sidebands due to modulation instability and four wave mixing processes within the laser cavity (see Section 3.3.3). By adjusting the input pump power, it was possible to generate output pulses with the same pulse energy (~17 μJ) , optical signal to noise ratio (OSNR) (~32 dB) and pulse width (~116 ns) at pulse repetition rates between 0.3 and 5.0 kHz.

5.4.2 Pre-amplifier characteristics

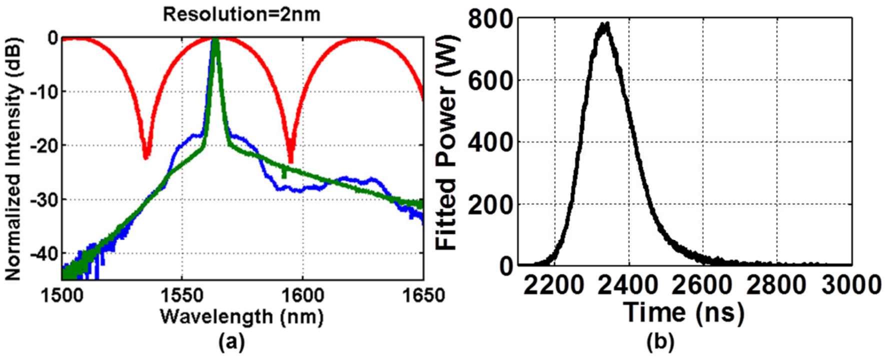

Figure 5-8 (a) The normalised output spectrum before WDM (green line), after WDM (blue line) and the transmission response of the WDM (red line). (b) The pre-amplifier pulse shape.

The output spectrum of the pre-amplifier (green line in Figure 5-8(a)) is nonlinearly broadened compared to the input spectrum (Figure 5-7(b)) due to the high pulse peak powers along the 4.55 m long EYDF pre-amplifier. When the output pulses from the EYDF pre-amplifier pass through the WDM, the pulse spectrum is further broadened due to nonlinear effects in the WDM pigtail and then partially filtered due to the WDM wavelength response (red line in Figure 5-8(a)). The corresponding output spectrum represented by the blue line in Figure 5-8(a) shows the effect of both the additional nonlinear effects and the WDM filtering response. The width of the output pulse is also increased relative to the seed laser pulse (Figure 5-8(b)) due to the effects of “dynamic gain-saturation” previously discussed in Section 5.1.1. Here again, by adjusting the input pump power, output pulses with the same pulse energy (~130 μJ) , OSNR (~18 dB) and pulse width (~149 ns) can be generated at repetition rates between 0.3 and 5.0 kHz.

5.4.3 In-band pumped final amplifier characteristics

In this section, the detailed performances of the CRS and CLS MOPAs are presented and compared.

Pulse energy and residual pump

The pulse energies were measured using a pyroelectric joulemeter (Ophir PE-10SH), which is insensitive to any continuous wave radiation components such as inter-pulse ASE and residual pump. Figure 5-9(a) shows the pulse energy generated as a function of input pump power at a repetition rate of 0.3 kHz for the CLS and CRS. At low input pump powers, the pulse energy from the CRS is initially lower than for the CLS but it increased more rapidly as the input pump power is increased. For example, with 3 W input pump power the output energy is ~0.41 mJ for the CLS, while it is only ~0.1 mJ for the CRS. At ~6.2 W input pump, the pulse energies for the CLS and the CRS are the same. Beyond that, the pulse energy for the CRS exceeds that of the CLS however it exhibits a stronger pulse energy saturation behaviour. The origin of this “cross-over” in pulse energy for the CRS and CLS is due to the effect of pair-induced quenching as I will show in Section 5.5 (see Figure 5-16(a)). The pulse energies in both cases start to saturate at an input pump power of ~7.0 W. The maximum output pulse energies are ~1.53 mJ and ~1.50 mJ for the CRS and CLS respectively.

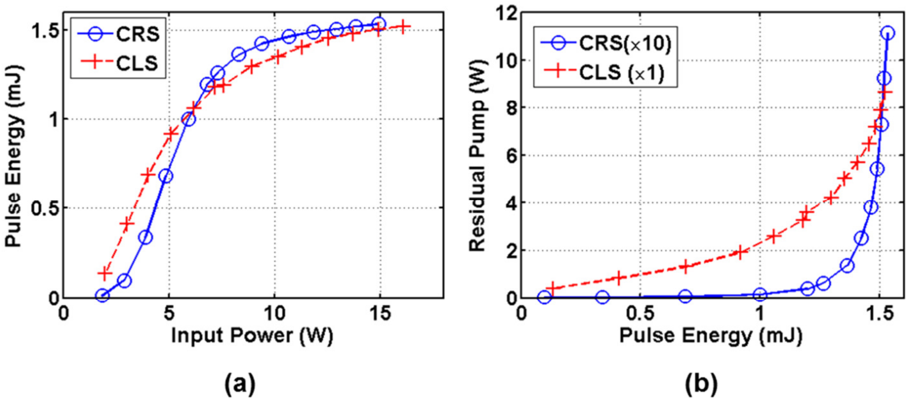

Figure 5-9 The pulse energy at different input pump powers at 0.3 kHz in the CRS (blue) and CLS (red) casess. (b) The residual pump power at different pulse energies. Note that the residual pump in the CRS has been scaled up by a factor of 10 so that the residual pump for both pumping schemes can be displayed on the same graph.

Figure 5-9(b) shows the residual pump power versus pulse energy for the CRS and CLS cases at 0.3 kHz. The residual pump powers for the CRS have been scaled up by a factor of 10 so that the residual pump powers for both the CLS and CRS can be displayed on the same graph. The residual pump for the CRS is insignificant for pulse energies below ~1.2 mJ but increase exponentially at energies above this. For the CLS, the residual pump increases linearly up to a pulse energy of ~1.2 mJ and exponentially thereafter. The residual pump for the CLS is much higher than the CRS, and in both cases the residual pump starts to increase rapidly at a pulse energy of ~1.2 mJ.

Absorbed pump and conversion efficiency

Figure 5-10(a) shows the pulse energy generated against the absorbed pump for the CLS and CRS at 0.3 kHz. It can be seen that much more pump power has been absorbed by the CRS in order to generate the same pulse energy. For example, the pump power absorbed to generate ~1.4 mJ energy pulses with the CRS (~8.6 W) is ~1.54 times higher than that required for the CLS (~5.6 W).

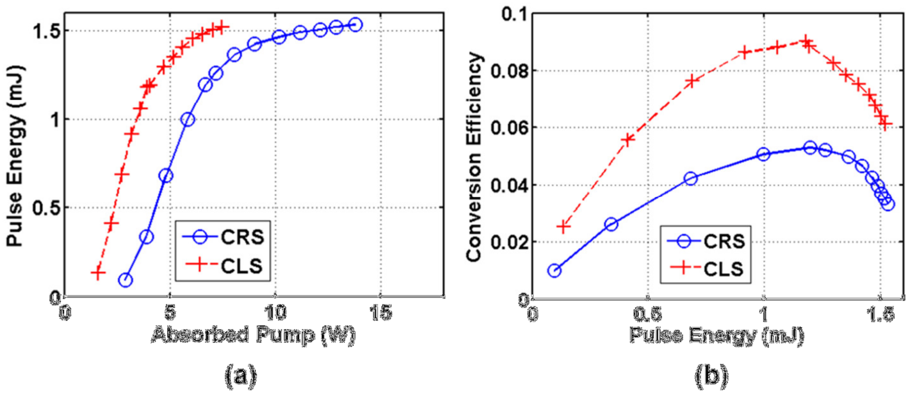

Figure 5-10 The pulse energy at different levels of absorbed pump at 0.3 kHz in the CRS (blue) and CLS (red) cases. (b) The conversion efficiency versus pulse energy.

Figure 5-10(b) shows the conversion efficiency (CE), i.e., the ratio of signal power (pulse energy × repetition rate) to the absorbed pump power, against pulse energy. The CE reaches a maximum for a pulse energy of ~1.2 mJ, which indicates that pulse energy saturation takes place at energies beyond this. This coincides with the exponential increase in residual pump at energies observed beyond ~1.2 mJ (see Figure 5-9(b)), and suggests that the pulse energy saturation is primarily caused by the saturation of the pump absorption. For the same pulse energy, the lower pump intensity in the CLS case helps to mitigate the detrimental effect of PIQ and results in a correspondingly higher efficiency in the CLS as I shall show in Section 5.5. As shown in Figure 5-10(b), the CLS is at least 1.5 times more efficient than the CRS in the range of 0.1-1.4 mJ.

Population inversion buildup time and repetition rate

Figure 5-11(a) shows the pulse energies for the CLS at different repetition rates at the maximum input pump of 16.1 W. The pulse energy saturates at a repetition rate of 1.0 kHz. The inset shows the temporal response of the system at a repetition rate of 0.3 kHz as measured using a fast photodiode. The two spikes at ~0.0 ms and ~3.3 ms correspond to the arrival of the output signal pulses. The vertical scale of the figure (i.e., 0-1 mV) is chosen such that the response in-between the two output pulses, which is what we are interested in, is clearly shown. The maximum voltage response of the output pulse is much higher than ~1 mV and has saturated the detection system. The response in-between the output pulses shows the build-up of inter-pulse ASE. The ASE build-up time, i.e., the time required for the ASE to reach steady state, is ~1 ms. The ASE build-up time also corresponds to the population inversion build-up time of the system since the ASE originates directly from the population inversion and accords well with the observed saturation in pulse energy at ~1.0 kHz. The CRS exhibits very similar behaviour.

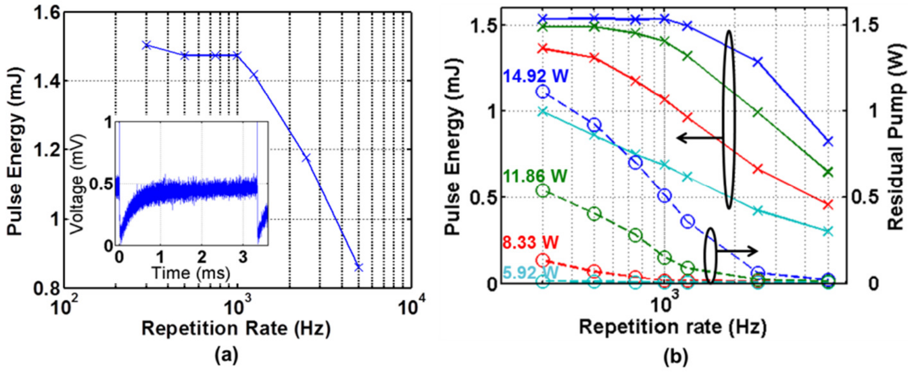

Figure 5-11 (a) The pulse energy versus repetition rate for the CLS at a pump power of ~16.1 W. The inset shows the inter-pulse temporal response measured at the fibre output. (b) The output energy (left axis) and residual pump power (right axis) versus repetition rate for 4 different input pump powers for the CRS (cyan: 5.92 W, red: 8.33 W, green: 11.86 W and blue: 14.92 W).

Figure 5-11(b) shows the pulse energy and the residual pump for CRS as a function of repetition rate for 4 different input pumps. When the input pump is set to 5.92 W (cyan lines), there is no saturation of the pulse energy or rapid increase of residual pump across all repetition rates. At an input pump of 14.92 W (blue line), the residual pump is small at 5.0 kHz. When the repetition rate decreases, the pulse energy increases but starts to saturate below 1.25 kHz. Meanwhile, the residual pump also starts to increase rapidly below 1.25 kHz. In fact, saturation of the pulse energy is always accompanied by a rapid increase in residual pump power at different input pump powers as shown in Figure 5-11(b). This phenomenon strongly suggests that the saturation of pulse energy is due to saturation of pump absorption and population inversion.

My findings also imply that as the repetition rate decreases, additional pump power becomes available to produce inversion in a longer section of active medium, i.e., the optimal length of the active fibre is increased. In fact, although it has been not highlighted previously, the simulation result in Fig. 9 of ref. [80] also shows that the optimal fibre length is increased by ~2.5 times when the repetition rate is reduced from 100 kHz to 10 kHz as shown in Figure 5-12. For example, at 20 W input pump power, the optimal length for 100 kHz and 10 kHz is ~2.5 m and ~9 m respectively. From this it can be concluded that for a given input pump, the optimal length of the fibre amplifier increases as the repetition rate is reduced.

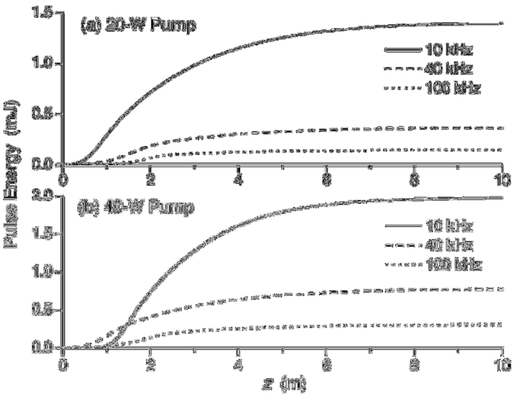

Figure 5-12 Evolution of pulse energy along the fibre under different repetition rates and pump powers [80].

Output spectra, pulse shapes and beam quality

Figure 5-13(a) shows the CRS output spectra at 3 repetition rates at the maximum input pump power. At high repetition rate (i.e., 5.0 kHz), the ASE build-up occurs at wavelengths longer than the signal wavelength (see the red curve). As the repetition rate decreases, the ASE build-up shifts toward shorter wavelengths (as shown by the green and blue curves). This phenomenon can be explained as follows: given that the input pulse energy into the final amplifier was the same for the different repetition rates, a higher repetition rate results in a lower inversion for a fixed input pump. As shown in Figure 4-2, at a lower inversion (for example, normalised inversion level of 0.4), longer wavelengths have a higher gain than shorter wavelengths. Consequently the ASE in the long wavelength region (~1585 nm) builds up at the expense of short wavelength components (~1550 nm). As the repetition rate decreases, a higher inversion is built up in-between the pulses resulting in the observed shift of the gain peak towards the shorter wavelength side. Analogously, at a fixed repetition rate, the ASE gain peak also shifts from longer to shorter wavelengths when the pump power increases. The CLS also exhibits a similar build-up of ASE with respect to the repetition rate and pump power.

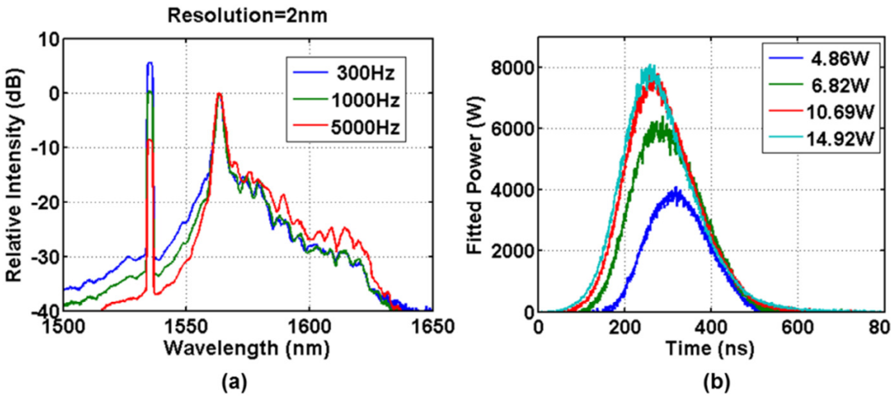

Figure 5-13 (a) The normalised CRS output spectra at 3 different repetition rates at maximum input pump power. (b) The CRS pulse shapes at 4 different input pump powers at a repetition rate of 0.3 kHz.

Figure 5-13(b) shows the pulse shapes for the CRS at a repetition rate of 0.3 kHz for4 input pump powers. As the input pump power is increased from 4.86 W to 14.92 W, a higher inversion is built-up in the active fibre. This, in turn, leads to an increase in the output energy (0.68 to 1.53 mJ) and the associated pulse peak power (~3.8 kW to ~8.0 kW). Meanwhile, the pulse appears to arrive earlier whilst its width increases from 167 to 176 ns which again due to the dynamic gain saturation effect acting on a Gaussian-like input pulse [31]. The evolution of the pulse shape for the CLS is similar to that for the CRS. For the CLS, at maximum input pump power and 0.3 kHz repetition rate, the measured pulse width is ~182 ns with a peak power of ~7.3 kW. At maximum input pump power, the M^2 of the output beam was measured to be ~1.6 in both cases.

In summary, the pulse energies for the CRS and CLS are shown to exhibit a “cross-over” with respect to the input pump power at a repetition rate of 0.3 kHz. Due to significantly lower absorbed pump power for the CLS as compared to the CRS, the CLS is more efficient than the CRS. It has also been shown that as the population inversion increases, due to either increase in pump power or decrease in repetition rate, the saturation of pulse energy always coincides with the rapid increase of residual pump.

5.4.4 CLS experiment with a longer length of fibre

In the previous section, I have experimentally shown that the saturation of pulse energy is accompanied by a rapid increase in residual pump. This indicates that the pulse energy can be further-increased if a longer fibre length is used. Due to the higher conversion efficiency and the lower pump brightness requirement in the CLS, it offers better prospects for energy up-scaling than the CRS. This motivated us to perform a CLS-based experiment with a longer length (19.5 m) of the same active fibre. Furthermore, the maximum pump power available was also increased to ~23.5 W by splicing a further 1535 nm single mode fibre laser pump to another pump port of the TFB.

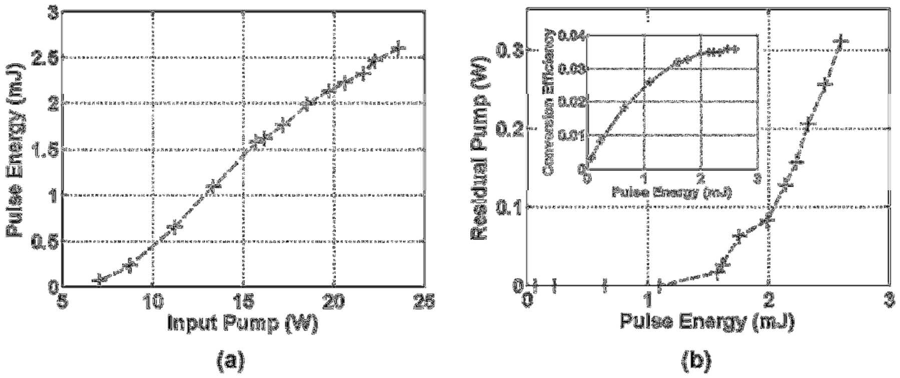

Figure 5-14 (a) The pulse energy against input pump power at a repetition rate of 0.3 kHz with a 19.5 m length of fibre. (b) The residual pump power at different pulse energies. The inset shows the conversion efficiency against pulse energy.

Figure 5-14(a) shows the pulse energy against input pump power at a repetition rate of 0.3 kHz. The maximum pulse energy of ~2.6 mJ was measured at ~23.5 W of input pump power. Figure 5-14(b) shows that the residual pump grows rapidly at a pulse energy of ~2 mJ, which corresponds well with the onset of the saturation of the conversion efficiency at ~2 mJ shown in the inset of Figure 5-14(b). Thus, the saturation of pulse energy again coincides with a rapid increase in the pump power, which again suggests pump and population inversion saturation. The output pulse has a FWHM of 100 ns and a fitted peak power of ~24 kW. I attribute the shorter pulse width compared to the input pulse width again to the gain saturation effects associated with the specific shape of the Q-switched pulse. The M^2 of the output beam was measured to be ~4.2. The lower beam quality in this case is due to the longer active fibre length that prevents us from performing active alignment of the cores when splicing between the 4MF and the LMA at the signal wavelength.

During the experiment described in Section 5.4.3, we also experimentally investigated the effect of splicing conditions on the output pulse energy. Our results showed that by degrading the quality of the launch into the fundamental mode (and hence launching more light in to higher-order modes) increases in pulse energy of up to ~10% can be achieved, albeit with an associated degradation in output beam quality. Consequently we conclude that the ~70% pulse energy increase observed when using a longer fibre is indeed due primarily to the increase in fibre length while the decrease of beam quality playing only a secondary role. Thus, with the increase in fibre length and pump power we have been able to scale the pulse energy from the CLS based approach to ~2.6 mJ.

5.5 Simulation

In the literature to date, to the best of my knowledge, pulse energy saturation in such pulse fibre MOPAs has been attributed to ASE self-saturation, spurious lasing and ASE seeding from the preamplifiers [7, 27, 77, 78]. However, as described in the previous section, I have observed the saturation of pulse energy to coincide with a rapid increase in residual pump power. This leads us to conclude that the saturation of pulse energy in my experiment is due to pump and population inversion saturation within the gain media. Hence, in this section, I provide support for this explanation for the mechanism of pulse energy saturation with the help of a numerical simulation model. Meanwhile, I also compare the impact of pair-induced quenching on CRS and CLS based low repetition rate in-band pumped erbium doped fibre amplifiers.

5.5.1 The simulation model

5.5.1.1 Simulation approach

The general approach I have used to simulate low repetition rate fibre amplifiers is similar to that used in [79], where the behaviour of the fibre amplifier is considered in two separate steps:

Step 1: Excitation step.

In this step, the ions in the active fibre are assumed to be excited by the pump power for a sufficiently long duration such that in the absence of signal power a steady state population inversion is reached. The inset of Figure 5-11(a) shows that the population inversion build-up time is ~1 ms. Therefore, this steady state assumption is valid for repetition rates of 1 kHz and below. This steady state behaviour can be simulated using the continuous wave EDFA model. In the cw model, the ion population density in the presence of PIQ is considered by Eq. (4-5) and the optical power evolution is considered by Eqs. (2-63) and (2-64). In this work, the cw behaviour of the fibre amplifier is simulated with the Optisystem software.

Step 2: Pulse amplification step.

When the steady state inversion is reached, the pulse amplification is modelled by passing a signal pulse through the fibre amplifier. The amplification of the input pulse is simulated by solving the spatio-temporal rate equation using the finite difference method (see Section 3.2.2). The grid spacing used in the time domain was 50 ps and Courant number is 0.9. In this work, the pulse amplification behaviour is simulated using a self-developed MATLAB code as described in Section 3.2.2.

5.5.1.2 Simulation parameters

I have previously used the current active fibre in continuous wave CRS experiments and obtained estimates of the key parameters required to describe the performance of the fibre (see Section 4.4.2). The values of the key simulation parameters are listed as follows: fibre length =4.9 m, core absorption=60 dB/m at 1530 nm, Er-doping diameter=40 μm, core diameter=40 μm, core NA=0.1, overlap factor in CRS =0.975, concentration of Er-ions=3.23×10^{25} /m^3, fluorescence lifetime of Er-ions=10 ms, k=4.1%, and the absorption/emission cross section values are taken from [22].

5.5.1.3 Limitations

My modelling makes a number of assumptions and has a number of limitations that it is important to recognize and which at some level will limit its accuracy.

Firstly, I assume that the signal pulse excites only the LP_{01}-mode and consequently we take the interaction between the optical field and the active ions into account using the confined doping model (CDM), where the overlap between the optical mode and the doping area is accounted for using an overlap factor [22, 27]. To understand the limitation of the CDM, it is useful to remind ourselves of the normalised modal intensity profiles of a step index fibre. With the single mode condition, for example when the normalised frequency (V) is ~2.35, the mode intensity decreases from 1.00 in the centre of the core to 0.51 at the core-cladding interface (see Table 2). The CDM is therefore suitable for single mode fibre because the transverse variations of the population inversion do not depend much on the saturation level. However, for a large mode area fibre (LMA), for example when $V\approx 8.11$ (corresponding to my active fibre), the mode intensity of LP_{01}-mode decreases from 1.00 to 0.02 at the core-cladding interface. This results in a large variation in saturation of the population inversion in the transverse direction across the core. Hence, the accuracy of the CDM is compromised in LMA fibre. In fact, it has been shown that, for a fibre with a 30 μm core diameter (V=10.64), the error introduced by use of the CDM is ~30% compared to a simulation model that properly considers transversely dependent saturation effects [27]. This indicates that my simulation model is likely to overestimate the pulse energy.

Secondly, the residual pump (see for example Fig. Figure 5-16(b)) is simulated using step 1 described above, which is based on the steady state assumption in the absence of signal power, i.e., the input pulse is taking no part in the redistribution of the stored energy. However, in practice, the presence of signal power will inevitably affect the inversion level through the process of stimulated emission, which leads to a higher pump absorption and lower residual pump compared to the simulation.

The two limitations discussed above show that my simulation model is likely to overestimate the pulse energy and residual pump power. Nevertheless I still consider it of value and believe that is still able to explain the various effects I have observed and in particular how pump saturation leads to the pulse energy saturation observed in my experiment.

5.5.2 Explanation for pulse energy saturation due to pump saturation

In this section, I describe the pulse energy saturation mechanism and how pair induced quenching leads to the "cross-over" behaviour of the output energies between the CRS and CLS.

Inversion level and spatial evolution of pulse energy

From step 1 of the simulation model, the population inversion along the active fibre at different condition can be simulated. Figure 5-15(a) shows the population inversion for input pump power of 3 W (dashed line), 4 W (dotted line) and 16 W (solid line) for the CLS (red) and CRS (blue) respectively in the presence of PIQ (*k*=4.1%). In case of CRS, a significant portion of the input pump power is lost through the PIQ process. Hence, a 3 W input pump is not sufficient to invert the last 1 m section of active fibre. In contrast, for the CLS at 3 W input pump power a more uniform inversion is achieved along the active fibre since PIQ is less detrimental due to the lower pump intensity. When the input pump approaches 4 W, the inversion level of CRS near the end of the active fibre starts to develop. Meanwhile, the overall inversion profile of the CLS increases slightly since the inversion along the fibre length is already close to the transparency inversion of ~0.5. Thus, most of the input pump cannot be absorbed but passes straight through the active fibre. As the pump power is increased even further, only a small fraction of the remaining ions are inverted because the population inversion approaches close to its maximum value (i.e., the saturation of the pump and population inversion has occurred). At 16 W input pump (solid line), the inversion is almost uniform along the entire length of fibre in both cases.

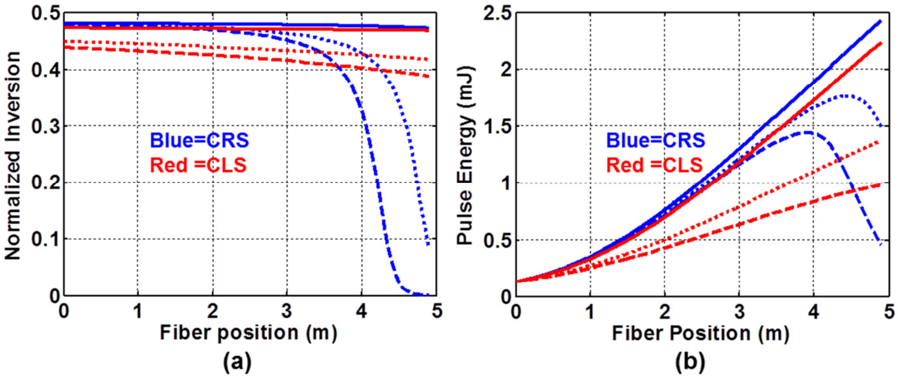

Figure 5-15 (a) The normalised inversion at an input pump power of 3W (dashed line), 4W (dotted line) and 16 W (solid line) for the CRS (blue) and CLS (red) respectively in the presence of PIQ (i.e., k=4.1%). (b) The spatial evolution of the pulse energy at input pump power of 3 W (dashed line), 4 W (dotted line) and 16 W (solid line) for the CRS (blue) and CLS (red) respectively in the presence of PIQ (i.e., k=4.1%).

From step 2 of the simulation model, the spatial evolution of the pulse energy along the active fibre can be simulated using the population inversion profile obtained from step 1. The input pulse is a

Guassian pulse of width 149 ns (FWHM) and energy of 130 μJ, equivalent to the experimental pulse width and pulse energy at the output of the pre-amplifier in Section 5.4.2. Figure 5-15(b) shows the spatial evolution for input pump power levels of 3 W (dashed line), 4W (dotted line) and 16 W (solid line) for both the CRS (blue) and the CLS (red) cases and assuming k=4.1%. At an input pump power level of 3 W the pulse energy for the CRS grows much faster in the front section of the fibre because the higher pump intensity results in a higher local gain. However, the higher pump intensity also induces a stronger detrimental effect due to PIQ, which in effect reduces the effective pump power available. Consequently, the pump power is not sufficient to invert the rear section of the fibre (blue dashed line in Figure 5-15(a)) and so the initially amplified pulse is reabsorbed by the active fibre. On the other hand, the inversion is fairly uniform for the CLS (red dashed line in Figure 5-15(a)) since the PIQ is less severe due to the lower CLS pump intensity. Therefore, the pulse is amplified along the full length of active fibre and generates more output energy than the CRS. At an input pump level of 4 W the CRS pulse energy still undergoes reabsorption while the CLS pulse energy grows monotonically along the active fibre. At the output of the fibre, the output pulse from the CRS is already slightly higher in energy than for the CLS. Beyond 4 W of input pump power, the output energies in both cases start to saturate as a result of the saturation of population inversion. At an input pump power level of 16 W the output energy from the CRS (2.43 mJ) is slightly higher than that of the CLS (2.24 mJ).

Output energy and residual pump

Figure 5-16(a) shows the output pulse energy calculated with step 1 and step 2 of the simulation model at different conditions (including the case where paired ions are absent, i.e k=0.0%). In the absence of paired ions, the absorbed pump energy contributes only to the creation of a population inversion. When the transparency inversion (~0.5 for 1535 nm pump) is reached additional pump power can no longer be absorbed. Under this condition, the active fibre becomes transparent at the pump wavelength and any excess pump power will pass straight through the active fibre, i.e., pump saturation has occurred. This, in turn, leads to the saturation of pulse energy. Furthermore, the pulse energy for the CRS builds-up more rapidly than for the CLS due to the higher pump absorption in the CRS. Hence, the pulse energy for the CRS is always higher than that of the CLS for a given input pump. In the presence of paired ions, the absorbed pump energy not only contributes to the creation of population inversion, but also suffers additional losses due to PIQ. As a result, the pulse energy for the CRS is lower (or higher) than that of the CLS when the input pump power is below (or above) ~3.8 W. Consequently, the pulse energies for the CRS and the CLS exhibit a “cross-over” at ~3.8 W due to the effects of PIQ.

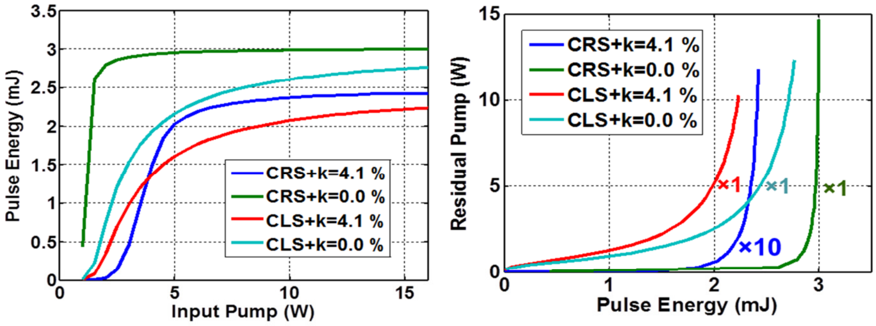

(a) (b)

Figure 5-16 (a) The pulse energy at different input pump power levels in the presence (*k*=4.1%) and absence (*k*=0.0%) of paired ions. (b) The residual pump power at different output pulse energies. Note that the residual pump power for the CRS with PIQ has been scaled up by a factor of 10 so that the residual pump power can be displayed on the same plot for all cases.

The residual pump power at different output pulse energies can be obtained from step 1 described in Section 5.1. Figure 5-16(b) shows the residual pump for various output energies and pumping conditions. Note that the residual pump for the CRS, with the effects of PIQ included, have been scaled up by a factor of 10 so that the residual pump powers for all cases can be displayed on the same graph. In the absence of PIQ, the maximum residual pump for the CLS (~12.3 W) is lower than the CRS (~14.7 W) due to the coating attenuation experienced by the cladding guided pump light. If the coating attenuation is not considered, the maximum residual pumps become identical (~14.7 W) for both the CRS and CLS cases. In the presence of PIQ, there is neglible residual pump for up to ~2.0 mJ of pulse energy in the case of the CRS. After that, the pulse energy starts to saturate and the residual pump power increases exponentially up to ~1.2 W at ~2.42 mJ of pulse energy. In the case of the CLS, the residual pump power increases linearly with pulse energy up to ~2.0 mJ, beyond which it increases exponentially with further increases in input pump power. Previously (see the discussion relating to Figure 5-16(a)), I have shown that the pulse energy is limited by pump saturation. The exponential increase of residual pump is a clear signature of the pulse energy saturation caused by pump saturation.

Discussion

Comparing Figure 5-9 and Figure 5-16, both experiment and simulation exhibit the pulse energy “cross-over” behaviour and that the CRS generates higher pulse energy at the maximum input pump power level. Furthermore, just as in the experiment, the simulated residual pump in the CRS is much lower than that for the CLS when the effects of PIQ are taken into account. Finally, both experiment and simulation also show that the residual pump increases exponentially as the pulse energy saturates. Therefore, despite the relative simplicity and limitations of my model, the characteristic behaviours of the experiments have been reproduced successfully. Accordingly, I believe that the simulations can be relied upon to understand and to explain the main experimental observations and in particular my description of the mechanism by which saturation of the pump absorption and hence the population inversion leads to pulse energy saturation. Finally, I would like to note that this pulse energy saturation mechanism can also occur in other types of in-band pumped pulsed fibre amplifiers, such as the ~975 nm pumped ytterbium doped fibre amplifiers and is particularly prone to occur when the gain fibre is pumped at a wavelength that exhibits low transparency inversion.

5.6 Conclusion

I have demonstrated and compared high energy, low repetition rate, nanosecond pulse fully-fibrised MOPAs based on in-band pumped erbium doped fibre amplifiers pumped either using a core-pumping scheme, or a cladding-pumping scheme, and constructed using exactly the same piece of active fibre. The maximum output energies obtained were ~1.53 mJ and ~1.50 mJ for the core-pumping scheme and cladding-pumping scheme respectively. The cladding-pumped MOPA scheme is >1.5 times more efficient in term of conversion efficiency than the equivalent core-pumping scheme variant due to the lower pump intensity in the cladding-pumping scheme which helps to mitigate the detrimental effects of pair-induced quenching. The M^2 of the output beam was measured to be ~1.6 in both cases. With a longer length of fibre operated in a cladding-pumped configuration, I have achieved an output pulse energy of ~2.6 mJ with an M^2 of ~4.2.

A simulation model has been used to understand how saturation of pump absorption and population inversion lead both to output pulse energy saturation and the rapid increase in residual pump observed in my experiment. The model also shows that for the generation of pulses of the same output pulse energy the effects of pair-induced quenching increases the absorbed pump requirements of the core-pumping scheme compared to cladding-pumping scheme. This, in turn, leads to the pulse energy cross-over observed in my experiments. It is shown that, as the inversion level increases in an in-band pumped pulsed fibre amplifier, either due to an increase in pump power or a decrease in pulse repetition rate, pump saturation can cause saturation of the output pulse energy.

Chapter 6 Conclusion and future work

In this chapter, the important conclusions from this thesis are first summarised. After that, potential future work will be discussed.

6.1 Conclusion

In Chapter 3, Q-switched erbium doped fibre lasers are investigated. I first demonstrate in a core pumped Q-switched erbium doped fibre ring laser the multiple-peak phenomenon (MPP), in which the Q-switched pulse develops sub-structure and can even break into multiple sub pulses. This phenomenon is clearly highly undesirable for many applications. Next, I eliminate the MPP by increasing the AOM rise time through changing the ramp rate of the electrical pulse that drives the AOM. Furthermore, an experimentally validated numerical model has been used to show that the MPP originates from the fast AOM rise time (compared to cavity round trip time) that defined a "step-like seed pulse" during the initial build-up of the Q-switched fibre ring laser. This "seed pulse" is amplified during subsequent round trips through the amplifier and a pulse with a "staircase-like" envelope with a period of the cavity round trip time emerges at the laser output. As the pulse energy increases and amplifier saturation takes place the step features on the original seed pulse increasingly sharpen leading to the apparent substructure within the longer overall Q-switched pulse envelope. For longer AOM rise times the amplitude variation across the "seed pulse" formed during the first cavity round trip is less pronounced and a smooth pulse profile emerges during repeated cycles of amplification.

Next, a cladding pumped Q-switched erbium doped fibre ring laser was investigated because higher pulse energy can be generated in the cladding pumping scheme due to the higher pump power available. Since the MPP and nonlinear effect are decoupled in my experiment, the nonlinear effects in cladding-pumped Q-switched fibre lasers can be systematically studied for the first time. I show that nonlinear effects play no role in instigating the MPP and that it is due to gain dynamics/the AOM rise time alone. My results show that MI and FWM can develop within an anomalously dispersive, Q-switched fibre laser. Finally, I show that, even though it is not directly observable with an OSA, the complex interplay of MPP and nonlinearity changes the detail of the spectral evolution and is measured through spectrally resolved time gating of the Q-switched pulse.

In Chapter 4, continuous wave in-band pumped erbium doped fibre amplifiers are investigated. Firstly, a highly efficient (~ 80%), high power (18.45 W) in-band core pumped, all-fibre MOPA is demonstrated using an in-house EYDF fibre. Next, a similar experiment was performed with a commercial (Liekki Er 60-40/140DC) pure erbium doped large mode area fibre and found that the efficiency is only about ~37% at best. Next, I identified through the fitting of the experimental results that concentration quenching, especially the pair induced quenching, can represent a major limiting factor in achieving highly efficient, high power, in-band pumped EDFAs. Furthermore, I believe that the high efficiency demonstrated with my in-band pumped EYDF fibre is due to the formation of erbium-ytterbium ion cluster that inhibits the pair induced quenching. I have also performed a cladding pumped experiment, where a relatively low efficiency of ~ 47% is demonstrated. In trying to establish the reason for these relatively low measured PCEs, I measured the background loss of the cladding guided pump light due to the fibre coating to be ~0.15 dB/m at 1535 nm in the passive version of the commercial fibre (Liekki Passive-40/140 DC). When this background loss is introduced into the simulation model, I obtained a very good fit to the experimental results.

Through the use of numerical modelling, I have found that the cladding pumping scheme is far less susceptible to the detrimental effects of pair induced quenching compared to the core pumping scheme due to the lower pump intensity in the cladding pumping scheme. Furthermore, the backward pumping scheme is less susceptible to the detrimental effects of pair induced quenching compared to the forward pumping scheme. The physical reason for this is that in the case of backward pumping scheme, the backward propagating pump is strongest in the region where the signal is strongest. Thus, the inversion can be most efficiently depleted by the signal thereby reducing the peak local inversion within the fibre and thereby reducing the efficiency and net effect of the pair induced quenching. Consequently, the detrimental effect of the pair induced quenching is mitigated. Hence, I conclude that backward, in-band cladding pumping should be employed not only to scale up the output power to the kW regime but also to mitigate the effect of concentration quenching.

In Chapter 5, high energy in-band pumped erbium doped fibre amplifiers are investigated. I demonstrate and compare high energy, low repetition rate, nanosecond pulse fully-fibrised MOPAs based on in-band pumped erbium doped fibre amplifiers pumped either using a core pumping scheme, or a cladding-pumping scheme. Both the core-pumping scheme and cladding pumping MOPAs are constructed using exactly the same Q-switched seed fibre laser, pre-amplifier and active fibre. The maximum output energies obtained were ~1.53 mJ and ~1.50 mJ for the core-pumping scheme and cladding-pumping scheme respectively. The cladding-pumped MOPA scheme however is >1.5 times more efficient in term of conversion efficiency than the equivalent core-pumping scheme variant due to the lower pump intensity in the cladding-pumping scheme which helps to mitigate the detrimental effects of pair-induced quenching. The M^2 of the output beam was measured to be ~1.6 in both cases. With a longer length of fibre operated in a cladding-pumped configuration, I have achieved an output pulse energy of ~2.6 mJ with an M^2 of ~4.2.

A simulation model has been used to understand how saturation of the pump absorption leads to output pulse energy saturation and the rapid increase in residual pump observed in my experiment. The model also shows that for the generation of pulses of the same output pulse energy the effects of pair-induced quenching increases the absorbed pump requirements of the core-pumping scheme compared to the cladding-pumping scheme. This, in turn, leads to the pulse energy cross-over observed in my experiments. It is shown that, as the inversion level increases in an in-band pumped pulsed fibre amplifier, either due to an increase in pump power or a decrease in pulse repetition rate, pump saturation can cause saturation of the output pulse energy.

In **Error! Reference source not found.**, all-fibre frequency-doubled fibre lasers based on periodically poled silica fibre (PPSF) are investigated. The first harmonic source (FH source) is a master oscillator power amplifier (MOPA) seeded with a tuneable external cavity laser with the central wavelength chosen to matched the optimal quasi-phase matched wavelength. A high power all-fibre frequency doubled laser is demonstrated with 1.13 W of second harmonic average power with ~27% conversion efficiency. During the high power operation, the heat deposition along the PPSF shifts the optimal quasi-phase matched wavelength to a longer wavelength by ~0.14 nm. This shift must be compensated to achieve optimal performance of the PPSF under test and is achieved in my experiment by tuning the central wavelength of fundamental source.

The degradation of the PPSF sample has been observed in one of my PPSF sample at a fibre core intensity of ~332 MW/cm^2 at 775 nm. At the end of the high power experiment, the PPSF samples in my experiments degraded to ~40% of the pristine PPSF normalised efficiencies. My results also suggest that the degradation of the PPSF seems to saturate, i.e., the degradation stops after some time. The glass property of the PPSF is changed by both UV exposure and high power exposure as indicated by the changes in the transmission spectrum between 400 nm and 800 nm.

6.2 Future work

In this thesis, the in-band pumped erbium doped fibre amplifier has been explored in continuous wave and nanosecond low repetition rate operation. However, it can also operate in other pulse regimes, for example, in-band pumped fibre amplifiers with sub-nano [75], sub-picosecond [105] pulse widths have been demonstrated. However, substantial progress in the fibre property must be made, for the in-band pumped erbium doped fibre amplifiers to ultimately reach, if not rival, the efficiency and the average power of current ytterbium doped fibre amplifiers. To reach high power, a cladding pumping scheme with highly doped erbium doped fibre amplifier must be implemented to achieve sufficient pump absorption. In this case, the concentration quenching must be further reduced. In this work, a 80% conversion efficiency has been demonstrated in a core pumped erbium ytterbium co-doped fibre. Following my demonstration, a separate group has also demonstrated a conversion efficient of 71% [61] in a cladding pumping scheme using a similar approach. These two results strongly suggest that a more systematic study of the effects of ytterbium as a concentration quenching inhibitor would yield interesting results. In terms of fibre host materials, it would be interesting to explore the P_2O_5-Al_2O_3-SiO_2 (PAS) ternary glass, which exhibits a structure similar to that of SiO_2 glass, a refractive index below SiO_2 glass and a reduced concentration quenching effect [65]. Meanwhile, the outer cladding of the double clad fibre should also be a material that exhibits low absorption at 1535 nm. If a fibre that allows >90% PCE can be realised, it would then provide a strong motivation to develop the pump power for kilowatts-level average power demonstration.

Currently, there are several published results that discuss the power scaling limit of fibre lasers, with the focus on ytterbium doped fibre lasers [106, 107], which operate in the normal dispersion regime. In this spectral region, the nonlinear effect that limits the power scaling in the stimulated Raman Scattering (or stimulated Brillouin Scatting for narrow linewidth source). However, 1.5 μm erbium doped fibre laser resides in the anomalous dispersion regime. Currently, the power scaling of in-band pumped erbium doped fibre is limited by the pump power available rather than nonlinear effects. However, from my experiments on the pulse amplifier, the modulation instability is the first nonlinear effect that results in the transfer of signal power to other wavelength and degrades the fidelity of the laser output. Therefore, it would be interesting to re-evaluate the power scaling limit of IP-EDFA with a consideration of MI. At the same time, the same analysis can also be applicable to other types of high power fibre amplifier operating in anomalous dispersion regime, such as thulium doped fibre amplifiers. The analysis of the threshold power when MI becomes severe should be similar to the analysis of super continuum generation with the continuous wave laser [108] in which MI plays an important role in the early development of super continuum.

In term of high pulse energy generation, the in-band pumping exhibits a lower inversion level than the 980 nm pumping scheme. This lower inversion results in a lower ASE and potentially exhibits higher energy storage with a longer fibre length [109]. Such comparison between 980 nm and 1535 nm pumped high energy pulse lasers have yet to be investigated. To improve the beam quality of the MOPA, novel waveguide structures [4, 110] as well as better tapering and splicing techniques [111] are required. In term of simulation, the spatial overlap between the optical power and rare earth ions has been considered by the overlap factor in this thesis. Although the model is able to explain the experimental trends, it has over-estimated the pulse energy. Therefore, a transverse spatially dependence amplifier model can be implemented to improvement the accuracy.

In this thesis, the exact degradation mechanism of the PPSF nonlinearity during high power operation remains unknown. The understanding of this degradation should be the first step to improve the long term stability of the PPSF sample and should be carried out as soon as possible. In term of improving the fundamental MOPA source, changing the current pump diode from 915 nm to 975 nm, would allow reduce of the nonlinear spectral broadening. This is because the 975 nm pumped EYDF exhibits higher pump absorption than the 915 nm variant and therefore shortens both the amplifier and the nonlinear length. Finally, a fully polarisation maintaining system should also be implemented to stabilize the polarisation drift during high power operation.

Chapter 7 Appendix

7.1 Derivation of the rate equations for the upconversion of erbium ions

In this section, the rate equations for the upconversion of erbium ions are derived. The erbium ions in the active fibre are assumed to have undergone two possible types of ions-ions interactions, namely the homogeneous upconversion (HUC) and pair induced quenching (PIQ) [22, 42, 43, 48, 51]. In this model, all ions can exist as two distinct ion species: independent ions and paired-ions (PI). In the case of PI, two ions form an ion-cluster (IC) due to their close proximity. With $2k$ as the fraction of ions exist as the PI, the total ion concentration, N_t^k , exist as PI can be expressed as $N_t^k = 2kN_t$, where N_t is the total ion concentration. Consequently, the total number of independent ions, N_t^i , can be expressed as $N_t^i = N_t - N_t^k = N_t(1-2k)$.

The independent ions

The independent ions can undergo HUC, where the nonradiative energy transfer between the two^{4}I$_{13/2}$-excited ions results in one ion decay to the ground state and another ion excited to the ^{4}I$_{9/2}$-state. The ^{4}I$_{9/2}$-excited ions will rapidly relax to ^{4}I$_{11/2}$ or ^{4}I$_{15/2}$-level. Assuming the population of both the upconversion level ^{4}I$_{9/2}$ and the level ^{4}I$_{11/2}$ is negligibly small, the rate equation for the independent ions can be written as follows [22, 48]:

$$\frac{dN_1^i}{dt} = -\frac{dN_2^i}{dt} = A_i N_2^i - R_{12}^i N_1^i + R_{21}^i N_2^i + (1+\frac{1}{m})C N_2^{i\,2}. \tag{7-1}$$

In the above equation, the superscript *i* signifies rates for independent ions.1/*m* is the branching ratio between relaxation process to ^{4}I$_{11/2}$ and ^{4}I$_{15/2}$, N_1^i and N_2^i are population densities of the ground level (^{4}I$_{15/2}$) and upper lasing level (^{4}I$_{13/2}$) respectively, C is the upconversion coefficient. The R_{12}^i , R_{21}^i and A^i are the absorption, stimulated emission and spontaneous emission rates respectively and are defined as:

$$R_{12}^i = \int_0^\infty \frac{\sigma_a(\upsilon)I(\upsilon)}{h\upsilon} d\upsilon, \tag{7-2}$$

$$R_{21}^i = \int_0^\infty \frac{\sigma_e(\upsilon)I(\upsilon)}{h\upsilon} d\upsilon, \tag{7-3}$$

$$A^i = \frac{1}{\tau}, \tag{7-4}$$

where $\sigma_e(\upsilon)$ and $\sigma_a(\upsilon)$ denote the $^4I_{15/2}$-absorption cross section and $^4I_{13/2}$-emission cross section, $I(\upsilon)$ is the intensity spectrum and τ is the lifetime of $^4I_{13/2}$. Under the steady state condition, the rate equation becomes:

$$N_2^i = \frac{R_{12}^i N_t^i}{A_i + R_{12}^i + R_{21}^i + (1+\frac{1}{2})CN_2^i}, \tag{7-5}$$

with $N_t^i = N_1^i + N_2^i$.

The paired-ions

In the paired-ions case, when both ions of the IC are excited, the nonradiative energy transfer between them is so fast that only one ion of the IC can remain in the excited state [22, 42, 43, 51]. The difference between PIQ and HUC is that, in the HUC, if an ion is excited, it does not prohibit neighbouring ions to go to the excited state. However, in PIQ, when one ion of IC go to the excited states, the other ion in the IC must be in its ground state [22].

As a result, the IC can be in either of the two states: State I: two ions in ground state or State II: one ion in the excited state and one ion in the ground state. Hence, the rate equation for IC can be written as [51]:

$$\frac{dK_I}{dt} = -\frac{dK_{II}}{dt} = A_k K_{II} - R_{12}^k K_I + R_{21}^k K_{II}. \tag{7-6}$$

In the above expression, the superscripts *k* signifies the rate for IC. The K_I and K_{II} are IC concentration in State I and State II respectively. The R_{12}^k, R_{21}^k and A^k are the absorption, stimulated emission and spontaneous emission rates of IC respectively and are defined as:

$$R_{12}^k = 2R_{12}^i, \tag{7-7}$$

$$R_{21}^k = R_{21}^i, \tag{7-8}$$

$$A^k = A^i. \tag{7-9}$$

The factor of 2 appears in the right hand side of Eq. (7-7) is due to the fact that the probability of IC in State I absorbing a photon is twice that of a single independent ion because an IC in State I consists of two ground state ions. Meanwhile, the stimulated emission rates of IC are the same as the single excited ions because an IC in State II consists of only one excited state ion.

For simulation, it is convenient to express the rate equation in terms of the ion population density. Let N_1^k and N_2^k be the ion population density of paired ions in the ground and upper lasing levels respectively. Then, $K_{II} = N_2^k$ because the number of IC in state II is equal to the number of PI in upper energy state. Due to the clustered nature of the PI, for each excited ion, there is a corresponding ground state ion associated with it. Hence, the population density of ground state ions in State I, i.e., not in State II, is given by $N_1^k - N_2^k$, which is also equal to twice the IC concentration in State I, i.e., $2K_i = N_1^k - N_2^k$. Furthermore, the relationship between the IC concentration and the ion population density is also illustrated in Figure 7-1 using a simple case where 4 ICs are in state I and 3 ICs are in state II.

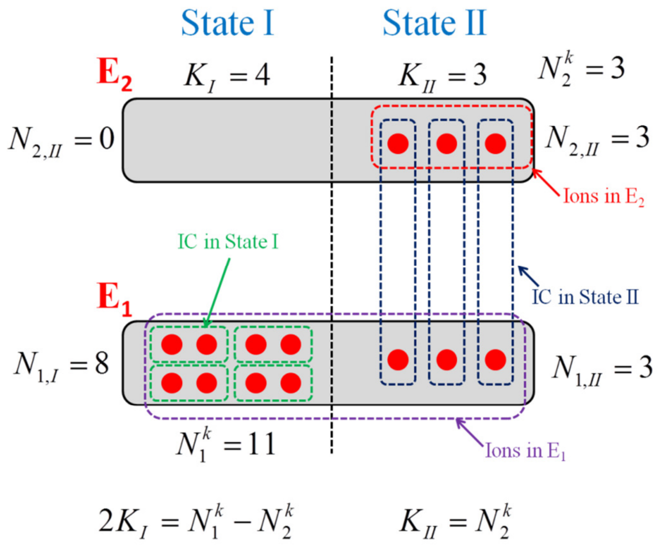

Figure 7-1 An illustration of the relationship between the IC concentration and the ion population density in a simple case where 4 ICs are in state I and 3 ICs are in state II. The notation $N_{E,S}$ represents the ion concentration at energy level E in the state S.

By substituting the relationship between the IC concentration and the ion population density into Eq. (7-6), the rate equation in term of the ion population density can be expressed as:

$$\begin{aligned}\frac{dN_2^k}{dt} &= -\frac{dN_1^k}{dt} = -A_s N_2^k + 2R_{12}^i (N_1^k - N_2^k)/2 - R_{21}^i N_2^k \\ &= -A_s N_2^k + R_{12}^i N_1^k - (R_{12}^i + R_{21}^i) N_2^k,\end{aligned} \tag{7-10}$$

with the steady-state solution:

$$N_2^k = \frac{R_{12}^s N_0^k}{A_i + 2R_{12}^i + R_{21}^i}, \tag{7-11}$$

where $N_0^k = N_1^k + N_2^k = 2(K_I + K_{II})$.

Overall, the population density of the excited ions in the steady-state by considering both the HUC and PIQ is [42]:

$$N_2 = N_2^i + N_2^k = \frac{R_{12}^i N_t (1-2k)}{A_i + R_{12}^i + R_{21}^i + (1+\frac{1}{m}) C N_2^i} + \frac{R_{12}^s 2kN_t}{A_i + 2R_{12}^i + R_{21}^i}. \tag{7-12}$$

Together with the standard equations for the evolution of optical power in the gain medium, the behaviour of the EDFA is simulated by assuming that only the fundamental mode is guided in a step index active fibre.

7.2 List of Publications

Journals related to this thesis

- E.-L. Lim, S. U. Alam, and D. J. Richardson, "High energy in-band pumped erbium doped fibre amplfiers," Opt. Express **20**, 18803–18818 (2012).
- E.-L. Lim, S. U. Alam, and D. J. Richardson, "Optimizing the pumping configuration for the power scaling of in-band pumped erbium doped fiber amplifiers," Opt. Express **20**, 13886-13895 (2012).
- E.-L. Lim, S. U. Alam, and D. J. Richardson, "The Multipeak Phenomena and Nonlinear Effects in Q-Switched Fiber Lasers," IEEE Photonics Technology Letters **23**, 1763-1765 (2011).

Conference contributions related to this thesis

- E. L. Lim, S. U. Alam, and D. J. Richardson, " High energy in-band pumped cladding pumped erbium doped pulsed fibre laser," in *Conference on Lasers and Electro-Optics & Quantum Electronics and Laser Science Conference,* (San Jose USA, 2012).
- E. L. Lim, S. U. Alam, and D. J. Richardson, " High energy in-band pumped erbium doped pulsed fibre laser," SPIE Photonics West (San Francisco USA, 2012).
- E. L. Lim, S. U. Alam, and D. J. Richardson, "Highly efficient, high power, inband-pumped Erbium/Ytterbium-codoped fiber laser," in *Conference on Lasers and Electro-Optics & Quantum Electronics and Laser Science Conference,* (Baltimore USA, 2011).

Other publication

- Q. Kang, E. L. Lim, Y. Jung, J. K. Sahu, F. Poletti, C. Baskiotis, S. U. Alam, D. J. Richardson, " Accurate modal gain control in a multimode erbium doped fiber amplifier incorporating ring doping and a simple LP01 pump configuration," Opt. Express **19**, 20835-20843 (2012).

Chapter 8 References

1. A. Hardy, "Signal amplification in strongly pumped fiber amplifiers," IEEE Journal of Quantum Electronics **33**, 307-313 (1997).
2. E. Stiles, "New developments in IPG fiber laser technology," in *5th International workshop on fiber laser*, 2009),
3. V. Kuhn, D. Kracht, J. Neumann, and P. Wessels, "67 W of Output Power From an Yb-Free Er-doped Fiber Amplifier Cladding Pumped at 976 nm," IEEE Photonics Technology Letters **23**, 432-434 (2011).
4. V. Kuhn, D. Kracht, J. Neumann, and P. Wessels, "Er-doped photonic crystal fiber amplifier with 70 W of output power," Optics Letters **36**, 3030-3032 (2011).
5. Y. Jeong, S. Yoo, C. A. Codemard, J. Nilsson, J. K. Sahu, D. N. Payne, R. Horley, P. W. Turner, L. Hickey, A. Harker, M. Lovelady, and A. Piper, "Erbium : Ytterbium codoped large-core fiber laser with 297-W continuous-wave output power," IEEE Journal of Selected Topics in Quantum Electronics **13**, 573-579 (2007).
6. D. J. Richardson, J. Nilsson, and W. A. Clarkson, "High power fiber lasers: current status and future perspectives," Journal of the Optical Society of America B-Optical Physics **27**, B63-B92 (2010).
7. V. Philippov, J. K. Sahu, C. Codemard, W. A. Clarkson, J. N. Jang, J. Nilsson, and G. N. Pearson, "All-fiber 1.15 mJ pulsed eye-safe optical source," in *Fiber Lasers: Technology, Systems, and Applications*, L. N. Durvasula, ed. (2004), pp. 1-7.
8. K. K. Chen, S. U. Alam, J. R. Hayes, H. J. Baker, D. Hall, R. McBride, J. Price, D. Lin, A. Malinowski, and D. J. Richardson, "56-W Frequency-Doubled Source at 530 nm Pumped by a Single-Mode, Single-Polarization, Picosecond, Yb3+ -Doped Fiber MOPA," Ieee Photonics Technology Letters **22**, 893-895 (2011).
9. F. Kienle, K. K. Chen, S.-u. Alam, C. B. E. Gawith, J. I. Mackenzie, D. C. Hanna, D. J. Richardson, and D. P. Shepherd, "High-power, variable repetition rate, picosecond optical parametric oscillator pumped by an amplified gain-switched diode," Opt. Express **18**, 7602-7610 (2010).
10. A. Ghatak and K. Thyagarajan, *Introduction to fiber optics* (Cambridge Univesity Press, 1997).
11. A. W. Snyder and J. D. Love, *Optical Waveguide Theory* (Chapman and Hall, 1983).
12. G. P. Agrawal, *Nonlinear fiber optics* 3ed. (Academic Press, 2001).
13. B. E. Saleh and M. C. Teich, *Fundamentals of Photonics* (John Wiley & Sons, Inc., 1991).
14. H. L. Offerhaus, N. G. Broderick, D. J. Richardson, R. Sammut, J. Caplen, and L. Dong, "High-energy single-transverse-mode Q-switched fiber laser based on a multimode large-mode-area erbium-doped fiber," Optics Letters **23**, 1683-1685 (1998).
15. K. Morishita, "Numerical-analysis of pulse broadening in graded index optical fibers," IEEE Transactions on Microwave Theory and Techniques **29**, 348-352 (1981).
16. R. W. Boyd, *Nonlinear Optics* (Academic Press, 2007).
17. R. Paschotta, (2012), retrieved http://www.rp-photonics.com.

18. A. Kobyakov, M. Sauer, and D. Chowdhury, "Stimulated Brillouin scattering in optical fibers," Adv. Opt. Photon. **2**, 1-59 (2010).
19. J. Nilsson, P. Blixt, B. Jaskorzynska, and J. Babonas, "Evaluation of parasitic up-conversion mechanisms in Er3+-doped silica-glass fibers by analysis of fluorescence at 980 nm," Journal of Lightwave Technology **13**, 341-349 (1995).
20. G. Vienne, "Fabrication and characterisation of ytterbium:erbium codoped phosphsilicat fibres for optical amplifiers and lasers," (University of Southampton, Southampton, 1996).
21. G. G. Vienne, J. E. Caplen, L. Dong, J. D. Minelly, J. Nilsson, and D. N. Payne, "Fabrication and characterization of Yb3+: Er3+ phosphosilicate fibers for lasers," Journal of Lightwave Technology **16**, 1990-2001 (1998).
22. P. C. Becker, N. A. Olsson, and J. R. Simpson, *Erbium-doped fiber amplifiers : fundamentals and technology* (Academic Press, San Diego, 1999).
23. C. A. Codemard, "High-power cladding-pumped Raman and erbium-ytterbium doped fibre sources," (University of Southampton, 2007).
24. H. Injeyan, G. D. Goodno, and G. Goodno, *High Power Laser Handbook* (McGraw-Hill, 2011).
25. M. N. Zervas, A. Marshall, and J. Kim, "Effective Absorption in Cladding-Pumped Fibers," in *Fiber Lasers Viii: Technology, Systems, and Applications*, J. W. H. E. C. Dawson, ed. (2011).
26. R. S. Quimby, *Photonics and Lasers,* 1 ed. (John Wiley & Sons, 2006).
27. G. Canat, J. C. Mollier, J. P. Bouzinac, G. M. Williams, B. Cole, L. Goldberg, and Y. Jaouen, "Dynamics of high-power erbium-ytterbium fiber amplifiers," Journal of the Optical Society of America B-Optical Physics **22**, 2308-2318 (2005).
28. C. R. Giles and E. Desurvire, "Modeling erbium-doped fiber amplifiers," Journal of Lightwave Technology **9**, 271-283 (1991).
29. E. Dersurvire, *Erbium-doped fiber amplifiers: principles and applications* (Wiley-Interscience, New York, 1994).
30. C. Carter, B. Samson, K. Tankala, D. P. Machewirth, V. Khitrov, U. H. Manyam, F. Gonthier, and F. Seguin, "Damage mechanisms in components for fiber lasers and amplifiers," in *Laser-Induced Damage in Optical Materials* (2005), pp. 561-571
31. A. E. Siegman, *Lasers* (University Science Book., 1986).
32. Y. Wang and C. Q. Xu, "Understanding multipeak phenomena in actively Q-switched fiber lasers," Optics Letters **29**, 1060-1062 (2004).
33. S. Adachi and Y. Koyamada, "Analysis and design of Q-switched erbium-doped fiber lasers and their application to OTDR," Journal of Lightwave Technology **20**, 1506-1511 (2002).
34. Y. Wang and C. Q. Xu, "Actively Q-switched fiber lasers: Switching dynamics and nonlinear processes," Progress in Quantum Electronics **31**, 131-216 (2007).
35. B. N. Upadhyaya, U. Chakravarty, A. Kuruvilla, K. Thyagarajan, M. R. Shenoy, and S. M. Oak, "Mechanisms of generation of multi-peak and mode-locked resembling pulses in Q-switched Yb-doped fiber lasers," Optics Express **15**, 11576-11588 (2007).
36. P. Roy and D. Pagnoux, "Analysis and optimization of a Q-switched erbium doped fiber laser working with a short rise time modulator," Optical Fiber Technology: Materials, Devices and Systems **2**(1996).
37. W. H. Press, S. A. Teukolsky, W. T. Vetterling, and B. P. Flannery, *Numerical Recipes in C* 2ed. (2002).

38. G. P. Agrawal, *Applications of Nonlinear fiber optics* (Academic Press, 2001).
39. S. Arahira, K. Watanabe, K. Shinozaki, and Y. Ogawa, "Successive excited-state absorption through a multistep proces in highly Er3+doped fiber pumped by a 1.48 um laser diode," Optics Letters **17**, 1679-1681 (1992).
40. J. Thogersen, N. Bjerre, and J. Mark, "Multiphoton absorption and cooperative up-conversion excitatin in Er3+ doped fibers," Optics Letters **18**, 197-199 (1993).
41. Y. O. Barmenkov, A. V. Kir'yanov, A. D. Guzman-Chavez, J. L. Cruz, and M. V. Andres, "Excited-state absorption in erbium-doped silica fiber with simultaneous excitation at 977 and 1531 nm," Journal of Applied Physics **106**(2009).
42. P. Myslinski, D. Nguyen, and J. Chrostowski, "Effects of concentration on the performance of erbium-doped fiber amplifiers," Journal of Lightwave Technology **15**, 112-120 (1997).
43. E. Delevaque, T. Georges, M. Monerie, P. Lamouler, and J. F. Bayon, "Modeling of pair-induced quenching in erbium-doped silicate fibers," IEEE Photonics Technology Letters **5**, 73-75 (1993).
44. S. Sergeyev, S. Popov, and A. T. Friberg, "Influence of the short-range coordination order of erbium ions on excitation migration and upconversion in multicomponent glasses," Opt. Lett. **30**, 1258-1260 (2005).
45. S. Sergeyev, S. Popov, D. Khoptyar, A. T. Friberg, and D. Flavin, "Statistical model of migration-assisted upconversion in a high-concentration erbium-doped fiber amplifier," J. Opt. Soc. Am. B **23**, 1540-1543 (2006).
46. D. Boivin, A. Pastouret, E. Burov, C. Gonnet, O. Cavani, S. Lempereur, and P. Sillard, "Performance Characterization of New Erbium-Doped Fibers using MCVD Nanoparticle Doping Process," in *Fiber Lasers Viii: Technology, Systems, and Applications*, J. W. Dawson and E. C. Honea, eds. (Spie-Int Soc Optical Engineering, Bellingham, 2011).
47. J. L. Philipsen, J. Broeng, A. Bjarklev, S. Helmfrid, D. Bremberg, B. Jaskorzynska, and B. Palsdottir, "Observation of strongly nonquadratic homogeneous upconversion in Er3+-doped silica fibers and reevaluation of the degree of clustering," IEEE Journal of Quantum Electronics **35**, 1741-1749 (1999).
48. P. Blixt, J. Nilsson, T. Carlnas, and B. Jaskorzynska, "Concentration-dependent upconversion in Er3+-doped fiber amplifiers: Experiments and modeling," IEEE Photonics Technology Letters **3**, 996-998 (1991).
49. P. Myslinski, J. Fraser, and J. Chrostowski, "Nanosecond Kinetics of Upconversion Process in EDF and its Effect on EDFA Performance," in *Optical Amplifiers and Their Applications*, 1995 OSA Technical Digest Series (Optical Society of America, 1995), ThE3.
50. A. Kirpsilayanov, Y. Barmenkov, and A. Guzman-Chavez, "Er 3+ excited-state absorption in an erbium-doped silica fiber at the wavelengths 1490-1580 and 978 nm," Laser Physics **18**, 1251-12561256 (2008).
51. J. Nilsson, B. Jaskorzynska, and P. Blixt, "Performance reduction and design modification of erbium-doped fiber amplifiers resulting from pair-induced quenching," IEEE Photonics Technology Letters **5**, 1427-1429 (1993).
52. D. Boivin, T. Fohn, E. Burov, A. Pastouret, C. Gonnet, O. Cavani, C. Collet, and S. Lempereur, "Quenching investigation on New Erbium Doped Fibers using MCVD Nanoparticle Doping Process," in *Fiber Lasers Vii: Technology,*

Systems, and Applications, K. Tankala and J. W. Dawson, eds. (Spie-Int Soc Optical Engineering, Bellingham, 2010).

53. K. Arai, H. Namikawa, K. Kumata, T. Honda, Y. Ishii, and T. Handa, "Aluminum or phosphorus co-doping effects on the fluorescence and structural properties of neodymium-doped silica glass," Journal of Applied Physics **59**, 3430-3436 (1986).
54. R. S. Quimby, W. J. Miniscalco, and B. Thompson, "Clustering in erbium-doped silica glass-fibers analyzed using 980 nm excited-state-absorption," Journal of Applied Physics **76**, 4472-4478 (1994).
55. J. Thomas, M. Myara, L. Troussellier, E. Burov, A. Pastouret, D. Boivin, G. Melin, O. Gilard, M. Sotom, and P. Signoret, "Radiation-resistant erbium-doped-nanoparticles optical fiber for space applications," Optics Express **20**, 2435-2444 (2012).
56. S. Tammela, M. Soderfund, J. Koponen, V. Philippov, and P. Stenius, "The potential of direct nanoparticle deposition for the next generation of optical fibers - art. no. 61160G," in *Optical Components and Materials III*, M. J. F. Digonnet and S. Jiang, eds. (Spie-Int Soc Optical Engineering, Bellingham, 2006), pp. G1160-G1160.
57. S. Tammela, M. Hotoleanu, P. Kiiveri, H. Valkonen, S. Sarkilahti, and K. Janka, "Very short Er-doped silica glass fiber for L-band amplifiers," Optical Fiber Communications Conference (OFC). **17**, 376-377 (2003).
58. M. Federighi and F. Dipasquale, "The effect of pair-induced energy-transfer on the performance of silica wave-guide amplifiers with high Er3+/Yb3+ concentrations," IEEE Photonics Technology Letters **7**, 303-305 (1995).
59. K. Aiso, Y. Tashiro, T. Suzuki, and T. Yagi, "Development of Er/Yb Co-doped Fiber for High-Power Optical Amplifiers," Furukawa Review **20**(2001).
60. J. Liu, P. F. Wysock, M. Andrejco, and B. Palsdottir, "Power conversion efficiency characterization of erbium-doped silica fibers in L-band," Optical Engineering **40**, 1195-1198 (2001).
61. M. A. Jebali, J. N. Maran, S. LaRochelle, S. Chatigny, M. A. Lapointe, and E. Gagnon, "A 103W High Efficiency In-Band Cladding-Pumped 1593nm All-Fiber Erbium-Doped Fiber Laser," in *2012 Conference on Lasers and Electro-Optics & Quantum Electronics and Laser Science Conference,* (San Jose USA, 2012).
62. M. Dubinskii, J. Zhang, and V. Ter-Mikirtychev, "Record-efficient, resonantly-pumped, Er-doped singlemode fibre amplifier," Electronics Letters **45**, 400-401 (2009).
63. V. R. Supradeepa, J. W. Nicholson, and K. Feder, "Continuous wave Erbium-doped fiber laser with output power of >100 W at 1550 nm in-band core-pumped by a 1480nm Raman fiber laser," in *2012 Conference on Lasers and Electro-Optics & Quantum Electronics and Laser Science Conference,* (San Jose USA, 2012).
64. J. Zhang, V. Fromzel, and M. Dubinskii, "Resonantly cladding-pumped Yb-free Er-doped LMA fiber laser with record high power and efficiency," Optics Express **19**, 5574-5578 (2011).
65. M. E. Likhachev, M. M. Bubnov, K. V. Zotov, D. S. Lipatov, M. V. Yashkov, and A. N. Guryanov, "Effect of the AlPO4 join on the pump-to-signal conversion efficiency in heavily Er-doped fibers," Optics Letters **34**, 3355-3357 (2009).

66. L. V. Kotov, M. E. Likhachev, M. M. Bubnov, O. I. Medvedkov, D. S. Lipatov, N. N. Vechkanov, and A. N. Guryanov, "Highly Efficient Double-Clad Yb-free Er-Doped All-Fiber Laser and Amplifier Pumped at 976 nm," in *2012 Conference on Lasers and Electro-Optics & Quantum Electronics and Laser Science Conference,* (San Jose USA, 2012).
67. S. U. Alam, A. T. Harker, R. J. Horley, F. Ghiringhelli, M. P. Varnham, P. W. Turner, M. N. Zervas, and S. R. Norman, "All-Fibre, High Power, Cladding-Pumped 1565nm MOPA Pumped By High Brightness 1535nm Pump Sources," 2008 Conference on Lasers and Electro-Optics & Quantum Electronics and Laser Science Conference, Vols 1-9, 1871-1872 (2008).
68. M. Dubinskii, J. Zhang, and I. Kudryashov, "Single-frequency, Yb-free, resonantly cladding-pumped large mode area Er fiber amplifier for power scaling," Applied Physics Letters **93**(2008).
69. M. Dubinskii, J. Zhang, and V. Ter-Mikirtychev, "Highly scalable, resonantly cladding-pumped, Er-doped fiber laser with record efficiency," Optics Letters **34**, 1507-1509 (2009).
70. E. L. Lim, S. U. Alam, and D. J. Richardson, "Highly efficient, high power, inband-pumped Erbium/Ytterbium-codoped fiber laser," in *2011 Conference on Lasers and Electro-Optics & Quantum Electronics and Laser Science Conference,* (Baltimore USA, 2011).
71. M. Laroche, S. Girard, J. K. Sahu, W. A. Clarkson, and J. Nilsson, "Accurate efficiency evaluation of energy-transfer processes in phosphosilicate Er3+-Yb3+-codoped fibers," Journal of the Optical Society of America B-Optical Physics **23**, 195-202 (2006).
72. E. Lallier and D. Papillon-Ruggeri, "High energy pulsed eye-safe fiber amplifier," 2011 Conference on Lasers & Electro-Optics Europe & 12th European Quantum Electronics Conference (CLEO EUROPE/EQEC) (2011).
73. S. Desmoulins and F. Di Teodoro, "High-gain Er-doped fiber amplifier generating eye-safe MW peak-power, mJ-energy pulses," Optics Express **16**, 2431-2437 (2008).
74. E. L. Lim, S. U. Alam, and D. J. Richardson, "The Multipeak Phenomena and Nonlinear Effects in Q-Switched Fiber Lasers," IEEE Photonics Technology Letters **23**, 1763-1765 (2011).
75. J. C. Jasapara, M. J. Andrejco, A. DeSantolo, A. D. Yablon, Z. Varallyay, J. W. Nicholson, J. M. Fini, D. J. DiGiovanni, C. Headley, E. Monberg, and F. V. DiMarcello, "Diffraction-Limited Fundamental Mode Operation of Core-Pumped Very-Large-Mode-Area Er Fiber Amplifiers," IEEE Journal of Selected Topics in Quantum Electronics **15**, 3-11 (2009).
76. N. A. Brilliant, R. J. Beach, A. D. Drobshoff, and S. A. Payne, "Narrow-line ytterbium fiber master-oscillator power amplifier," J. Opt. Soc. Am. B **19**, 981-991 (2002).
77. D. Taverner, D. J. Richardson, L. Dong, J. E. Caplen, K. Williams, and R. V. Penty, "158-mu J pulses from a single-transverse-mode, large-mode-area erbium-doped fiber amplifier," Optics Letters **22**, 378-380 (1997).
78. C. C. Renaud, H. L. Offerhaus, J. A. Alvarez-Chavez, J. Nilsson, W. A. Clarkson, P. W. Turner, D. J. Richardson, and A. B. Grudinin, "Characteristics of Q-switched cladding-pumped ytterbium-doped fiber lasers with different high-energy fiber designs," IEEE Journal of Quantum Electronics **37**, 199-206 (2001).

79. J. Nilsson and B. Jaskorzynska, "Modeling and optimization of low-repetition-rate high-energy pulse amplification in cw-pumped erbium-doped fiber amplifiers," Optics Letters **18**, 2099-2101 (1993).
80. Y. Wang and H. Po, "Dynamic characteristics of double-clad fiber amplifiers for high-power pulse amplification," Journal of Lightwave Technology **21**, 2262-2270 (2003).
81. J. Li, Z. Dai, Z. Ou, L. Zhang, Y. Liu, and Y. Liu, "Modeling and optimizing of low-repetition-rate high-energy pulse amplification in high-concentration erbium-doped fiber amplifiers," Optics Communications **282**, 3577-3582 (2009).
82. B. Desthieux, R. I. Laming, and D. N. Payne, "111 kw (0.5 mJ) pulse amplification at 1.55 micron using a gated cascade of 3 erbium doped fibre amplifiers," Applied Physics Letters **63**, 586-588 (1993).
83. N. G. R. Broderick, H. L. Offerhaus, D. J. Richardson, R. A. Sammut, J. Caplen, and L. Dong, "Large mode area fibers for high power applications," Optical Fiber Technology **5**, 185-196 (1999).
84. V. Philippov, J. K. Sahu, C. A. Codemard, J. Nilsson, and G. N. Pearson, "All-fiber 0.4 mJ high-coherence eye-safe optical source," in *Solid State Laser Technologies and Femtosecond Phenomena*, J. A. C. C. W. A. Terry, ed. (2004), pp. 284-288.
85. J. D. Minelly, V. Stasyuk, J. P. de Sandro, E. Gagnon , and S. Chatigny, "Yb-free High energy double-clad Er fiber amplifier," in *Optical Amplifiers and their Applications (OAA 2004),* (San Francisco, CA., 2004).
86. C. Codemard, C. Farrell, P. Dupriez, V. Philippov, J. K. Sahu, and J. Nilsson, "Millijoule, high-peak power, narrow-linewidth, sub-hundred nanosecond pulsed fibre Master-Oscillator Power-Amplifier at 1.55 mu m," Comptes Rendus Physique **7**, 170-176 (2006).
87. V. Khitrov, V. Shkunov, D. Rockwell, F. Strohkendl, and Y. Zakharenkov, "Er-doped high aspect ratio core (HARC) rectangular fiber producing 5-mJ, 13-nsec pulses at 1572 nm," in OSA Technical Digest (CD) (Optical Society of America, 2012), AW4A.5.
88. P. N. Butcher and D. Cotter, *The Elements of Nonlinear Optics,* 1 ed. (Cambridge University Press, Cambridge, 1990).
89. C. Corbari, "Development of Non-Linear Waveguide Devices for Optical Signal Processing," (University of Southampton, 2005).
90. A. Canagasabey, "Development of Frequency Converters with Extended Functionalities in Periodically Poled Silica Fibres," (University of Southampton, 2009).
91. G. Bonfrate, "Optical Parametric Processes in periodically poled silica fibres," (University of Southampton, 2000).
92. T. G. Alley, "The formation of the second-order nonlinearity in thermally poled fused silica glass," (DTIC Document, 1998).
93. Y. S. Liu, T. Galvin, T. Hawkins, J. Ballato, L. Dong, P. Foy, P. Dragic, and J. Eden, "Linkage of oxygen deficiency defects and rare earth concentrations in silica glass optical fiber probed by ultraviolet absorption and laser excitation spectroscopy," Optics Express **20**, 14494-14507 (2012).
94. R. Kashyap, *Fiber Bragg Gratings* (Academic Press, 1999).
95. C. Corbari, (personal communication, 2011).
96. V. Pruneri, G. Bonfrate, P. G. Kazansky, C. Simonneau, P. Vidakovic, and J. A. Levenson, "Efficient frequency doubling of 1.5 mu m femtosecond laser pulses

in quasi-phase-matched optical fibers," Applied Physics Letters **72**, 1007-1009 (1998).

97. V. Pruneri, G. Bonfrate, P. G. Kazansky, D. J. Richardson, N. G. Broderick, J. P. de Sandro, C. Simonneau, P. Vidakovic, and J. A. Levenson, "Greater than 20%-efficient frequency doubling of 1532-nm nanosecond pulses in quasi-phase-matched germanosilicate optical fibers," Optics Letters **24**, 208-210 (1999).
98. G. Bonfrate, V. Pruneri, and P. G. Kazansky, "Periodic UV erasure of the nonlinearity for quasi-phase-matching in optical fibers," Conference on Lasers and Electro-Optics (CLEO 2000). Technical Digest. Postconference Edition. TOPS Vol.39 (IEEE Cat. No.00CH37088), 73-7373 (2000).
99. C. Corbari, A. Canagasabey, M. Ibsen, F. Mezzapesa, C. Codemard, J. Nilsson, and P. G. Kazansky, "All-fibre frequency conversion in long periodically poled silica fibres," 2005 Optical Fiber Communications Conference Technical Digest (IEEE Cat. No. 05CH37672), 3 pp. Vol. 6-3 pp. Vol. 63 pp. Vol. 66 (2005).
100. A. Canagasabey, C. Corbari, A. V. Gladyshev, F. Liegeois, S. Guillemet, Y. Hernandez, M. V. Yashkov, A. Kosolapov, E. M. Dianov, M. Ibsen, and P. G. Kazansky, "High-average-power second-harmonic generation from periodically poled silica fibers," Optics Letters **34**, 2483-2485 (2009).
101. R. A. Myers, N. Mukherjee, and S. R. J. Brueck, "Large 2nd-order nonlinearity in poled fused-silica," Optics Letters **16**, 1732-1734 (1991).
102. P. G. Kazansky, V. Pruneri, and P. S. Russell, "Blue-light generation by quasi-phase matched frequency-doubling in thermally poled optical fibers," Optics Letters **20**, 843-845 (1995).
103. H. G. de Chatellus, S. Montant, and E. Freysz, "Spatial control of second-order optical susceptibility induced in thermally poled glasses," Applied Physics Letters **78**, 3018-30203020 (2001).
104. A. Kameyama, A. Yokotani, and K. Kurosawa, "Identification of defects associated with second-order optical nonlinearity in thermally poled high-purity silica glasses," Journal of Applied Physics **89**, 4707-4713 (2001).
105. T. Yilmaz, L. Vaissie, M. Akbulut, D. M. Gaudiosi, L. Collura, T. J. Booth, J. C. Jasapara, M. J. Andrejco, A. D. Yablon, C. Headley, and D. J. DiGiovanni, "Large-mode-area Er-doped fiber chirped-pulse amplification system for high-energy sub-picosecond pulses at 1.55 mu m," in *Fiber Lasers V: Technology, Systems, and Applications*, J. Broeng and C. Headley, eds. (Spie-Int Soc Optical Engineering, Bellingham, 2008), pp. U296-U303.
106. J. W. Dawson, M. J. Messerly, R. J. Beach, M. Y. Shverdin, E. A. Stappaerts, A. K. Sridharan, P. H. Pax, J. E. Heebner, C. W. Siders, and C. P. J. Barty, "Analysis of the scalability of diffraction-limited fiber lasers and amplifiers to high average power," Optics Express **16**, 13240-13266 (2008).
107. J. W. Dawson, M. J. Messerly, J. E. Heebner, P. H. Pax, A. K. Sridharan, A. L. Bullington, R. J. Beach, C. W. Siders, C. P. J. Barty, and M. Dubinskii, "Power scaling analysis of fiber lasers and amplifiers based on non-silica materials," in *Laser Technology for Defense and Security Vi*, M. P. S. G. Dubinskii, ed. (2010).
108. S. M. Kobtsev and S. V. Smirnov, "Modelling of high-power supercontinuum generation in highly nonlinear, dispersion shifted fibers at CW pump," Optics Express **13**, 6912-6918 (2005).
109. J. Nilsson, R. Paschotta, J. E. Caplen, and D. C. Hanna, "Yb3+-ring-doped fiber for high-energy pulse amplification," Optics Letters **22**, 1092-1094 (1997).

110. L. Dong, X. Peng, and J. Li, "Leakage channel optical fibers with large effective," Journal of the Optical Society of America B-Optical Physics **24**, 1689-1697 (2007).

111. Y. M. Jung, Y. C. Jeong, G. Brambilla, and D. J. Richardson, "Adiabatically tapered splice for selective excitation of the fundamental mode in a multimode fiber," Optics Letters **34**, 2369-2371 (2009).